Berichte aus dem Institut für Mehrphasenströmungen
Band 16

Development of an Aerated High-Pressure Reactor for Biotechnological Applications

Vom Promotionsausschuss der Technischen Universität Hamburg
zur Erlangung des akademischen Grades
Doktor-Ingenieur (Dr.-Ing.)
genehmigte Dissertation

von

Daniel Niehaus

aus

Gehrden

2026

Impressum

Reihe: Berichte aus dem Institut für Mehrphasenströmungen, Band 16
Titel des Werkes: Development of an Aerated High-Pressure Reactor for Biotechnological Applications
Autor: Daniel Niehaus
Cuvillier Verlag GmbH
Nonnenstieg 8
37075 Göttingen
Telefon: 0049-551-547240
Webseite: www.cuvillier.de **E-Mail:** info@cuvillier.de

Bibliografische Informationen der Deutschen Nationalbibliothek
Die Deutsche Nationalbibliothek verzeichnet diese Publikation in der Deutschen Nationalbibliografie; detaillierte bibliografische Daten sind im Internet über http://dnb.dnb.de abrufbar.

1. Auflage, Göttingen. 2026
Zugl.: (TU) Hamburg, Univ., Diss., 2026

1. Gutachter: Prof. Dr. Michael Schlüter
2. Gutachter: Prof. Dr. Andreas Liese
Vorsitzender des Prüfungsausschusses: Prof. Dr. Alexander Penn
Tag der mündl. Prüfung: 19.06.25

ISSN 2943-8497
eISSN 3053-8203
ISBN 978-3-68952-432-6
eISBN 978-3-68952-433-3
ORCID 0000-0001-7217-7583
ISNI 0000000529571824
DOI 10.61061/ISBN_9783689524326

Acknowledgements

This dissertation was prepared in the course of my work at the Institute for Multiphase Flow. At this point, I would like to express my sincere gratitude to all those who supported me professionally, organizationally, and personally throughout this period.

First and foremost, I would like to thank Prof. Dr.-Ing. Michael Schlüter from the Institute for Multiphase Flow for supervising this work. I am equally grateful to Prof. Dr. Andreas Liese for serving as second reviewer and for the consistently constructive, project-spanning scientific exchange, including our joint work within the VR Lab. I would also like to thank Prof. Dr. Alexander Penn for chairing the examination committee and for his support and openness, including with regard to personal matters during the course of my doctoral studies.

I thank the entire team of the Institute for Multiphase Flow—both scientific and technical staff—for their support in daily work, the collegial atmosphere, and the many stimulating technical discussions. As representatives of the close collaboration and scientific exchange, I would like to particularly acknowledge Marc Maly and Sebastian Hofmann, whose support, constructive discussions, and collegial interaction accompanied this work in a special way. Special thanks are also due to Bettina Hoppe from the institute's administrative office. Her open and friendly manner, as well as her constant willingness to help, contributed significantly to a pleasant working environment.

I am especially grateful to Gregor Liebsch from PreSens Precision Sensing GmbH, as the project initiator of the Prot P.S.I. project, for the continuously valuable scientific exchange, numerous intellectual impulses, and the close collaboration throughout the entire project duration. I also thank Jochen Schoop-Zipfel from Ingenieurbüro Schoop for the always uncomplicated and reliable cooperation and his constant support, particularly with regard to control engineering issues. Furthermore, I would like to thank the team at Eurotechnica for their support in implementing the experimental setup and for carrying out the experiments and acquiring measurement data under high-pressure conditions.

My thanks also go to the theses I supervised, which contributed substantially to the content of this dissertation: Nils Dürkop, Jabrayil Guliyev, Saad Posharkar, Selma Iraqi Houssaini, and Lisa Hahn. I am likewise grateful to my student assistants Sina Bertram, Kim Meyer, and Hani Ahmadi for their dedicated work and support in everyday research activities.

My special thanks go to my partner Christina for her patience, understanding, and continuous support, particularly during many late-night hours at the desk. I also thank my parents, my sister Ann-Kathrin, and my many friends for their constant encouragement and support. I would like to explicitly thank them as well for their understanding when work in the pilot plant or laboratory took longer than initially anticipated and occasionally led to delays.

Abstract

A key element in the development of sustainable chemical products is the biotechnologization of chemical synthesis processes. One approach to intensifying biotechnological processes to make them competitive with established synthesis methods involves utilizing the process parameter of pressure. This is particularly of interest for enzymatically catalyzed oxidation reactions, which often face limitations due to low oxygen solubility, resulting in mass transport limitations.

This work presents and characterizes an aerated high-pressure batch reactor designed for the investigation of enzymatic systems at laboratory scale up to a pressure of 15.0 MPa. The characterization is divided into three parts: Firstly, the use of optical sensors for online measurement of dissolved oxygen concentration under pressure is considered. Showing that the optical sensors used can reliably measure an oxygen concentration of up to 227 mg l^{-1} even under significant pressure fluctuations. The second section deals with the characterization of mass transfer in the used high-pressure bubble column. Through optical access to the bubble column, the bubble size distribution is measured, and essential factors for mass transport, such as gas hold-up and interfacial area for mass transfer, are determined, highlighting in particular the influence of pressure on bubble diameter. The volumetric mass transfer coefficient is also determined using optical sensors.

In the context of validation experiments, the results of the preceding sections are combined, and the functionality of the setup with immobilized glucose oxidase is demonstrated. It is shown that the reaction can be monitored using optical sensors and that process intensification can be achieved through increased oxygen availability. It also becomes evident that the mass transport performance of the used bubble column is not sufficient to circumvent mass transport limitation. Based on these results, a scaled-up reactor concept of 2 liters is finally presented, based on a compact and high-performance jet loop reactor.

Zusammenfassung

Ein Schlüsselelement in der Entwicklung nachhaltiger chemischer Produkte ist die Biotechnologisierung chemischer Syntheseprozesse. Ein Ansatz zur Intensivierung biotechnologischer Prozesse, um sie mit etablierten Synthesemethoden wettbewerbsfähig zu machen, besteht darin, den Prozessparameter Druck zu nutzen. Dies ist besonders für enzymatisch katalysierte Oxidationsreaktionen von Interesse, die häufig aufgrund geringer Sauerstofflöslichkeit Einschränkungen unterliegen, was zu Stofftransportlimitationen führt.

Diese Arbeit stellt einen begasten Hochdruck-Batchreaktor vor, der für die Untersuchung von enzymatischen Systemen im Labormaßstab bis zu einem Druck von 15,0 MPa konzipiert wurde und charakterisiert diesen. Die Charakterisierung umfasst drei Teilbereiche: Zunächst wird der Einsatz von optischen Sensoren zur Online-Messung der gelösten Sauerstoffkonzentration unter Druck betrachtet, wobei gezeigt wird, dass die eingesetzten optischen Sensoren auch bei starken Druckwechselbelastungen eine Sauerstoffkonzentration von bis zu maximal 227 mg l^{-1} zuverlässig erfassen können. Der zweite Abschnitt beschäftigt sich mit der Charakterisierung des Stoffübergangs in der verwendeten Hochdruckblasensäule. Durch optische Zugänglichkeit zur Blasensäule wird die Blasengrößenverteilung gemessen und für den Stofftransport wesentliche Faktoren wie der Gasgehalt und die Stoffaustauschfläche bestimmt, wobei insbesondere der Einfluss des Drucks auf den Blasendurchmesser hervorgehoben wird. Mit Hilfe der optischen Sensoren wird ebenfalls der volumenspezifische Stoffübergangskoeffizient bestimmt.

Im Rahmen von Validierungsexperimenten werden die Ergebnisse der vorangegangenen Abschnitte zusammengeführt und die Funktionalität des Setups mit immobilisierter Glucoseoxidase dargelegt. Es wird gezeigt, dass die Reaktion über die optischen Sensoren verfolgt und durch die höhere Sauerstoffverfügbarkeit eine Prozessintensivierung erreicht werden kann. Ebenso wird deutlich, dass die Stofftransportperformance der eingesetzten Blasensäule nicht ausreicht, um eine Stofftransportlimitierung zu umgehen. Auf Grundlage dieser Erkenntnisse wird abschließend ein auf 2 Liter hochskaliertes Reaktorkonzept vorgestellt, das auf einem kompakten und leistungsstarken Treibstrahlschlaufenreaktor beruht.

Table of Contents

Nomenclature

Roman Symbols

$\dot{n}$	$\mathrm{mol \cdot m^{-2} s^{-1}}$	molar mass transfer
$\dot{V}$	$\mathrm{m^3 \cdot s^{-1}}$	volume flow rate
A	$\mathrm{m^2}$	surface/ interfacial area
A	$\mathrm{m^2 \cdot m^{-3}}$	Arrhenius coefficient
a	$\mathrm{m^2 \cdot m^{-3}}$	specific interfacial area
C	$-$	constant
c	$\mathrm{mol \cdot m^{-3}}$	molar concentration
D	$\mathrm{m^2 \cdot s^{-1}}$	diffusion coefficient
d	m	diameter
E	$\mathrm{kg \cdot m^{-2} \cdot s^{-2}}$	energy
F	$\mathrm{kg \cdot m \cdot s^{-2}}$	force
f	$\mathrm{s^{-1}}$	frequency
g	$\mathrm{m \cdot s^{-2}}$	gravitational constant, 9.81
H	$\mathrm{m^3 \cdot Pa \cdot mol^{-1}}$	Henry constant
h	m	height
I	mV	luminescence intensity
i	$-$	number

k	$\mathrm{m} \cdot \mathrm{s}^{-1}$	mass transfer coefficient
L	m	length
M	g/mol	molar mass
n	$-$	number
p	$\mathrm{kg} \cdot \mathrm{m}^{-1} \cdot \mathrm{s}^{-2}$	pressure
t	s/min	time
u	$\mathrm{m} \cdot \mathrm{s}^{-1}$	velocity
V	m^3	volume
R	$\mathrm{kg} \cdot \mathrm{m}^2 \cdot \mathrm{s}^{-2} \cdot \mathrm{K}^{-1} \cdot \mathrm{mol}^{-1}$	universal gas constant, 8.314
T	K	temperature
X		conversion
Z		compressibility factor

Dimensionless numbers

$Eo = \frac{g\Delta\rho d_b^2}{\sigma}$	Eötvös number
$Fr = \frac{w_b^2}{g d_p}$	Froude number
$Mo = \frac{g\eta^4\Delta\rho}{\rho^2\sigma^3}$	Morton number
$Re = \frac{w_b d_b \rho}{\eta_l}$	Reynolds number
$We = \frac{\rho_l w_b^2 r_b}{\sigma}$	Weber number

Greek Symbols

β	$\mathrm{m} \cdot s^{-1}$	mass transfer coefficient
δ	m	boundary layer thickness
η	$\mathrm{kg} \cdot \mathrm{m}^{-1} \cdot \mathrm{s}^{-1}$	dynamic viscosity
η		efficiency

γ	$-$	activity coefficient
ν	$\mathrm{m}^2 \cdot \mathrm{s}^{-1}$	kinematic viscosity
ν	$\mu\mathrm{mol} \cdot \mathrm{min}^{-1}$	enzymatic activity
ϕ	$\mathrm{kg} \cdot \mathrm{m} \cdot \mathrm{s}^{-2}$	fugacity
ρ	$\mathrm{kg} \cdot \mathrm{m}^{-3}$	density
ρ	$\mathrm{kg} \cdot \mathrm{m}^{-3}$	mass concentration
σ	$\mathrm{N} \cdot \mathrm{m}$	surface tension
τ	s	luminescence lifetime
ε	$-$	hold-up
φ	$^\circ$	phase angle

Superscripts

0	superficial
a	exponent a
b	exponent b

Subscripts

$*$	saturation concentration
0	unquenched state
$1/2$	half life
32	Sauter mean diameter
∞	bulk phase concentration
a	activation
air	air
B	buoyancy
b	bubble

bc	bubble column
br	bioreactor
conv	converted
D	drag
E	enzyme
g	gaseous phase
GA	gluconic acid
GL	glucose
GO_x	glucose oxidase
i	component i
in	inactivation
l	liquid phase
M	Michaelis Menten/ affinity coefficient
max	maximum
n	nozzle
O_2	oxygen
q	quenching
s	substrate
stat	steady state
supp	supplied
SV	Stern Volmer coefficient
T	inertia

trans	transferred

Acronyms / Abbreviations

BRENDA	BRaunschweig ENzym DAtabase
DAD	Diode Array Detector
EC	Enzyme Commission
EOM	Electro-Optical Module
HPLC	High-Performance Liquid Chromatography
JLR	Jet Loop Reactor
LED	Light Emitting Diode
NADH	Nicotinamide Adenine Dinucleotide
OCR	Oxygen Consumption Rate
PBR	Packed Bed Reactor
POCS	Periodic Open Cell Structures
SMA	SubMiniature version A
UV-Vis	Ultraviolet-Visible Spectroscopy

Chapter 1

Introduction

Given the increasing scarcity of fossil raw materials and their impact on the global climate, renewable raw materials are becoming increasingly important in the chemical industry [Clo17, Mar21]. One approach to creating sustainable production chains involves the employment of catalytically active proteins, commonly known as enzymes. Unlike traditional chemical catalysis, biocatalysis typically occurs under mild reaction conditions (ambient temperature, atmospheric pressure, and neutral pH). Moreover, biocatalysts are far more sustainable than catalysts traditionally reliant on rare metals [She18, Bor12]. Consequently, enzymes are particularly appealing for the production of large quantities of basic chemical feedstocks. Notable examples include the production of high fructose corn syrup using glucose isomerase [Jen87] and the utilisation of lipases in biodiesel production [Han20].

The high enantio-, regio-, and stereoselectivity exhibited by enzymes also holds significant promise in the production of fine chemicals and intricate, high-value molecules. Due to these attributes, conventional synthesis pathways can be streamlined, reducing the effort required for product purification [Sch18b]. Noteworthy examples encompass the enzymatic production of certain drugs for diabetes (saxagliptin and sitagliptin), central nervous system disorders (pregabalin), and autoimmune diseases (atazanavir) [Pat18]. Ongoing research and developments indicate that the full potential of enzymatically catalysed reactions has yet to be fully realized. This future potential lies in protein engineering and in comprehending and purposefully modifying the intricate protein structures. This could, for instance, enhance enzyme stability under industrial conditions or achieve heightened activity across a broader spectrum of substrates [Den15, Arn18].

In addition to enzyme design, the consideration of optimal operating parameters also plays a crucial role in an industrial integration. In this context, high pressure has emerged as a

promising parameter for optimizing biocatalytic processes. While enzymes typically function under mild conditions, controlled high pressure application presents new opportunities to enhance their industrial utility. The impact of high pressure on proteins was initially observed by Bridgman in 1914, who noted the denaturation of egg albumen under its influence [Bri14]. Since the early 2000s, this knowledge has found increasing application in the food industry. High pressure is now frequently employed to denature unwanted enzymes. Unlike thermal denaturation through pasteurization, deactivation via high pressure is a milder process that does not adversely affect product properties [Che95, Lud03]. Further scientific inquiry revealed that protein structure may shift before irreversible denaturation, potentially enhancing stability [Mee06], increasing enzyme activity [Rei22], or altering selectivity [Ber10]. Nevertheless, due to the intricate nature of protein structure, precise predictions remain challenging at present [Eis09, Cze17].

Furthermore, aside from its direct impact on the enzyme, the application of pressure can also affect the properties of the substrate, including density, viscosity, and gas solubility. This would be of particular interest for oxidation reactions. 60 % of conventionally catalysed chemicals in 2001 are products or intermediates from oxidation reactions [Cen01]. While oxidases present advantages over traditional catalysts, biocatalytic reactions under atmospheric conditions face challenges related to mass transport. This is attributed to the limited solubility of oxygen in aqueous media [Cha18].

1.1 Scope

Although the application of pressure in enzymatic reactions offers potential advantages, its technical implementation remains limited. This is primarily due to the lack of suitable reactor types and technologies for monitoring reactions under high-pressure conditions. The primary objective of this research is the design and development of an aerated high-pressure reactor specifically tailored for biocatalytic oxidations. This involves both the conceptual design of the reactor and the identification of appropriate sensor technologies capable of monitoring oxygen saturation under high pressure to ensure precise reactor control. A key feature of this reactor is the deliberate separation of the aeration process from the enzymes to minimize any adverse effects of aeration on enzyme activity. As part of the reactor's characterization, the behaviour of both the aeration process and the oxidase will be thoroughly investigated across the full operational spectrum. The insights gained from these studies will ultimately contribute to the development of a scalable reactor concept.

Chapter 2

State-of-the-Art

The following chapter introduces the chemical, physical, and biological principles employed in designing and characterising the aerated high-pressure reactor outlined in this work. This chapter is structured into three primary sections for clarity:

- **Mass Transfer Dynamics:** This section introduces various concepts of multiphase reactors. It provides the fundamental principles of mass transfer between gaseous and liquid phases and examines the influence of pressure on mass transfer.
- **Biocatalysis:** This section covers the fundamentals of enzymatically catalysed reactions, including basic reactions kinetics, the concept of enzyme immobilization and the impact of pressure on enzymatic activity.
- **Dissolved Oxygen Measurement Techniques:** The concluding section of this chapter reviews established measurement techniques for dissolved oxygen. Specifically emphasising the method of optical oxygen measurement through fluorescence quenching, applied as the main measurement technique within the aerated reactor.

2.1 Fundamentals of Mass Transfer

A crucial aspect of the envisioned reactor concept is to ensure an adequate supply of molecular oxygen for the enzymatic reaction. To achieve efficient mass transport between the gaseous and liquid phases, several multiphase reactors are available options. These include aerated stirred tank reactors, bubble columns, airlift and jet loop reactors (Figure 2.1). This study primarily focuses on bubble columns due to their simple design and their suitability for high-pressure applications, which results from the absence of moving components [Dec85].

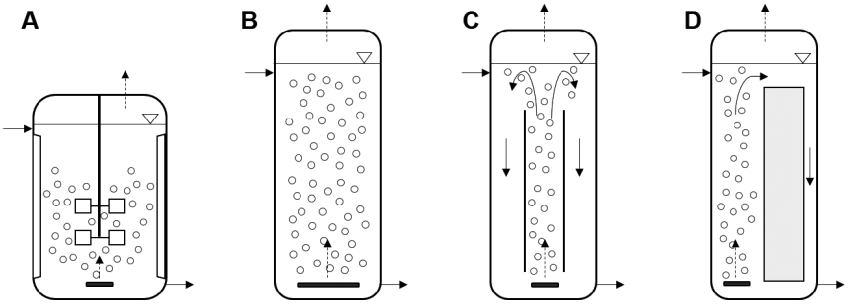

Fig. 2.1 Comparative overview of reactor types for aerated reactions, including (A) Stirred tank reactor, (B) Bubble column, (C) Jet loop reactor, and (D) Airlift reactor adapted from Stolle [Sto20].

The gas-liquid mass transfer within these reactors can be quantitatively described using theories like the penetration theory [Hig35], the surface renewal theory [Dan51] and two-film theory. The two-film theory is the simplest and oldest mass transfer theory, attributed to Lewis and Whitman [Lew24]. This theory assumes the formation of two adjacent boundary layers at the interface, characterized by a specific thickness δ and mass transfer coefficients β of each bubble.

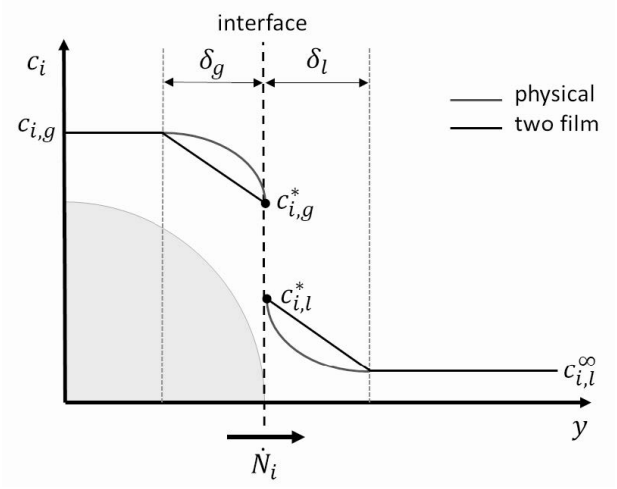

Fig. 2.2 Schematic representation of the two-film theory, illustrating mass transfer from a gas bubble into the surrounding liquid, adapted from Brauer [Bra71].

Thus, the equation for steady-state mass transport from the bulk phase to the phase interface can be expressed as

$$\dot{N}_i = \beta_l \cdot A \cdot (c_{i,l}^{\infty} - c_{i,l}^{*}) = \beta \cdot A \cdot \Delta c_{i,l} \tag{2.1}$$

as illustrated in Figure 2.2. The transported mass ($\dot{n}$) can be described with the help of the interfacial area A and the concentration gradient between the bulk phase c_l^{∞} and the interface c_l^{*}. The mass transport within the boundary is assumed as equimolar diffusion and can thus be described by Fick's first law, as shown in Equation 2.2

$$\dot{N}_i = -D \cdot A \cdot \frac{\Delta c_i}{\Delta \delta} \tag{2.2}$$

where D represents the diffusion coefficient, A the area, Δc_i the concentration difference, and $\Delta\delta$ the thickness of the boundary layer [Fic55]. Combining Equations 2.1 and 2.2 allows for the derivation of an expression for the mass transfer coefficient. This derivation underscores the direct relationship between the diffusion coefficient and the thickness of the boundary layer according to

$$\beta = \frac{D}{\Delta \delta}. \tag{2.3}$$

To model mass transfer across the full phase boundary, an analogous mass transfer equation is applicable for both the gas and liquid phases. At the phase boundary, a phase equilibrium is established, allowing the difficult-to-measure concentration at the boundary to be substituted with the equilibrium concentration. This equilibrium concentration can be calculated using the Henry coefficient H as the distribution coefficient

$$c_l^{*} = H \cdot c_g \tag{2.4}$$

with c_l^{*} representing the equilibrium concentration in the liquid phase and c_g denotes the concentration in the gas phase [San15]. Hence, the individual mass transfer resistances within the boundary layers can be concisely represented as

$$\frac{1}{k_l} = \frac{1}{\beta_l} + \frac{1}{H \cdot \beta_g} \tag{2.5}$$

where k_l represents the overall mass transfer resistance, which results from the combined effects of the mass transfer resistances β_l and β_g in the liquid and gaseous phases [Kra12]. Considering Equation 2.5, the local mass transfer for both gas and liquid phases can be deduced as follows

$$\dot{N}_i = k_l \cdot A \cdot (c_l^{\infty} - c_l^*). \tag{2.6}$$

To link local mass transfer and mass transfer in an entire multiphase reactor, the reactor volume V_R and the volume-specific surface area a need to be integrated into Equation 2.6. The specific surface area can be calculated for spherical bubbles with

$$a = \frac{6 \cdot \varepsilon_g}{d_{32}} \tag{2.7}$$

using the gas hold-up ε_g and the Sauter mean diameter d_{32}. By incorporating Equation 2.7 into Equation 2.6, the change of concentration of the gaseous component within the liquid phase of the reactor over time can be expressed as

$$\frac{\mathrm{d}c_l}{\mathrm{d}t} = k_l \cdot a \cdot (c_l^{\infty} - c_l^*). \tag{2.8}$$

The mass transfer coefficient can be directly calculated by modifying and integrating Equation 2.8, resulting in Equation 2.9 which accounts for the logarithmic difference in dissolved oxygen concentration.

$$\ln \frac{c^* - c(t)}{c^* - c_0} = -k_l a \cdot (t - t_0) \tag{2.9}$$

Equation 2.8 and 2.7 underscores the crucial factors for mass transfer in multiphase reactors: the contact time between gas and liquid phases, bubble diameter d_{32}, and gas hold-up ε_g. These factors are significantly influenced by the reactor's fluid dynamics.

2.1.1 Flow Regimes

A pivotal factor influencing fluid dynamics within bubble columns is the flow regime. The rise of gas bubbles within liquids is classified into three categories, distinguished by the apparatus diameter and the superficial gas velocity u_g^0 of the gaseous phase. The superficial gas velocity is defined according to

$$u_g^0 = \frac{\dot{V}_g}{A_{bc}} \tag{2.10}$$

representing the velocity resulting from the gas volume flow rate $\dot{V}_g$ passing through the empty cross-sectional area A_{bc} of the bubble column. Figure 2.3 below illustrates the relationship between the bubble regime, superficial gas velocity, and bubble diameter. Across the full range of bubble column diameters, it is apparent that a uniform bubble regime forms at low superficial gas velocities, ranging from 3 to 8 cm s^{-1}. This regime is characterized

by a uniform velocity profile across the entire cross-section of the column, minimizing cross-mixing and thus preventing bubble break-up or coalescence. As a result, a very narrow bubble size distribution is achieved [Dec85]. With an increase in superficial gas velocity, a heterogeneous bubble flow is observed. Increased turbulence leads to bubble break up or coalescence, resulting in a wider bubble size distribution. This variation in bubble sizes creates distinct flow zones across the column's cross-section. In the central area, an upward flow prevails with larger bubbles ascending, while in the peripheral areas, a counterflow develops, where smaller bubbles either ascend slowly or are pulled downwards [Bes18]. In bubble columns of laboratory scale with a diameter less than 15 cm, bubbles tend to stabilize on the apparatus walls, allowing slug flow as gas velocity through the column increases [Kan05]. Figure 2.3 illustrates that the transitions between these regions occur over a wide range, influenced by various factors including the gas distributor type, the chosen liquid system, and liquid loading.

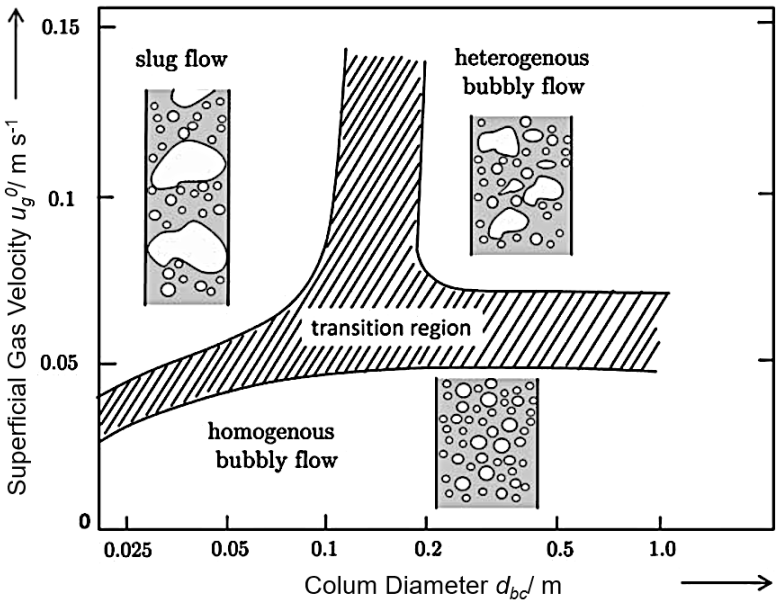

Fig. 2.3 Flow regime in bubble columns shown in relation to the column diameter d_{bc} and the superficial gas velocity u_g^0, adapted from Bothe [Bot16].

Gas Hold-Up

Another factor influencing the flow regime and mass transfer performance is the gas hold-up, denoted as ε_g. The gas hold-up, defined as

$$\varepsilon_g = \frac{V_g}{V_l + V_g} = \frac{V_g}{V_{tot}} \tag{2.11}$$

quantifies the volume of gas V_g dispersed throughout the total fluid volume V_{tot}. A proportional relationship between the superficial gas velocity and the gas hold-up can be expressed as

$$\varepsilon_g \sim u_g^n. \tag{2.12}$$

In principle, the gas hold-up increases with increasing superficial gas velocity. The factor n takes into account the influence of the flow regime. Thus n assumes a value of approximately one for the homogeneous flow regime. However, in the heterogeneous bubble regime, where larger bubbles are more prevalent, the value of n decreases. Consequently, the rate at which gas hold-up increases with superficial gas velocity becomes significantly reduced [Hik80, Kri91], as depicted in Figure 2.4.

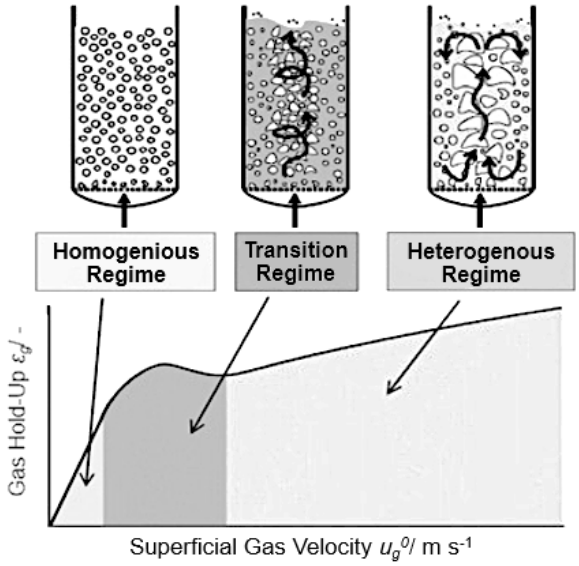

Fig. 2.4 Relationship between gas hold-up, superficial gas velocity, and flow regime adapted from Manjrekar [Man19]

2.1.2 Single Bubble Behaviour

In the previous sections, comprehensive understanding of bubble flows was developed through the examination of bubble regime and gas hold-up. Clearly, factors such as rise velocity, and consequently, residence time, mass transfer area, and boundary layer thickness at the interface, are significantly influenced by the behaviour of individual bubbles [Fan90]. An approach to analyse the rising velocity of a single bubble, u_b, is to examine the equilibrium of forces acting on the bubble. This equilibrium is considered when the bubble reaches its terminal rising velocity [Bra72]. At this point, the buoyancy force F_B and the drag force F_D acting on the bubble are in balance. The buoyancy force is given by

$$F_B = d_b^3 \cdot \frac{\pi}{6} \cdot g \cdot (\rho_l - \rho_g) \tag{2.13}$$

where d_b is the bubble diameter, g is the gravitational acceleration, ρ_l is the liquid density, and ρ_g is the gas density. Besides the buoyancy force, the drag force can be expressed as

$$F_D = c_D \cdot d_b^2 \cdot \frac{\pi}{4} \cdot \frac{\rho_l \cdot u_b^2}{2} \tag{2.14}$$

where c_D represents the drag coefficient, and u_b refers to the rising velocity of the gas bubble. By equating F_B (2.13) and F_D (2.14), the terminal rising velocity of the bubble can be calculated as

$$u_b = \sqrt{\frac{4}{3} \cdot \frac{d_b \cdot g \cdot \Delta\rho}{c_D \cdot \rho_l}}. \tag{2.15}$$

Equation 2.15 underscores the role of the drag coefficient c_d in determining the rising velocity. The drag coefficient encompasses effects on the dynamic boundary layer between gas and liquid, as well as influences from the bubble's shape [Cli92]. To accurately determine the drag coefficient, the surrounding flow conditions must be taken into account. These interactions are characterized by the dimensionless Reynolds number, which represents the balance between inertial and viscous forces.

$$\mathrm{Re} = \frac{u_b \cdot d_b}{\nu_l} = \frac{u_b \cdot d_b \cdot \rho_l}{\eta_l} \tag{2.16}$$

Figure 2.5 depicts the relationship between the Reynolds number and the drag coefficient, which applies to solid particles, droplets, and bubbles. This diagram categorizes the general behaviour into four distinct categories, following the criteria established by Peebles and Garber [Pee53].

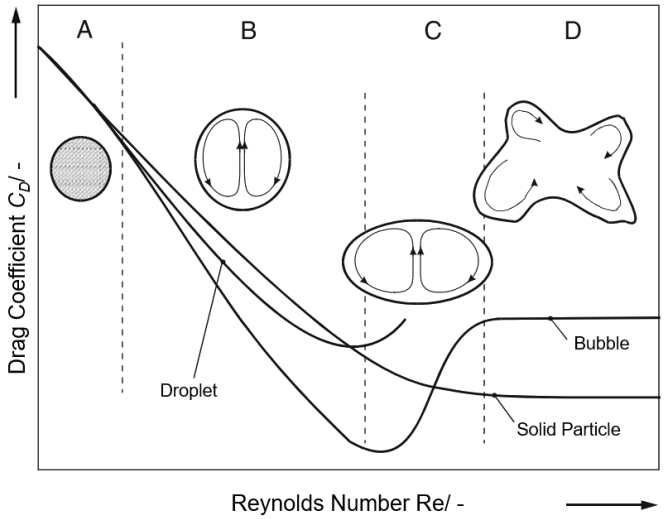

Fig. 2.5 Drag coefficient C_D as a function of Reynolds number Re for drops, bubbles, and solid particles based on Riquarts [Riq89].

In category A, bubble and droplets behave similar to rigid particles. However, in category B, this behaviour deviates from that of rigid particles, as the moving interphase induces internal circulation, which reduces the drag coefficient compared to solid particles. In category C, the forces of flow surpass the opposing internal forces, culminating in the creation of an ellipsoidal bubble shape that undergoes a tumbling movement during its ascent. This consequently results in a higher drag coefficient. Finally, category D illustrates the formation of an umbrella-shaped bubble (Davis Taylor Cap) characterized by a stable drag coefficient. For detailed insights and correlations to determine the drag coefficient, readers are referred to the work of Schlüter [Sch18a].

The dynamics of bubble motion and deformation have received considerable attention in the realm of fluid dynamic research. The so called Clift diagram, presented in Figure 2.6, offers an insightful summary of critical findings. This diagram successfully integrates key aspects of fluid mechanics and properties, such as density, viscosity, and surface tension, through the application of three dimensionless parameters, effectively demonstrating their influence on the shape and rising velocity of bubbles.

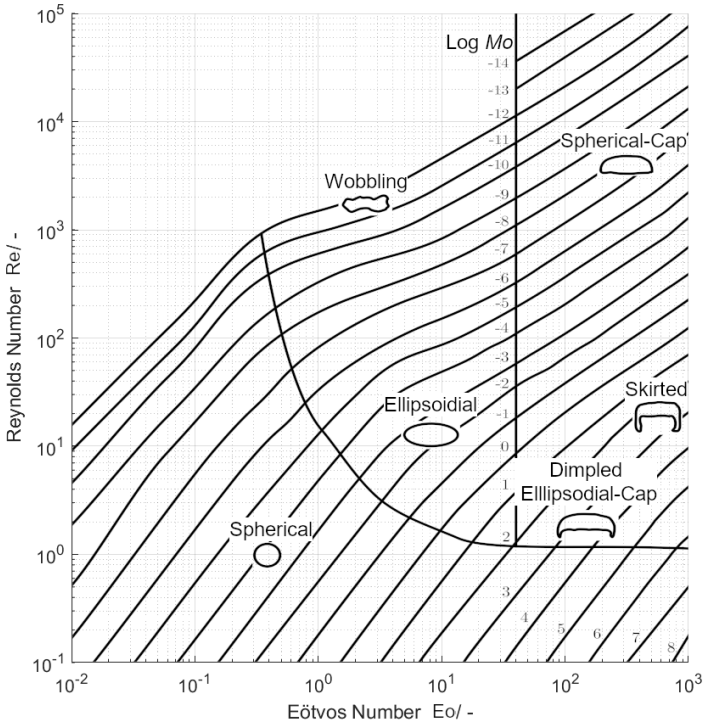

Fig. 2.6 Behaviour of bubbles and droplets in unhindered gravitational motion in the context of dimensionless properties, adapted from [Cli92].

In addition to the previously introduced Reynolds number in Equation 2.16, the diagram also incorporates the Morton number Mo, which delineates the interplay between viscous forces and surface tension, as given by

$$\mathrm{Mo} = \frac{g \cdot \eta^4 \cdot \Delta\rho}{\rho_l^2 \cdot \sigma^3} \tag{2.17}$$

where η is the dynamic viscosity, $\Delta\rho$ is the density difference between the gaseous and liquid phase and σ is the surface tension. The diagram further includes the Eötvös number Eo, which correlates volume forces to surface tension, expressed as

$$\mathrm{Eo} = \frac{g \cdot \Delta\rho \cdot d_b^2}{\sigma}. \tag{2.18}$$

Bubble Size

A factor influencing both the rising velocity and the mass transfer area is the bubble diameter [Kul05]. Depending on the flow regime, the bubble size distribution in turbulent and coalescing systems is primarily determined by the local energy dissipation. Conversely, in coalescence-inhibited and laminar systems, the bubble diameter generated at the aeration element dictates the bubble size distribution throughout the reactor's entire height. The Sauter mean diameter d_{32} [Sau26] is used as an important parameter for characterising the phase interface for transfer processes. As Equation 2.19 demonstrates, it represents the volume-to-surface area ratio.

$$d_{32} = \frac{\sum n_b \cdot d_b^3}{\sum n_b \cdot d_b^2} \tag{2.19}$$

To determine the bubble diameter formed at the aeration element, which predominates in the laminar flow regime, a quasi-stationary force equilibrium can be applied, as illustrated in Figure 2.7.

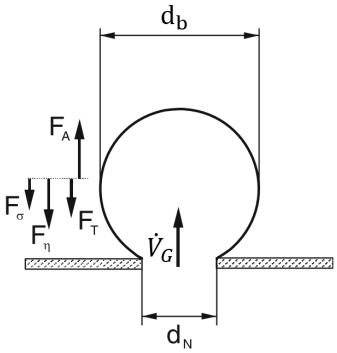

Fig. 2.7 Force equilibrium during periodic bubble formation [Sch18a].

This equilibrium, applicable to Newtonian bubbles and droplets, involves the buoyancy force F_B (Equation 2.13), the viscous force F_η, the inertia force F_T, and the surface tension force F_σ. The viscous force is defined as

$$F_\eta = 15 \cdot \eta_l \cdot \frac{\dot{V}_g}{d_b} \tag{2.20}$$

where η_l represents the dynamic viscosity of the liquid, $\dot{V}_g$ is the gas flow rate. The inertia force is given by

$$F_T = 1.3 \cdot \rho_l \cdot \left(\frac{\dot{V}_g}{d_b}\right)^2 \tag{2.21}$$

with ρ_l corresponds to the liquid density. As last part of the equilibrium at the bubble the surface tension force can be expressed as

$$F_\sigma = \pi \cdot d_n \cdot \sigma \tag{2.22}$$

including σ which represents the surface tension and d_b referring to the bubble diameter. The following relationship can be derived from the equilibrium for the generated bubble diameter

$$d_b = \left[\left(\frac{F_\eta + F_T + F_\sigma}{\Delta\rho \cdot g}\right) \cdot \frac{6}{\pi}\right]^{1/3}. \tag{2.23}$$

In addition to primary bubble formation at the aeration element, an increased gas volume flow resulting in a higher exit velocity leads to jet gassing and bubble fragmentation above the sparger, resulting in the creation of smaller secondary bubbles. To accurately determine the jet gassing region, either the dimensionless Weber We or Froude number Fr can be employed. The choice between the Weber and Froude numbers hinges on the sparger opening diameter d_n. For smaller hole diameters, the Weber number is applied, as it compares the inertia force to the stabilizing surface force, and buoyancy forces become negligible when surface tension is predominant [Bla88, Sch18a].

$$\begin{aligned} \mathrm{We_n} &= \frac{u_n^2 \cdot d_n \cdot \rho_g}{\sigma} \quad \textit{für} \\ d_n\sqrt{\frac{\rho_g \cdot g}{\sigma}} \cdot \left(\frac{\Delta\rho}{\rho_g}\right)^{5/8} &\leq 2.32 \end{aligned} \tag{2.24}$$

For larger hole diameters, buoyancy forces gain significance, prompting the use of the Froude number. The Froude number describes the ratio of inertial forces to gravitational forces, providing a more relevant parameter under these conditions:

$$\begin{aligned} \mathrm{Fr_{n,\Delta\rho}} &= \frac{u_n^2}{d_n \cdot g} \cdot \left(\frac{\rho_g}{\Delta\rho}\right)^{5/4} \quad \textit{for} \\ d_n\sqrt{\frac{\rho_g \cdot g}{\sigma}} \cdot \left(\frac{\Delta\rho}{\rho_g}\right)^{5/8} &> 2.32 \end{aligned} \tag{2.25}$$

The correlation between bubble gassing and jet gassing, as dictated by the Weber number, is depicted in the Figure 2.8 below:

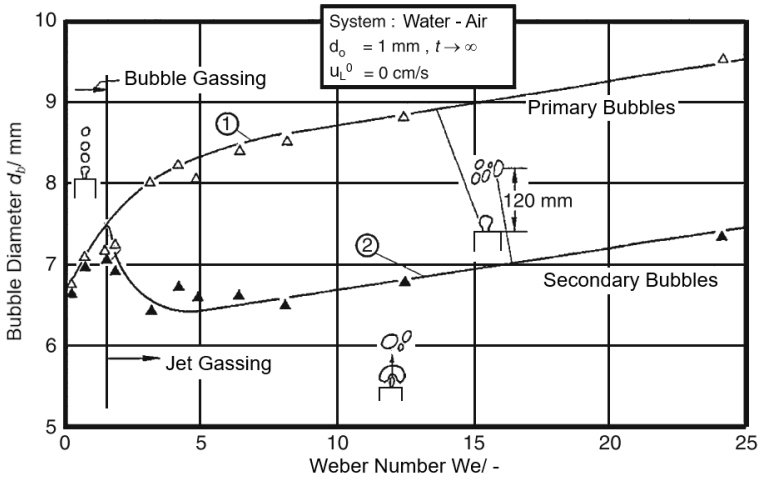

Fig. 2.8 Primary and secondary bubble formation at an open tube sparger in relation to the Weber number We based on Klug [Klu83].

2.1.3 Hydrodynamics and Mass Transfer in Pressurized Systems

The preceding sections have established an understanding of mass transfer and the various factors affecting them. It is widely recognised that chemical reactions often occur under conditions of elevated temperature and/or pressure to align with the optimal requirements for reaction kinetics and equilibrium states. This leading to a substantial body of literature regarding high pressure bubble columns [Jor02, Let99, Rol15, Wil94]. An insightful review of this topic is provided by Leonardo [Leo15]. Notably, a significant portion of investigations focuses on the pressure range between 0.1 and 3 MPa.

The impact of applying pressure is profound, altering both the physical and chemical properties of the phases involved in gas-liquid interactions. These modifications include changes in density, viscosity [Sch05], surface tension [Mas74], and gas solubility within the continuous phase, which showcases the intricate interplay between pressure and fluid properties. The most recognized method for describing solubility is Henry's Law (Equation 2.4). However, Henry's Law incorporates several simplifications, limiting its suitability in

high-pressure settings [San15]. These simplifications are as follows:

- Ideal mixture: Utilisation of the fugacity coefficient of pure substances instead of mixtures ($\phi_{0i} = \phi_i = \text{const.}$)
- Ideal gas behaviour: The fugacity coefficient is considered constant and therefore negligible ($\phi_{0i} = \phi_i = 1$)
- Ideal liquid phase: The liquid phase is assumed ideal, and hence the activity coefficients are considered constant and negligible ($\gamma_i^* = \gamma_i = 1$)
- Neglecting the Poynting correction at moderate pressures

These points reveal that deviations mainly arise from molecular interactions. Nevertheless, studies by Battino [Bat82], Geng [GEN10], and Zheng [Zhe19] indicate that for the pressure range up to 15.0 MPa considered in this study, an approximately ideal or linear behaviour can be assumed. This is attributed to the relatively low solubility of oxygen and nitrogen. For precise calculations of the maximum oxygen solubility in this work, the thermodynamic equation proposed by Tromans is employed, accounting for the effects of pressure and temperature [Tro00].

$$c_{O_2}^* = p_{O_2} \exp \frac{\underline{0.046T^2} \underline{+ 203.35T \cdot ln(T/298) - (299.378 + 0.092T)(T - 298) - 20.591 \cdot 10^3}}{R \cdot T} \tag{2.26}$$

Subsequently, the impact of these factors on the hydrodynamics and mass transfer within a high-pressure bubble column will be reviewed based on literature.

Flow Regime and Bubble Diameter

Various studies have investigated the impact of pressure on bubble regimes, particularly the transition between homogeneous and heterogeneous bubble flows. An increase in pressure leads to a delayed transition between these regimes, occurring at higher superficial gas velocities. This shift is linked to alterations in bubble coalescence and break up behaviours, with rising gas density fostering instabilities that promote increased bubble break-up and diminished coalescence [Kri91, Let97, Rei94, Rol16]. Consequently, the bubble size distribution narrows, reducing the average bubble diameter. Numerous studies also indicate the formation of a plateau at specific pressure levels, beyond which further pressure increase does not significantly decrease bubble diameter [Chi10, Wil92].

Rising Velocity and Gas Hold-Up

As highlighted by Equation 2.13, the contrast in density between the liquid and gaseous phases plays a pivotal role in determining the buoyancy forces of bubbles. The compressibility of the gaseous phase diminishes this differential, resulting in reduced buoyancy forces and rising velocity. Moreover, pressure affects not just the gas density ρ but also the surface tension σ and viscosity η, which in turn influence the bubble's shape and the drag coefficient C_D. Clift's methodology, which employs the Eötvös, Morton, and Reynolds numbers to characterize bubble shape and movement (see Section 2.1.2), accounts for variations in these physical properties. Lin's experimental data [Lin98] corroborates the accuracy of the Clift diagram, as depicted in Figure 2.9, in reflecting bubble behaviour in good precision even under varied pressure conditions.

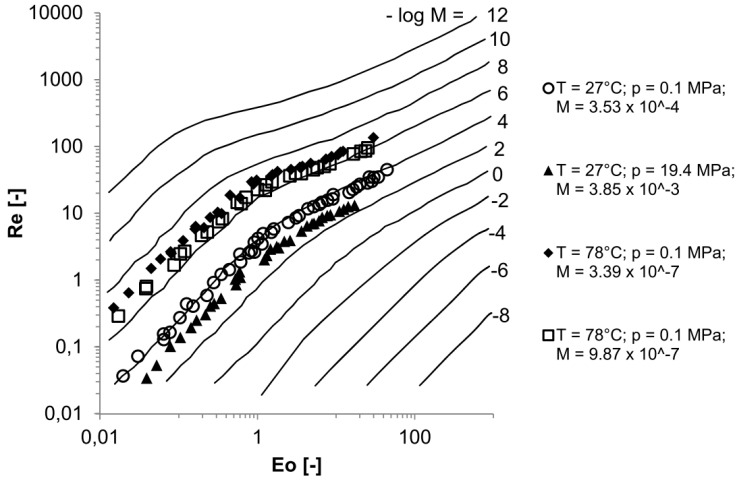

Fig. 2.9 Validation of the clift diagram for elevated pressures and temperatures, through comparison of measured and calculated Reynolds numbers (Re) for rising single bubbles in Paratherm NF adapted from Lin [Lin98].

The decrease in rising velocity and, consequently, the residence time results in an elevated gas hold-up ε_g. It is crucial to differentiate between the bubble regimes in this context. The increase in gas hold-up within the homogeneous bubble regime is modest, whereas it becomes markedly more pronounced in the heterogeneous bubble regime [Leo19].

Mass Transfer Coefficient

Numerous studies have demonstrated that pressure influences the volume-specific mass transfer coefficient $k_l a$. The key factor is the change in bubble diameter, which in turn affects residence time, gas hold-up, and mass transfer area. However, determining the k_l value is significantly more complex because it requires a comprehensive understanding of the mass transfer area under pressure conditions. The few studies that have addressed this issue indicate that the k_l value, is slightly reduced or remains constant [Chi10, Dew97].

2.2 Fundamentals of Enzymatic Reactions

In addition to fluid dynamics and mass transfer, biotechnology plays a crucial role in the reactor concept discussed in this study. To deepen the understanding of this concept and the associated research findings, the following sections will elucidate the fundamentals of enzyme kinetics, enzyme immobilization, and the contemporary understanding of enzymatic reactions under pressure.

2.2.1 Enzyme Kinetics

Enzymes, typically proteins, are large biological molecules capable of reducing the activation energy required for reactions by forming enzyme-substrate complexes. Their intricate structure adheres to the lock-and-key principle, ensuring that complexes form only with specific substrates, thus achieving markedly higher specificity than other catalysts. Enzymes are classified by their Enzyme Commission (EC) number, with the first digit indicating the type of reaction they catalyse. The Enzyme Commission has defined six main classes (oxidoreductases, transferases, hydrolases, lyases, isomerases, and ligases). Membership of a main class is also a good indicator of the stoichiometry of the catalysed reaction [Chm18]. This research primarily focuses on reactions catalysed by the first main class, the oxy-reductases, offering an in-depth analysis of their mechanisms.

One Substrate Kinetics

The foundational framework for enzyme kinetics was established by Leonor Michaelis and Maud Menten [Bri25]. The basic Michaelis-Menten equation can be derived using irreversible one-substrate (S) one-product (P) kinetics (uni-uni reaction, see reaction equation 2.27). In this context, an enzyme-substrate complex (ES) is formed during the reaction from substrate to product.

$$\mathrm{E} + \mathrm{S} \underset{k_{-1}}{\overset{k_1}{\rightleftharpoons}} \mathrm{ES} \xrightarrow{k_2} \mathrm{E} + \mathrm{P} \tag{2.27}$$

This model operates under the steady-state assumption, where the formation rate of the enzyme-substrate complex equals its dissociation rate plus the rate of product formation, leading to the derivation of the Michaelis-Menten equation:

$$v = \frac{v_{max} \cdot c_s}{c_s + K_M} \tag{2.28}$$

The reaction rate, denoted as v, is a function of the substrate concentration c_s,the Michaelis-Menten constant K_M, and the maximum reaction rate v_{max}. The Michaelis-Menten constant K_M indicates the enzyme's substrate affinity, defined as the substrate concentration at which the reaction rate is half of v_{max}. The maximum rate v_{max} is further defined by the total enzyme concentration c_E and the turnover number k_{cat}, which quantifies the number of substrate molecules an enzyme's active site can convert per second.

$$v_{max} = k_{cat} \cdot c_E \tag{2.29}$$

The reaction rate, including the binding of substrate and enzyme, is influenced by factors such as temperature and pH value. Like chemical reactions, the influence of temperature follows the Arrhenius equation, which quantifies its impact on activation energy and reaction kinetics. The equation incorporates the activation energy E_a, the universal gas constant R, the pre-exponential factor a, and the absolute temperature T.

$$k = a \cdot e^{-E_a/R \cdot T} \tag{2.30}$$

As temperature increases, a notable difference in enzyme behaviour is observed. Enzymes experience a sharp drop in reactivity upon reaching a certain maximum temperature, a phenomenon attributed to heat-induced denaturation, which leads to irreversible changes in the enzyme's structure. A similar situation is observed with pH values, where each enzyme has an optimum pH. Deviation from this optimum can also cause irreversible alterations to the enzyme's complex structure. The interplay between an enzyme's stability and its activity is crucial and must be taken into account in bioreactor design. Besides temperature and pH, enzyme stability is affected by various factors, including salts, solvents, detergents, radicals, radiation, and oxidants [Buc12]. The mathematical representation of enzyme inactivation utilizes the half-life time $t_{1/2}$ and the inactivation constant k_{in}.

$$t_{1/2} = \frac{ln(2)}{k_{in}} \tag{2.31}$$

A viable strategy to enhance enzyme stability is through the immobilization onto a carrier material. This technique is discussed in more detail in Section 2.2.2.

Multi-Substrate Kinetics

The uni-uni reaction kinetics, as mentioned in the previous section, are rare in practical applications. More commonly, reactions involve multiple substrates, necessitating the consideration of multi-substrate kinetics. Delving into multi-substrate kinetics introduces a level of complexity beyond the scope of this work. Therefore, the focus is placed on identifying the appropriate reaction mechanism for the oxidation reactions under study, which falls into the categories of Bi-Bi or Ter-Bi reaction kinetics.

In the context of multi-substrate kinetics, it is essential to differentiate between the sequence in which substrates bind to the enzyme and the rate-limiting step. The binding sequence can be organized as either a defined sequence (ordered), a random sequence (random), or a ping-pong mechanism, where one product is released before all substrates have attached to the enzyme's active site. Regarding the rate-limiting step, distinctions are drawn between rapid equilibrium and the steady-state mechanism. In the steady-state approach, the formation and breakup of covalent bonds become rate-limiting, with binding and dissociation steps proceeding rapidly and in equilibrium. The distribution of enzyme forms in this mechanism depends on the rate constants of all subprocesses [Bis17].

This study utilizes a steady-state ping-pong Bi-Bi reaction mechanism to analyse the enzymatic reaction of interest. The reaction mechanism is depicted in the form of a Cleland diagram, as shown in Figure 2.10.

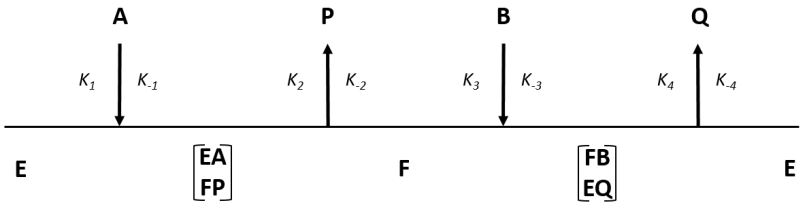

Fig. 2.10 Cleland Diagram illustrating the steady-state Ping-Pong Bi-Bi reaction kinetics, reprinted from [Chm18].

The enzymatic reaction involving two substrates (**A** and **B**) and two products (**P** and **Q**). The mechanism is characterized by the sequential interaction of the enzyme (**E**) with the

substrates and products, without forming a ternary complex. Initially, the enzyme (**E**) binds substrate (**A**) to form the enzyme-substrate complex [**EA**], which is then converted to the first product (**P**), leaving the enzyme in a modified state (**FP**). Subsequently, substrate (**B**) binds to the modified enzyme [**FP**], forming the complex [**FB**]. This leads to the conversion of (**B**) into the second product (**Q**), regenerating the enzyme in its original state (**E**).The reaction is governed by rate constants, which define the forward (K_1 to K_4) and reverse reactions (K_{-1} to K_{-4}) at each step of the mechanism.

Under steady-state conditions, the concentrations of intermediate complexes ([**EA**], [**FP**], and [**FB**]) remain constant, allowing for a simplified mathematical analysis of the reaction mechanism.

2.2.2 Enzyme Immobilisation

A pivotal component of the reactor design is the spatial segregation of the aeration unit from the enzymes. The technique of immobilization is key to achieving this separation by spatially fixing the enzyme, either on the walls of a Reactor or within a packed bed reactor (PBR) [Bol20]. Immobilization offers several advantages and disadvantages concerning reaction engineering. Advantages include improved enzyme stability, the possibility of enzyme reuse—which is significant considering the costs associated with enzyme purification—and easier separation of enzyme from product. Nonetheless, these benefits are offset by higher costs, increased preparation time, and potential disadvantages such as diffusion barriers due to the carrier's structure and decreased enzyme activity. Although attachment to a carrier material might limit enzyme activity, it can also affect the substrate's access to the enzyme's active site [Lie13].

Selecting a suitable carrier material is an integral part of the immobilization process. The ideal carrier should exhibit mechanical robustness and chemical inertness, combined with low cost. Macroporous polyacrylic particles are particularly noted for their utility in industrial settings. Beyond material selection, choosing an optimal immobilization technique is crucial [Bre13]. The last few decades have seen the development of numerous immobilization methods, with Figure 2.11 offering a comprehensive overview.

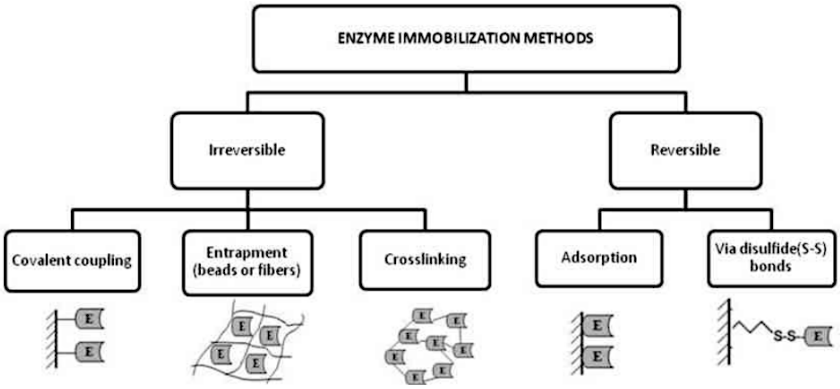

Fig. 2.11 Schematic overview of various enzyme immobilization methods as presented in Brena [Bre13].

Immobilization techniques are divided into reversible and irreversible methods. Reversible methods facilitate the straightforward removal of enzymes from the carrier in the event of complete denaturation, permitting the substitution of denatured enzymes with active ones. However, a potential drawback of these methods is the relatively weak binding of the enzyme to the carrier, which may result in enzyme leaching during operation. In contrast, irreversible immobilization methods, such as covalent bonding, entrapment, or cross-linking, are chosen to ensure that enzyme detachment is minimized under operational conditions. While covalent immobilisation effectively prevents enzyme loss, it leads to significant activity reduction and poses challenges for mass transfer [Dat13].

2.2.3 Enzymatic Reactions under Pressure

As outlined in the introduction, pressure can influence enzyme activity, selectivity, and stability. Predicting behaviour is challenging due to the complex structures of enzymes. Identifying factors and molecular structures that are affected either negatively or positively by pressure is still an ongoing area of research [Lei23].

Potential impacts on stability and activity can be partially deduced as follows: The catalytic activity of enzymes is attributed to their spatial conformation. Alterations to this conformation result in the loss of catalytic activity. The primary structure of enzymes is formed by the linkage of amino acids through peptide bonds. The secondary and tertiary structures are established through inter- and intramolecular noncovalent bindings, such as

hydrogen bonding, disulfide bridges, van der Waals forces, electrostatic, and hydrophobic interactions [Iye08, Lei17]. Pressure can also influence molecular and atomic bonds within an enzyme, thus affecting the enzyme's stability. For instance, hydrogen bonds are often strengthened under pressure, while ionic and hydrophobic interactions may be disrupted in aqueous solutions [Cze17]. The hydration shell of an enzyme can also be impacted by pressure, possibly becoming more ordered at higher pressures. This reordering could contribute to enhanced thermal stability of the enzyme under pressure [Eis09]. Another effect that could impact enzyme activity is the *Le Chatelier* principle. A driving effect can be achieved through pressure if the volume of the product is smaller than that of the substrate [Cha14].

2.3 Dissolved Oxygen Measurement Technologies

As underscored in earlier chapters, the concentration of dissolved oxygen in the solution is critical for analysing mass transfer and enzyme kinetics. Therefore, reliable and accurate measurement of this parameter becomes imperative. This section provides a comprehensive review of established measurement techniques, including iodometric determination, electrochemical determination, and optical oxygen determination. Given its application in the reactor setup under investigation, the operational principles of optical oxygen measurement technology are discussed in greater detail.

Iodometric Oxygen determination

The iodometric determination of dissolved oxygen, often known as the Winkler method, is renowned as a global standard for its accuracy [Win88, Int09]. This technique involves the addition of manganese sulfate and alkaline potassium iodide to the sample solution, resulting in the formation of unstable manganese hydroxide, as depicted by the reaction equation

$$4\,\mathrm{MnSO_4} + 8\,\mathrm{NaOH} \longrightarrow 4\,\mathrm{Mn(OH)_2}\downarrow + 4\,\mathrm{NA_2SO_4}. \tag{2.32}$$

Manganese hydroxide then reacts with dissolved oxygen to form manganic acid, as shown in the following equation 2.33

$$2\,\mathrm{Mn(OH)_2} + \mathrm{O_2} \longrightarrow 2\,\mathrm{H_2MnO_3}. \tag{2.33}$$

which subsequently transforms into manganese(III) oxide and water, as detailed in Equation 2.34

$$2\,H_2MnO_3 + 2\,Mn(OH)_3 \longrightarrow 2\,MnMnO_3\downarrow + 4\,H_2O. \tag{2.34}$$

The addition of sulfuric acid initiates two reactions. First, sulfuric acid reacts with potassium iodide to produce hydrogen iodide and potassium sulfate, as shown in Equation 2.35

$$4\,KI + 2\,H_2SO_4 \longrightarrow 4\,HI + 2\,K_2SO_4. \tag{2.35}$$

Subsequently, the manganese(III) oxide reacts with sulfuric acid and hydrogen iodide, resulting in the formation of manganese sulfate, iodine, and water, as captured in Equation 2.36

$$2\,MnMnO_3\downarrow + 4\,H_2SO_4 + HI \longrightarrow 4\,MnSO_4 + 2\,I_2 + 6\,H_2O. \tag{2.36}$$

The oxygen content is then quantified through titration with sodium thiosulfate, as shown in the following reaction equation

$$I_2 + 2\,Na_2S_2O_3 \longrightarrow 4\,NaI + Na_2S_4O_6. \tag{2.37}$$

Despite its reliability, the iodometric method is particularly labour-intensive and time-consuming [Wei19]. Consequently, its application for continuous in-situ measurements, especially in high-pressure environments, is considered impractical and is not the focus of this research.

Electrochemical Oxygen Determination

An alternative method for measuring dissolved oxygen concentrations is electrochemical determination, with polarography being a widely used approach. This technique involves measuring the current potential (or potential-time) of a polarized electrode during electrolysis and correlating it with the dissolved oxygen concentration. The Clark electrode, depicted in Figure 2.12, serves as a prime example:

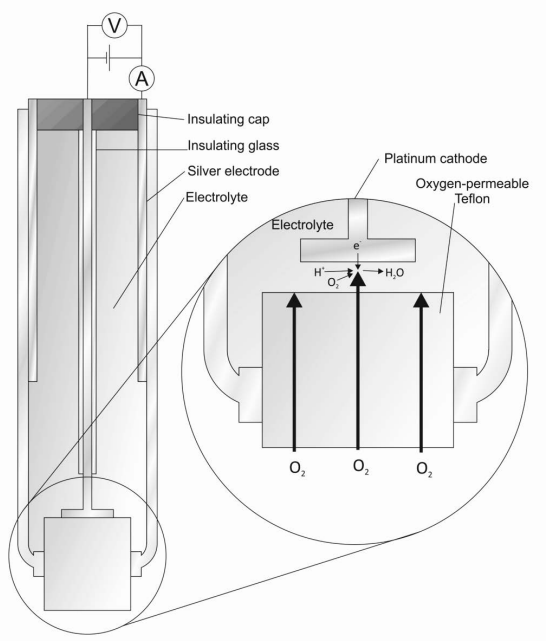

Fig. 2.12 Schematic structure of a Clark electrode for polarographic determination of dissolved oxygen concentrations ρ_{O_2} [O'C17].

The Clark Electrode consists of a working electrode, an auxiliary electrode, an air-permeable membrane, and an electrolyte solution. This setup prevents the electrodes and the measuring solution from direct contamination. Upon applying a voltage between the electrodes, oxygen molecules are reduced at the working electrode, as shown in

$$O_2 + 2H_2O \longrightarrow 4e^- + 4OH^-. \tag{2.38}$$

Simultaneously, at the auxiliary electrode, silver reacts with chloride ions, as described in the following equation

$$4Ag + 2Cl \longrightarrow 4AgCl + 4e^-. \tag{2.39}$$

This mechanism ensures a steady diffusion of oxygen molecules through the membrane, maintaining a consistent diffusion flux. While this method is a promising approach for continuous oxygen concentration measurements, it faces several limitations. The accuracy depends on the oxygen's diffusion through the membrane to the electrodes. Factors such as membrane contamination, low liquid flow velocities, or significant varying flow condition

changes at the measurement site can affect accuracy and measuring speed [Fra98]. Additionally, oxygen depletion (as indicated in Equation 2.39) poses a challenge in small volumes or low oxygen concentrations. Furthermore, additional factors such as electrical interference and potential electrode poisoning by H_2S, proteins, or other organic components must be considered [Wol15].

Optical Oxygen Determination

Since the early 1980s, fluorescence quenching has emerged as a notable method for measuring oxygen concentration. This technique involves embedding a luminophore within an oxygen-permeable polymer. Suitable luminophores span from polycyclic aromatic carbon compounds (e.g., pyrene or its derivatives) to complex transition metals (e.g., Ru^{2+}, Os^{2+}, Ir^{3}), or fullerenes [Qua12]. The measurement process begins with the excitation of the luminophore by an external light source, which triggers fluorescence. Oxygen present in the solution then quenches/reduces this fluorescence. This principle offers a robust solution to circumvent the drawbacks associated with previously mentioned methods. Fluorescence quenching is reversible and does not deplete the oxygen content of the sample. By anchoring the fluorophore in an oxygen-diffusive polymer, the measurement becomes independent of the sample's quality and unaffected by potential interfering agents [Dem99, Wol15]. Compared to iodometric and electrochemical techniques, fluorescence quenching provides faster measurements, making it suitable for continuous oxygen monitoring.

Therefore, fluorescence quenching has been chosen as the preferred method for measuring oxygen under pressure. The following sections provide an in-depth examination of this measurement technique and highlight the current understanding of its efficacy when applied in pressurized conditions.

2.3.1 Optical Measurement with Fluorescence Quenching

The principle of fluorescence quenching is based on quantum-physical processes resulting during the interaction between light and matter. As depicted in Figure 2.13, when a luminophore is excited by light at a specific wavelength, electrons transition from their ground state to higher energy levels. These electrons then seek to return to their original state, dissipating the excess energy through the emission of heat and light. Notably, the light emitted during this process has a longer wavelength than the excitation light, a phenomenon known as the Stokes shift, which is a characteristic of photoluminescence [Alb07].

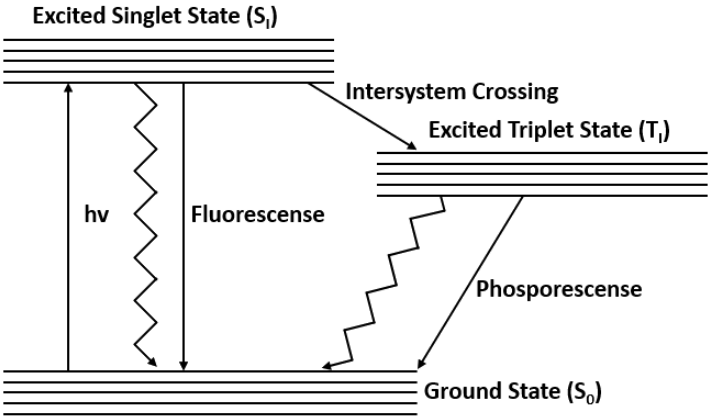

Fig. 2.13 Illustration of fluorescence and phosphorescence processes in the Jablonski diagram based on Amao [Ama03].

Photoluminescence encompasses both fluorescence and phosphorescence, which differ based on the excited state's characteristics. Fluorescence occurs when an electron transitions back from an excited singlet state to the singlet ground state. This process is spin-allowed, making it highly probable and resulting in a rapid decay time of about $10^{-9} - 10^{-7}$ seconds. Conversely, phosphorescence involves a change in the electron's spin, permitting a transition from the lowest excited triplet state back to the singlet ground state, although with a much lower probability. This process yields a longer light emission duration, ranging from $10^{-5} - 10$ seconds. The extended emission duration of phosphorescence makes it more sensitive to quenching by external molecular interactions [Lew44, Lot74].

Beyond emitting light, luminescence may also undergo dynamic quenching by a quencher, such as oxygen, through a process involving the collision between the quencher and the luminophore. In this interaction, the quencher absorbs the excited luminophore's energy, leading the luminophore to revert to its ground state without emitting light. This effect can be quantitatively related to the oxygen concentration using the Stern-Volmer relationship, shown in Equation 2.40 [Ste19]. This equation correlates the luminescence intensity ratio of the unquenched state I_0 to the quenched state I with the quencher concentration $[c_Q]$ and the Stern-Volmer constant K_{SV}, as shown in Equation

$$\frac{I_0}{I} = 1 + k_q \cdot \tau_0 \cdot [c_Q] = 1 + K_{SV} \cdot [c_Q]. \tag{2.40}$$

The Stern-Volmer constant K_{SV} is determined by the product of the luminescence lifetime in the unquenched state τ_0 and the bimolecular quenching constant k_q. As Equation 2.41 highlights, this constant incorporates both the collision frequency f_0 and the collision efficiency k_0 between the quencher and the luminophore

$$k_q = f_0 \cdot k_0. \tag{2.41}$$

The bimolecular rate coefficient, denoted as k_0, governs the rate-determining diffusion in the process. This coefficient can be determined using the Smoluchowski equation, underscoring the intricate nature of the diffusion process and its implications for measurement techniques. In an ideal scenario, luminophores in a homogeneous solution with the quencher adhere to the linear Stern-Volmer Equation 2.40. However, in fluorescence quenching measurements, the luminophore is embedded within a polymer matrix to isolate it from direct interactions with potentially luminescence-affecting agents, such as proteins, surfactants, solvents, and metal ions. This embedding can introduce heterogeneities, resulting in non-linear, downward-curved Stern-Volmer plots, particularly noticeable at elevated oxygen levels. Consequently, the selection of the polymer and its effect on the luminophore's quenching behaviour have been the focus of extensive research [Dem95].

Figure 2.14 illustrates the Stern-Volmer plot, which shows the relationship between oxygen saturation and luminescence quenching based on Equation 2.40. The x-axis represents oxygen saturation in percent, while the left y-axis shows the normalized luminescence intensity (I/I_0) or lifetime (τ/τ_0), and the right y-axis displays the phase angle (q) used in phase-modulated luminescence measurements.

The dashed line in the figure represents the idealized Stern-Volmer relationship, which predicts a linear correlation between oxygen concentration and luminescence quenching. The solid line shows the actual quenching behaviour of the fluorophore, with Region A marking the range of low oxygen saturation where quenching dynamics are dominated by efficient quencher-luminophore interactions. Region B, in contrast, corresponds to higher oxygen saturation levels, where the quenching efficiency decreases, leading to deviations from the ideal Stern-Volmer relationship. Additionally, the phase angle (q) decreases with increasing oxygen concentration, reflecting the dynamic quenching process.

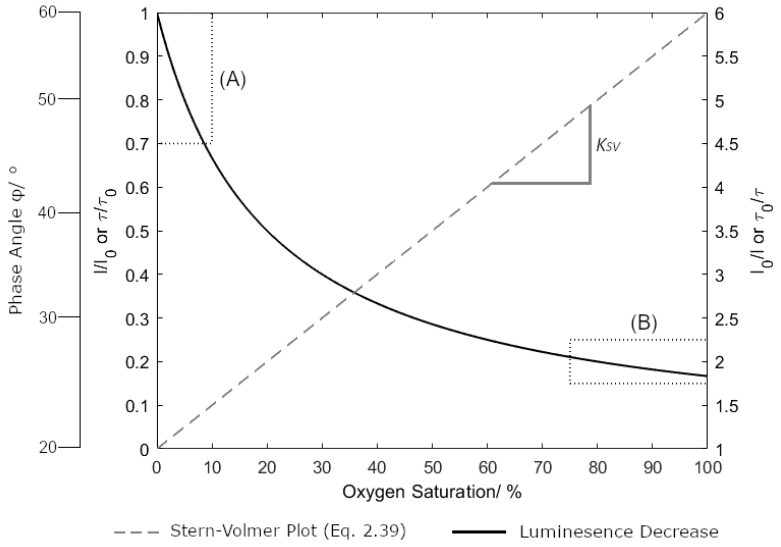

Fig. 2.14 Quenching behaviour of a fluorophore as a function of oxygen saturation under atmospheric conditions and its linearization by the Stern-Volmer equation.

2.3.2 Time and Frequency Domain Fluorescence Spectroscopy

As the Stern-Volmer equation demonstrates, both the intensity and lifetime of luminescence are parameters usable for determining the dissolved oxygen concentration. In intensity-based measurements, a light pulse activates the luminophore, and the resulting decrease in luminescence intensity is quantified. Although this approach provides repeatable responses and a favourable signal-to-noise ratio, it is significantly affected by external variables. These include sensitivity to variations in LED light emission, changes due to sensor spot positioning, and the gradual degradation of both light source and dye. To mitigate these issues, time-domain-dependent methods that utilize fluorescence lifetime, an intrinsic property of the luminophore, are employed. In this approach, the luminophore is excited by an LED emitting a sinusoidally modulated light, with the luminescence intensity responding in a phase-delayed sinusoidal manner, as depicted in Figure 2.15 [Lak06].

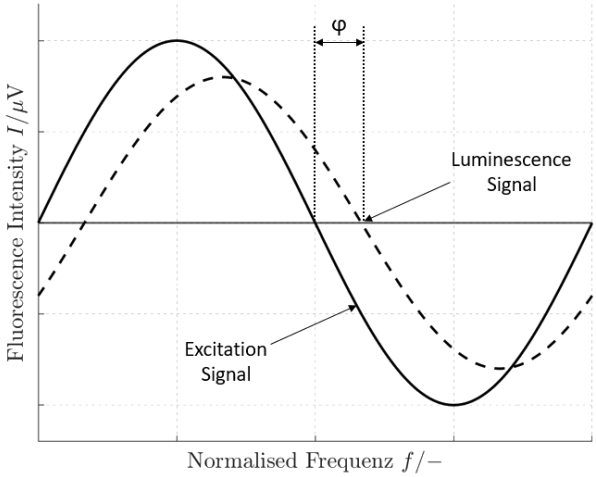

Fig. 2.15 Principle of the phase Fluorometry to measure dissolved oxygen concentrations.vgl Bambot

However, this is balanced by considering the lifetime or phase angle. The relationship between the lifetime τ and the phase angle φ can be expressed as follows for a single exponential decay.

$$\tau = \frac{tan(\varphi)}{2\pi \cdot f} \tag{2.42}$$

Selecting the modulation frequency f of the excitation signal involves a trade-off between the signal-to-noise ratio and phase sensitivity. While the signal-to-noise ratio may decline with an increase in frequency, phase sensitivity tends to improve [Bam94].

2.3.3 Effect of Pressure on Fluorescence Quenching

The deployment of optical oxygen sensors in high-pressure environments holds considerable importance, particularly within the fields of limnology and oceanography. Research in these domains examines the performance and precision of optical oxygen sensors in deep-sea conditions. Through this research, three primary factors have been pinpointed as determinants of sensor performance under pressure: the excited state stability of the luminophore, variations in quenching efficiency, and the solubility equilibrium between the polymer membrane and the surrounding medium [Bit18, Ten06].

High pressure can destabilize the luminophore's excited state, leading to oxygen-independent quenching. This phenomenon shortens the luminescence lifetime and induces a positive shift in O_2 detection. Despite the assumption that luminescence quenching is predominantly diffusion-driven, as shown in Equation 2.41, the effect of increased pressure on quenching efficiency is found to be minimal. The diffusion of oxygen within the polymer, governed by the chemical potential gradient and impeded by frictional resistance, remains relatively unaffected by pressure. This is because, although pressure elevates the chemical potential across the polymer, the essential gradient driving quenching efficiency does not change significantly [Bit18].

A pivotal factor under pressure is the solubility balance between the measurement medium and the polymer membrane, primarily due to differential pressure impacts on their solubilities [Dal22]. Dalfen's findings underscore that the sensor's response to pressure changes depend on this balance. Notably, with rising pressure, a consistent discrepancy in oxygen concentration measurement between the polymer and the medium is observed, which can be linearly related to the prevailing pressure. The slope of this linear relationship is directly linked to the material selected for the sensor's support structure.

Importantly, most studies on the use of oxygen sensors under high-pressure conditions focus on oxygen concentrations below atmospheric saturation (8.8 mg l^{-1}). This research, seeks to extend the exploration of sensor capabilities beyond this limit, aiming to thoroughly understand sensor behaviour in scenarios far exceeding the typical operational range.

Chapter 3

Experimental Setups

This thesis focuses on the design and investigation of an aerated high-pressure reactor for enzymatic catalysed oxidation reactions. This section comprehensively presents the individual components, measurements, and control technologies used within this reactor. Special attention is given to the oxygen measurement technology used, and the setup for examining optical probes is detailed. Utilizing this setup and the oxygen measurement technology, the study aims to investigate the effects of pressure on an enzymatic oxidation reaction. This model reaction is elaborated within the framework of an enzyme assay, from which the operational parameters for the reactor setup are systematically derived.

3.1 Reactor Setup

A key identification point of the reactor is the separation of aeration from the enzymes, addressing the direct aeration as a potential cause of enzyme deactivation. As research has shown, direct aeration might lead to enzyme deactivation, primarily due to shear forces and interactions between enzymes and gas bubbles [Tho11]. By maintaining this separation, the design not only addresses these concerns but also facilitates the independent optimization of operational conditions within the aeration unit and the bioreactor itself. The piping and instrumentation diagram of this reactor concept is depicted in Figure 3.1.

The aeration unit and the bioreactor are linked to create a continuous circulation loop. Additional peripheral equipment is integrated into this circulation loop. Liquid flow between these units is monitored with a mass flow meter (CORI-FLOW, M14, Bronkhorst, Ruurlo, Netherlands) and regulated using a gear pump (GA 180, Micropumps, Vancouver, USA), achieving a volumetric flow rate of $\dot{V}_l = 0.15$ to 1.5 ml s^{-1}. To ensure a uniform temperature throughout operation, the system is thoroughly insulated and features a spiral

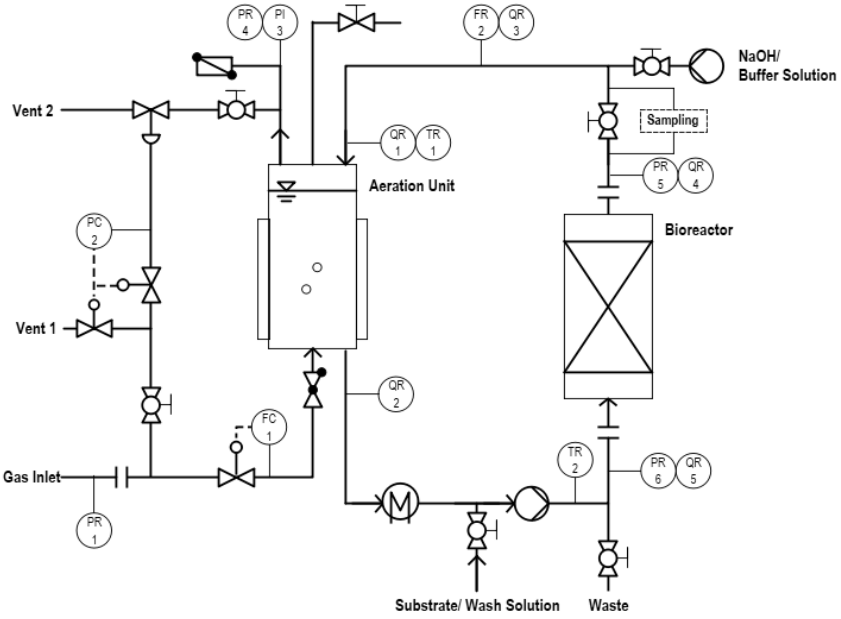

Fig. 3.1 Piping and instrumentation diagram of the developed aerated high-pressure reactor concept.

heat exchanger, maintaining the reaction medium's temperature between $T = 10$ to 40 ± 1 °C.

Situated in a bypass behind the bioreactor, a HPLC valve (6 Port 2 Pos, VICI Valco Instruments, Houston, USA) is integrated for sample extraction. This valve channels fluid through a sampling loop ($V = 250$ µl), and, by altering the valve's position and employing a programmable syringe pump (LA 100, Landgraf Laborsysteme HLL GmbH, Langenhagen, Germany), samples from the loop can be transferred into an HPLC vial for analysis. Additionally, the system is designed for the in-operation infusion of liquids into the reaction medium, using a pressure-resistant syringe pump (D500, Teledyne ISCO, Lincoln, USA) to adjust the pH value of the reactor. A control cabinet and a computer equipped with the WinErs process control system (Ingenieurbüro Dr.-Ing. Schoop GmbH, Hamburg, Germany) complement the control of the reactor. This system gathers and logs sensor data, managing time-dependent processes, and upholds critical operational parameters via control loops throughout the experimental phase.

The aeration unit saturates the liquid with oxygen for the enzymatic reaction. The aeration unit is a bubble column ($V_{bc} = 38$ ml) operated in counter-current flow (Figure 3.2). It features an observation window for optical analysis under pressure, enhancing the capability to monitor the aeration process directly. The liquid enters from the top of the cell and exits at the bottom. The gas phase is injected through a capillary ($d_n = 1.8$ mm) situated at the base of the viewing cell. The capillary is precisely aligned within the aeration unit using a centering ring. For oxygen saturation of the liquid phase, technical compressed air (79 % N_2, 21 % O_2, oil-free, Westfalen AG, Münster, Germany) is utilised. Conversely, nitrogen (purity 5.0, Westfalen AG, Münster, Germany) can be used to strip oxygen from the liquid phase.

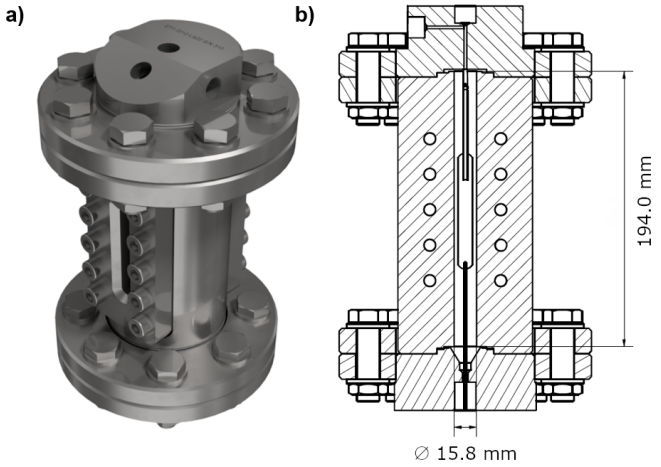

Fig. 3.2 **a)** Isometric view of the aeration unit with observation window **b)** Sectional view through the aeration unit.

Gas flow through the capillary is precisely regulated by a mass flow meter (EL-FLOW F111B, Bronkhorst, Ruurlo, Netherlands), ensuring a consistent volume flow rate between $\dot{V}_g = 3.5$ to 85.0 ml s^{-1}. To accommodate varying temperature and pressure conditions, a mass flow meter is employed instead of a volume flow meter due to its higher accuracy, which is essential for reproducible measurements in dynamic environments.

System pressure is regulated by the gas supply, with pressure adjustments made in the headspace of the bubble column. The column's top is outfitted with instruments for continuous pressure management, including a pressure transmitter (A-10, WIKA, Klingenberg am Main, Germany) for ongoing monitoring, a rupture disc for emergency pressure release, and

a back pressure regulator (Pressure Control Solutions, Veenendaal, The Netherlands) for controlling the system pressure. The regulator, utilizing a membrane, adjusts the pressure within a range of $p = 0.3$ to 15 ± 0.01 MPa with the back pressure on the membrane set by a process pressure regulator (P-822 CV, Bronkhorst, Ruurlo, Netherlands).

The benefits of using immobilized enzymes were highlighted in Chapter 2.2.2, leading to the selection of a packed bed reactor as the cornerstone of the bioreactor design. The reactor consists of a cylindrical vessel measuring $d_{br} = 41$ mm inner diameter and $h_{br} = 115$ mm in height, as shown in Figure 3.3. The reactor's lid plugs are engineered with centered holes, each equipped with a continuous thread, enhancing the bioreactor's versatility for testing innovative carrier structures. This includes both periodic open cell structures (POCS) and traditional particulate porous carrier materials, facilitated through the use of sintered stones.

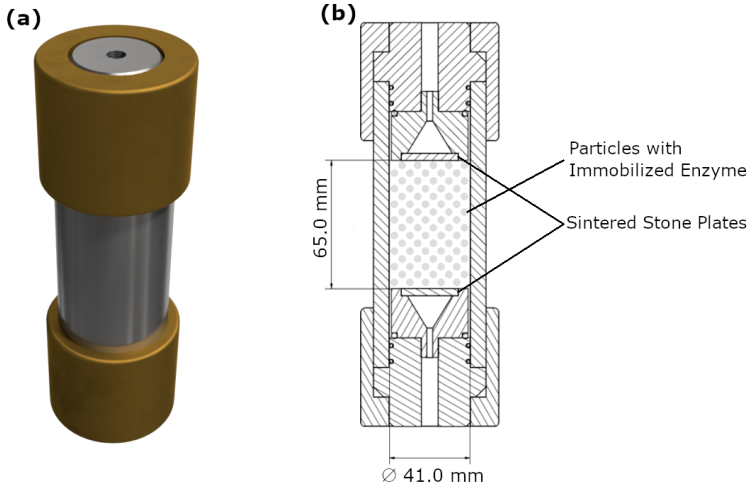

Fig. 3.3 **a)** Isometric view of the bioreactor **b)** Sectional view through the bioreactor with particle retention.

3.2 Optical Measurement Technique

The measurement points QR 1, 2, 4, and 5 in the P&ID (Figure 3.1) are equipped with oxygen probes (DP-PST3, PreSens Precision Sensing GmbH, Regensburg, Germany) and PT 100 temperature sensors, housed within crosspieces. These conical dipping probes are specifically designed for integration into cutting ring fittings (Figure 3.4 A), commonly used

in high pressure technology. The probes feature a window resistant to pressures up to 120 MPa, allow optical access into the reactor. The sensor, featuring a luminophore embedded within an adhesive polyester spot (Figure 3.4 B), is affixed to the pressurized side of the window. Conversely, on the window's opposite side, a fibre optic cable is securely attached, serving as a conduit to the transmitter.

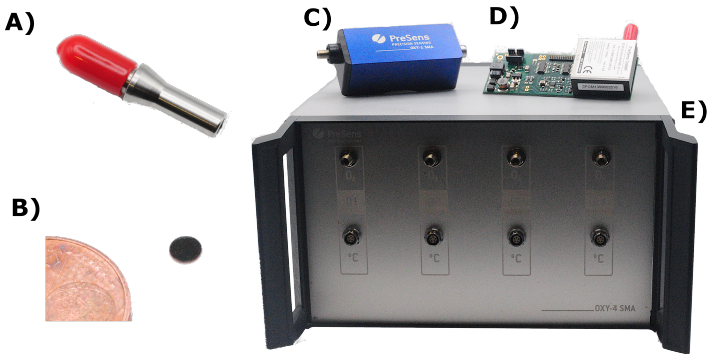

Fig. 3.4 Key components of optical oxygen measurement technology. A) Conical dipping probe B) Sensor spot, shown next to a 1-cent coin for scale C) Single-channel transmitter Oxy SMA 1 D) Electro-optical module EOM-O_2-mini E) Multi-channel transmitter Oxy SMA 4.

For the analyses conducted in this study, three devices from PreSens Precision Sensing GmbH (Regensburg, Germany) are employed: a single-channel oxygen measurement device (OXY-1, Figure 3.4 C), a single-channel electro-optical module (EOM-O2-mini, Figure 3.4 D), and a multichannel measurement device (OXY-4 SMA G2, Figure 3.4 E). These devices utilize LEDs to excite the luminophore in the sensor spots and capturing the fluorescence response. The EOM is designed for direct integration to the process control system, while the other measurement devices are connected to a computer running PreSens Measurement Studio 2 (version 3.0.0.1353) for data analysis. This software translates the phase shift into relative or absolute oxygen concentrations using a modified Stern-Volmer relationship, which adjusts for temperature and pressure conditions at the sensor, analogous to the representation shown in Figure 2.14

A similar method is adopted for monitoring the pH value at measuring point QR 3. In this case, a pH-sensitive luminophore is utilised, which also varies in the excitation wavelength. Consequently, a specific pH-sensitive sensor spot (DP-HP5, PreSens Precision Sensing

GmbH, Regensburg, Germany) and a pH-specific electro-optical module (EOM-pH-mini, PreSens Precision Sensing GmbH, Regensburg, Germany) is employed.

A separate experimental setup was used for the calibration of the oxygen sensors to ensure precise characterization of their response to varying pressures. This setup, developed in collaboration with Eurotechnica GmbH (Bargteheide, Germany), enabled the preparation of measurement solutions with accurately defined dissolved oxygen concentrations at different pressures, facilitating a detailed evaluation of the optical oxygen sensor's performance under high pressure conditions. The piping and instrumentation flow diagram of this configuration is presented in Figure 3.5.

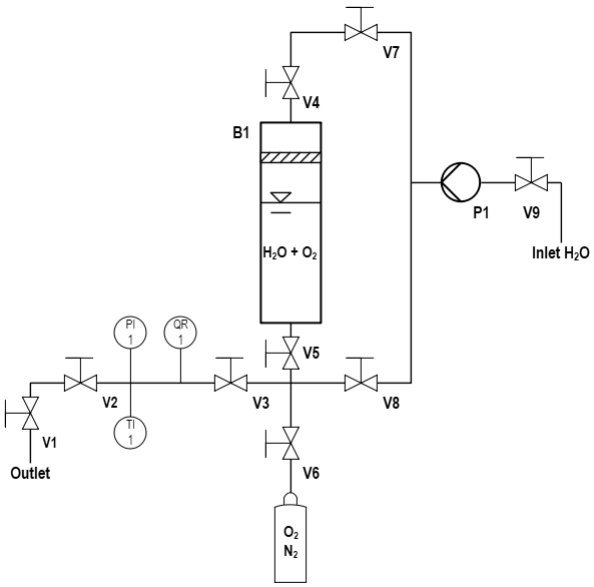

Fig. 3.5 Piping and instrumentation diagram of the laboratory setup used for analysing the optical oxygen sensors under varying pressure conditions.

The setup includes three main components: a syringe pump (D260, Teledyne ISCO, Lincoln, USA) for precise fluid supply, a swiveling piston accumulator (300cc, Proserve Engineering GmbH, Lüneburg, Germany) for solution mixing, and a measuring section for data acquisition. After achieving thermodynamic equilibrium, the prepared solution is passed through the measuring section, which houses a pressure sensor (PA-23, KELLER Druckmesstechnik AG, Winterthur, Switzerland), a thermocouple, and the previously shown

optical oxygen sensor model DP-PST3. Signal processing is conducted using the OXY-1 SMA single-channel measuring device (PreSens Precision Sensing GmbH, Regensburg, Germany).

3.3 Model Reaction System

As highlighted in the objectives of this thesis, a primary aim is to demonstrate the functionality of the developed setup by exploring the process intensification of an enzymatic reaction facilitated by increased gas solubility under pressure. Thus, the reactor's effectiveness is corroborated through an enzymatic model reaction. The selected reaction should be transferable to other gas-liquid biotransformations, underscoring the broad potential for process intensification via the application of high pressure. Oxidation reactions, especially involving oxygenases and oxidases, are of particular interest due to their industrial significance. Oxygenases can incorporate one or two oxygen molecules into a substrate with the aid of nicotinamide (NADH or NADPH) co-factors. However, the relatively high cost of these co-factors and the need for their intricate regeneration through secondary reactions challenge their economic viability. On the other hand, oxidases can directly utilize molecular oxygen as an electron acceptor, producing water or hydrogen peroxide as by-products without requiring expensive co-factors. Analysis from the Braunschweiger Enzym Datenbank (BRENDA) indicates that the oxygen affinity constant K_{MO} for many oxidases surpasses the maximum oxygen solubility of 0.26 mM ($T = 25$ °C, $p = 0.1$ MPa), suggesting that their activity is limited by the available oxygen.

Besides these prerequisites, factors like high enzyme activity, stability, and a thorough understanding of enzyme kinetics are vital for an exhaustive evaluation of enzyme behavior. A model reaction that adheres to these standards is the oxidation of glucose to D-gluconic acid by glucose oxidase. This process, illustrated in Figure 3.6, entails the enzymatic oxidation of glucose by molecular oxygen into D-glucono-δ-lactone, which then undergoes non-enzymatic hydrolysis to form D-gluconic acid.

3.3.1 Reaction Conditions for the Enzymatic Reaction

Alongside kinetic data, factors such as pH, temperature, and their respective deactivation effects are crucial in designing and interpreting the enzymatic experiments. Thomas provided a detailed characterization of glucose oxidase obtained from *Aspergillus Niger* [Tho21].

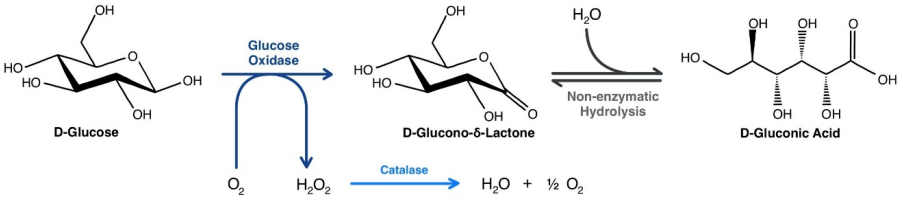

Fig. 3.6 Scheme of the chemoenzymatic synthesis of D-gluconic acid from D-glucose and molecular O_2 by glucose oxidase and H_2O_2 depletion by catalase.

The enzyme's activity and deactivation, influenced by pH and temperature, are displayed in Figure 3.7.

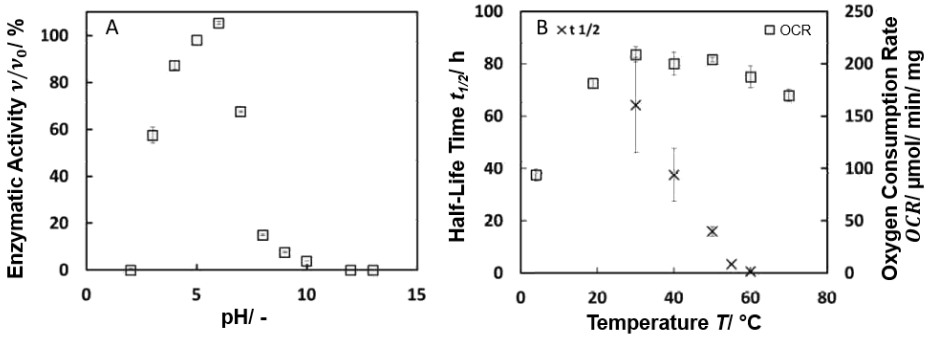

Fig. 3.7 Characterization of glucose oxidase (GOx) for pH sensitivity, oxygen consumption, and temperature stability. Reaction conditions: 0.021 mM o-dianisidine, 10 mM Na-acetate buffer at pH 5.3, 1 wt.% D-glucose, measurement at 520 nm, $T = 35$ °C for pH investigation, with concentrations of 20 U ml^{-1} for both GOx and catalase.

This information enables the identification of an optimal operating point for the experiments. Balancing enzyme stability and activity, a temperature of 35 °C and a pH of 5.4 emerge as the ideal conditions. To mitigate enzyme inhibition by the produced hydrogen peroxide, an sufficient quantity of catalase is added to the reaction mixture. Catalase effectively decomposes hydrogen peroxide into oxygen and water. This addition not only alters the overall reaction equation (as shown in Figure 3.5) but also effectively halves the oxygen requirement of glucose oxidase.

3.3.2 Enzyme Immobilisation

For the reactor design, the enzymes are introduced into the bioreactor in an immobilized state. This was achieved in close collaboration with the Institute of Technical Biocatalysis at TUHH. The institute provided expertise in enzyme immobilization techniques and contributed to the development and optimization of the methodology used in this study. The established immobilization protocol ensured a consistent supply of immobilized enzyme material for all experiments. To circumvent enzyme leaching under the specified conditions, a covalent immobilization method was chosen. The method uses commercially available porous polymethacrylate carrier particles with an epoxy-functionalised surface (ReliZyme™ HFA-403 from Resindion) as the immobilization medium. This technique, originally established by [Bol19], has been adapted and refined. It employs multi-point covalent bonding between the amino groups of the enzyme and the epoxy groups on the carrier particles' surface. To achieve immobilization, a solution containing 0.25 g l^{-1} glucose oxidase in a 100 mM sodium acetate buffer (pH 5.4) is prepared. Then, 10 g of the dry carrier particles are introduced into this enzyme solution. The mixture is agitated at 4 °C for 20 hours to ensure thorough immobilization. The immobilization yield, which ranges from 95 % to 99 % depending on the batch, proves to be consistently reproducible. Yield determination is carried out photometrically using a UV-Vis photometer, measuring the protein content in the enzyme solutions at 280 nm.

Chapter 4

Experimental Methods

This chapter outlines the methodology employed to explore the phenomena under study and the approach for data analysis. The investigation is divided into three principal sections. Initially, the focus is on evaluating the behaviour of optical oxygen sensors under pressure, which lays the groundwork for utilizing these sensors in experimental procedures. The subsequent section is dedicated to characterising the hydrodynamics and mass transfer efficiency of the aeration unit. In the final section, active oxidase is incorporated into the reactor to analyse its performance under various operational pressures.

4.1 Examination of the Optical Oxygen Sensors

The aim of studying the optical oxygen sensors was to verify their operational integrity under pressure, ascertain the accuracy of their measurements, and evaluate their suitability for experiments to be performed in the developed reactor. This involved testing the sensor' response to pressure variations and performing calibration measurements under different operating pressures.

4.1.1 Alternating Compressive Stress on the Measurement Behaviour

The examination of pressure fluctuation effects was conducted using the reactor setup described in Chapter 3.1. Prior to each experiment, the setup was outfitted with new sensor spots and filled with demineralized water. During the experiments, technical compressed air was used to vary and maintain the pressure within the reactor. A total of 24 alternating pressure cycles were conducted, with pressures oscillating between 0.5 and 5.0 MPa. An example of the sequence of two cycles is shown in Figure 4.1. Each cycle consists of a 60-minute phase at 0.5 MPa, followed by another 60-minute phase at 5.0 MPa. The pressure

profile in the reactor system is represented by a dashed line. The interval between pressure changes was carefully selected to ensure complete oxygen saturation in the medium and equilibrium between the polymer matrix of the sensor spot and the measurement medium. This is also evident in the displayed data from the oxygen sensor, represented by a solid line. In comparison to the pressure profile, the oxygen sensor data indicate that a significantly longer period is required to reach a steady state.

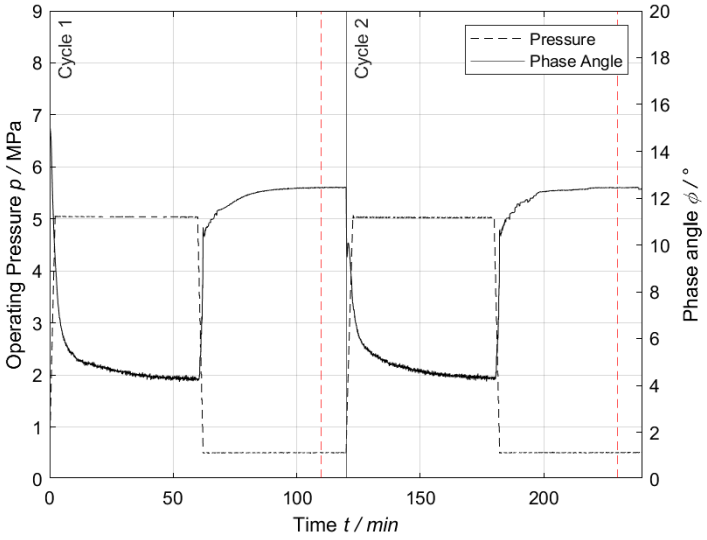

Fig. 4.1 Course of pressure in the test setup during a cyclic pressure load ranging from 0.5 to 5.0 MPa, alongside the corresponding phase angle measurements obtained by the optical oxygen sensor.

This study examines the compression phases, as they may induce structural modifications in the polymer matrix. Additionally, the decompression phases are analysed, since the rapid outgassing of oxygen could compromise the integrity of the polymer. To simulate these conditions, two distinct pressure gradients of 0.5 and 2.0 MPa min^{-1}, are applied. To guarantee precision and reliability of the results, each measurement point was replicated with three new sensor spots.

Throughout the measurement process, both the phase angle shift and its luminescence intensity were consistently recorded. To evaluate variations in the steady-state signals, the data were averaged over the final 10 minutes of each cycle. The start of this interval

is indicated in Figure 4.1 by a red dashed line, while the end corresponds to the cycle's conclusion, marked by a solid line. This approach enabled a detailed comparison of the signals and their temporal evolution. To further complement the analysis of the measurement signals, the surfaces of the sensor spots were examined both before and after the experiments using a 3D Confocal Laser Scanning Microscope (VK-X160K, Keyence, Osaka, Japan).

4.1.2 Calibration Process of the Optical Oxygen Sensors

The calibration of oxygen sensors was conducted using the setup detailed in Section 3.2. The process began with the preparation of a measurement solution in the piston accumulator. Initially, the accumulator was completely emptied, followed by the precise addition of 200 ml of solution through a syringe pump directly connected to it. The pump was then switched to actuate the hydraulic piston of the accumulator. The pressure was adjusted using the regulator on the oxygen cylinder, and the valve leading to the accumulator was opened. A defined volume of oxygen was then drawn into the accumulator via the syringe pump and the piston's movement, after which the system was sealed. To accelerate the dissolution process, the accumulator was periodically agitated while being monitored with a pressure sensor. Oxygen dissolution was considered nearly complete only when no further changes in pressure were detected. For the highest oxygen concentrations, a dissolution period of approximately 15 hours was required. This approach enabled the creation of measurement solutions with oxygen concentrations ranging from 9.68 to 3332.81 mg l^{-1}.

Prior to the measurement, the measuring line is flushed with gaseous nitrogen to guarantee a complete absence of oxygen. Subsequently, the syringe pump is connected to the hydraulic section of the piston accumulator. The solution from the piston reservoir is then consistently fed, under constant pressure, through the measuring section towards the outlet. This procedure is maintained until the oxygen sensor indicates a stable reading. Ten distinct oxygen concentration levels were evaluated under pressure settings of 0.3, 2.5, 5.0, 7.5, 10.0, 12.5, and 15.0 MPa. To ensure the reliability of the test, the temperature was kept constant at 20 °C throughout the experiment. Each concentration level was measured three times at every pressure setting to confirm the accuracy and repeatability of the results.

4.2 Hydrodynamic Characterisation of the Aeration Unit

As part of the hydrodynamic characterization, the study includes the behaviour of the aeration unit under varying pressures. This examination seeks to elucidate the dynamics within the high pressure system, identifying key factors affecting aeration efficiency. The characterization process encompasses analyses of bubble size distribution and bubble flow regimes, which are pivotal in determining gas hold-up and the mass transfer area. Lastly, the volume-specific mass transfer coefficient is measured.

This study analyses the results from two complementary perspectives. First, the outcomes are examined in the context of the supplied mass flow, enabling an understanding within the framework of a mass balance. This approach clarifies the extent to which the introduced oxygen dissolves in the aqueous phase and is subsequently utilised by the enzyme. Second, by applying the ideal gas law, the effects of compression on the supplied gas flow under increased pressure are accounted for. The ideal gas law is expressed as

$$p \cdot V = Z \cdot n \cdot R \cdot T \tag{4.1}$$

where p is the pressure, V is the volume, n is the amount of substance in moles, R is the universal gas constant, and T is the temperature. The compressibility factor Z accounts for deviations from ideal gas behaviour, which become significant under high-pressure conditions. This adjustment ensures a more precise calculation of the gas flow and its compression effects in non-ideal conditions. This adjustment facilitates the examination of operating points within comparable flow regimes, thereby identifying effects that manifest independently of gas compression.

4.2.1 Analysis of the Bubble Regime and Bubble Size Distribution

To investigate the bubble flow dynamics, the setup was filled with demineralized water and kept at a stable temperature of 20 °C. Technical compressed air was supplied via a capillary, regulated by a mass flow controller. During the experiment, the mass flow was varied from 4 to 35 mg s^{-1}, while the pressure was methodically altered to specific values of 0.3, 2.5, 5.0, 7.5, 10.0, 12.5, and 15.0 MPa. A digital camera (D90, Nikon, Minota, Japan), equipped with a macro Nikkor lens (focal length 105 mm), captured 10 images per measurement point at 8 Hz. A high-power LED panel positioned behind the viewing cell enhanced contrast at the bubble interface, facilitating bubble identification. The observed bubble regime was

classified according to the flow regime characteristics detailed in Section 2.1.1.

To maintain consistent operation of the setup for prolonged periods, achieving a uniform bubble regime within the aeration cell was essential. Therefore, the mass flow levels connected to a homogeneous bubble regime were systematically scanned. The bubble size distribution was measured incrementally, with mass flow increments of 4.3 mg s^{-1}. At each measuring point, 300 images were captured, and the determination process was conducted in triplicate for accuracy. The bubble size distribution was derived from the images using the SOPAT evaluation software (v2.1.17.1623), which features a trainable algorithm for automatic recognition of spherical bubbles. An illustrative presentation of a raw image and its corresponding evaluation can be found in Figure 4.2.

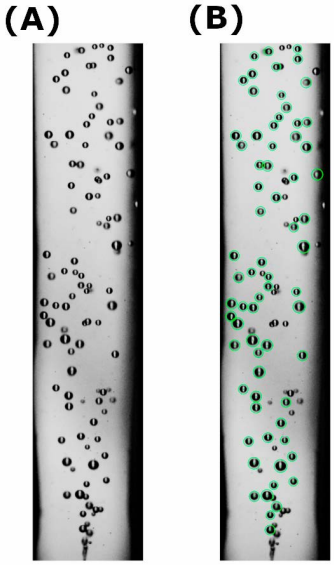

Fig. 4.2 **a)** Raw Image of the bubbly flow within the aeration unit **b)** Image processed by the SOPAT bubble recognition software. Detected and analysed bubbles are marked with a green circle.

The evaluation software determine the bubble diameter in pixels. To convert this data into millimetres, it's necessary to establish the ratio between pixels and millimetres on the focused plane. The known diameter of the capillary in focus is used as the reference for this conversion. As a result, a spatial resolution of 9.12 µm per pixel is determined for the

camera setup in use. Utilizing the derived bubble size distribution and the conversion factor, the Sauter mean diameter can be calculated using Equation 2.18.

4.2.2 Calculation of the Gas Hold-Up and Mass Transfer Area

Considering the narrow depth of the viewing cell (1 cm) and assuming that the bubbles are nearly spherical, it is feasible to estimate the gas hold-up ε_g effectively using the bubble size distribution identified earlier. This estimation involves multiplying the quantity of bubbles by their respective volumes, calculated based on their diameters. Performing this calculation across the entire size spectrum enables the determination of the gas volume, which is then compared to the known liquid volume in the bubble column, as described by

$$\varepsilon_g = \frac{\sum_i n_i \cdot (\frac{\pi}{6} \cdot d_{b,i}^3)}{V_{bc} \cdot n_{images}}. \tag{4.2}$$

Here, n_i is the number of bubbles of diameter $d_{b,i}$, V_{bc} is the volume of the bubble column, and n_{images} denotes the total number of images analysed. It's essential to note that the accuracy of determining the gas hold-up is heavily reliant on the quality of bubble detection and the resulting bubble size distributions. This method of gas hold-up determination has limitations, particularly in regions with non-spherical bubbles or areas with a very high bubble density, leading to overlapping. The volume-specific phase boundary area can be determined with precision using the established gas hold-up and Sauter diameter, as per Equation 2.7.

4.2.3 Determination of Mass Transfer Coefficient

Before each experiment, dissolved oxygen is removed from the liquid phase by purging with nitrogen until the oxygen saturation level falls below 1 mg l^{-1}. Subsequently, the system is aerated using technical compressed air until maximum oxygen saturation is achieved. The dissolved oxygen concentration is continuously monitored at a frequency of 0.33 Hz employing the optical oxygen measurement technology detailed in Section 3.2. To ensure consistency in the analysis of the mass transfer coefficient with hydrodynamic data, the same measurement points previously discussed are examined.

By monitoring the temporal evolution of oxygen concentration in relation to the saturation concentration (Section 2.1.3), the logarithm of the dissolved oxygen concentration can be plotted against time. This relationship, described by Equation 2.9, allows for the

determination of the mass transfer coefficient $k_l a$ through linear regression. For optimal accuracy, the linear regression is typically applied to the range between 20 % and 80 % saturation. At elevated pressures, this range may be limited due to the limited resolution of the optical sensors used.

4.3 Characterisation of Glucose Oxidase under Pressure

The oxidation of glucose into glucono-δ-lactone by glucose oxidase was studied in a batch process. These experiments were designed to examine the performance of the reactor setup and glucose oxidase under elevated pressure while ensuring consistent reaction conditions. This approach facilitated a comparison of enzyme behaviour across different pressure levels.

4.3.1 Experimental Procedure

Prior to conducting the experiments, glucose oxidase was added to the bioreactor, as detailed in Chapter 3.1. After incorporating the bioreactor into the experimental setup, the entire system was evacuated using a vacuum pump (E1M5, Edwards Vacuum, Burgess Hill, UK). To protect the porous particles from potential damage caused by evacuation, the pump's suction volume was regulated via a bypass. Once evacuated, the systemwas filled with a substrate solution containing 100 mM D-glucose dissolved in 100 mM sodium acetate buffer and adjusted to a pH of 5.4. To mitigate potential inhibition of glucose oxidase by hydrogen peroxide, catalase from *Corynebacterium glutamicum* was added to the substrate solution. Due to the high specific activity of the catalase stock solution (613.9 U mL^{-1}), the addition of only 2 µL to 250 mL of substrate solution was sufficient, corresponding to a total free catalase activity of $\leq$ 1 kU per experiment.

As preparations for the experiment were completed, the process control system was engaged to start the setup preparation and execution of the experiment. The initial step involved setting the desired process parameters within the setup. In this preparatory phase, the substrate solution was circulated through the reactor at a flow rate of 1.33 ml s^{-1} aiming to reach the targeted process temperature and pressure. Simultaneously, to inhibit any prior reaction between the substrate and glucose oxidase, gaseous nitrogen was continuously added into the substrate mixture. The oxygen concentration was tracked utilizing the installed optical oxygen sensors. Upon attaining the experimental conditions, the operational phase of the experiment commenced. At this juncture, all data points were logged by both the process

control system and the gas supply was switched from nitrogen to technical compressed air.

The introduction of oxygen into the system initiates the conversion of glucose into glucono-δ-lactone, which further hydrolyses into gluconic acid, leading to a decrease in the pH value. The employed buffer system mitigates this pH change. Once the buffer's capacity is exceeded, the pH starts to drop, adversely affecting enzyme activity. To neutralize the acidity and stabilize the pH, a 2 molar NaOH solution is injected into the bioreactor's outlet via a syringe pump. Recirculation through the aeration cell ensures thorough mixing and prevents potential deactivation of the immobilized enzymes due to the concentrated base. All chemicals used were of analytical grade, sourced from Roth (Karlsruhe, Germany) or Sigma-Aldrich (Vienna, Austria). Details of the substances and operational parameters utilised in the experiment are provided in table 4.1 below:

Table 4.1 Comprehensive Listing of Operational Parameters for Validation Experiments with Glucose Oxidase.

Parameter	**Value**	**Unit**
Operating Temperature T	35.0 ± 1	°C
Operating Pressure p	0.3 - 15.0 ± 0.01	MPa
Liquid Volume Flow $\dot{V}_l$	1.3 ± 0.03	ml s^{-1}
Gas Mass Flow $\dot{V}_g$	6.49 ± 0.04	mg s^{-1}
Substrate	100 mM D-glucose 100 mM sodium acetate buffer	
Enzyme	glucose oxidase from *Aspergillus Niger* Catalase from *Corynebacterium glutamicum*	
pH value	5.4	

4.3.2 Data Evaluation

For the analysis of these experiments, two distinct measurement techniques were employed. The first involves data from optical oxygen sensors, which facilitate the monitoring of oxygen mass flows as outlined in the balance shown in Figure 4.3.

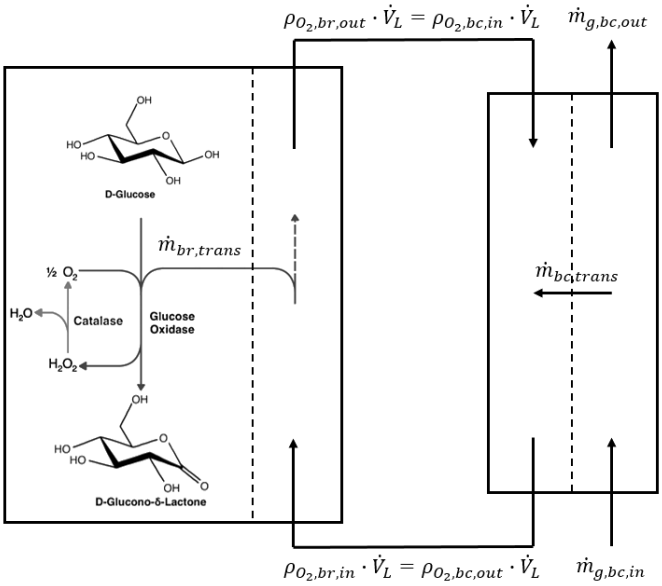

Fig. 4.3 Defined system boundaries for the calculation of oxygen mass flows in the reactor setup.

Within the context of the mass balance, three specific oxygen mass flows — or their ratios — are of particular interest. These include the oxygen mass flow introduced into the aeration unit $\dot{m}_{g,bc,in}$, calculated as

$$\dot{m}_{g,bc,in} = \dot{m}_{air} \cdot w_{O_2} \tag{4.3}$$

where $\dot{m}_{air}$ represents the total air mass flow and w_{O_2} is the oxygen mass fraction in the air. The second is the oxygen mass flow transitioning from the gas phase to the liquid phase within the aeration unit $\dot{m}_{bc,trans}$, given by

$$\dot{m}_{bc,trans} = (\rho_{O_2,bc,in} - \rho_{O_2,bc,out}) \cdot \dot{V}_l. \tag{4.4}$$

Lastly, the oxygen mass flow utilised within the bioreactor $\dot{m}_{br,trans}$ is determined by

$$\dot{m}_{br,trans} = (\rho_{O_2,br,in} - \rho_{O_2,br,out}) \cdot \dot{V}_l \tag{4.5}$$

where $\rho_{O_2,br,in}$ and $\rho_{O_2,br,out}$ are the oxygen concentrations at the inlet and outlet of the bioreactor, respectively. The oxygen generated from hydrogen peroxide decomposition by catalase is not accounted for as a separate mass flow in this balance. In the examination of

mass flows, the mass flow within the bioreactor $\dot{m}_{br,trans}$, is of primary interest. This flow metric serves as an indicator of oxygen utilization and, by extension, enzyme activity. A pivotal point in this analysis is reached when oxygen concentrations at the reactor's inlet and outlet align, leading to a reduction in the oxygen mass flow. This indicates the cessation of oxygen uptake by the immobilised enzyme bed and suggests a decline in enzymatic activity.

Furthermore, beyond analysing instantaneous mass flows and pinpointing potential process bottlenecks, it is possible to quantify the total oxygen mass supplied, m_{supp}, by integrating the instantaneous mass flow $\dot{m}_{g,bc,in}(t)$ over the duration of the experiment, as shown in the following equation

$$m_{supp} = \int_{t_o}^{t} \dot{m}_{g,bc,in}(t)\, dt. \tag{4.6}$$

Similarly, the total oxygen mass consumed within the bioreactor, m_{conv}, can be determined by integrating the instantaneous oxygen mass flow $\dot{m}_{br,trans}(t)$ over the same time period, expressed in the following equation

$$m_{conv} = \int_{t_o}^{t} \dot{m}_{br,trans}(t)\, dt. \tag{4.7}$$

The converted mass flow, m_{conv}, allows for a direct comparison with the stoichiometric oxygen demand required for the reaction. By evaluating m_{conv} alongside the supplied oxygen mass flow m_{supp}, it's feasible to establish an efficiency factor, η_{O_2} that reflects the effectiveness of oxygen utilization within the system. This factor quantifies the effectiveness of oxygen utilization within the system and is calculated as

$$\eta_{O_2} = \frac{m_{supp}}{m_{conv}}. \tag{4.8}$$

This provides a quantitative measure of how efficiently the oxygen supplied to the reactor setup is being consumed in the enzymatic reactions. Within the scope of a secondary measurement approach, liquid samples are collected at 2.5-minute intervals throughout the experiment for analysis. These samples are extracted from the setup via a bypass incorporating an HPLC valve (6 Port 2 Pos, VICI Valco Instruments, Houston, USA) equipped with a sampling loop. A programmable syringe pump displaces the sampling loop's volume (250 µl) with 1.5 ml of sodium acetate buffer (100 mM, pH 5.4), which is then transferred into an HPLC vial.

The samples undergo HPLC analysis using a NUCLEODUR® column (3 µm, 110 Å, RP C18, Macherey-Nagel, Düren, DE) to track the formation of D-gluconic acid. The process is conducted at a constant temperature of 25 °C, utilizing an aqueous mobile phase with 20 mM phosphoric acid (pH 2.0). The flow rate is maintained at 1.0 ml min^{-1}, and gluconic acid's retention time is observed to be approximately 0.8 min, detected by a DAD detector at 210 nm. The concentration of glucose, ρ_{GL} is inferred from the peak area integration using prior calibration. The conversion rate of glucose, X_{GL}, is subsequently calculated using the initial glucose concentration, $\rho_{\mathrm{GL},0}$, as outlined in

$$X_{Gl} = \frac{\rho_{Gl,0} - \rho_{Gl}(t)}{\rho_{Gl,0}}. \tag{4.9}$$

Chapter 5

Experimental Results and Discussion

In this chapter, the experimental results are presented and analysed in detail.The structure of this chapter reflects the interconnected nature of the findings, which progressively build upon each other. It encompasses the investigation of oxygen sensors, the study of mass transport within the aeration unit, and the impact of increased oxygen concentration in the substrate on the enzymatic reaction.

The first part evaluates the suitability of oxygen sensors under pressure. Key questions addressed include the stability of the sensors under varying pressure conditions, the maximum measurable oxygen concentration, and the sensitivity and accuracy of the sensors when exposed to elevated pressures. Building on these findings, the second part examines mass transfer under pressure. This analysis includes changes in critical parameters (Section 2.1) such as the Sauter mean diameter, gas hold-up, and mass transfer coefficient as a function of pressure. The third part investigates the enzymatic reaction using glucose oxidase as a model system (Section 3.3). Here, the different oxygen mass flows in the reactor are analysed to determine whether increased oxygen availability intensifies the reaction process. Finally, the experimental results are contextualized through modelling, which evaluates whether further increases in oxygen concentration can lead to an additional enhancement of the reaction rate. This holistic approach ensures that the findings are systematically linked and provide a comprehensive understanding of the studied processes.

5.1 Behaviour of Oxygen Sensors under Pressure

This subsection examines the system for optical measurement of dissolved oxygen concentration, as introduced in Section 3.2, under pressures of up to 15.0 MPa. This analysis aims to systematically evaluate the sensor's performance and limitations in high-pressure applications. This section addresses the following key aspects:

- The impact of compression and decompression cycles on the structural integrity of the sensor spot or polymer matrix, potentially affecting precision and accuracy.
- The maximum measurable dissolved oxygen concentration, considering the limitations imposed by the sensor's optical components and the solubility of oxygen in the medium under high-pressure conditions.
- The sensitivity and accuracy of the sensor under high-pressure conditions, focusing on the influence of pressure-induced changes in the sensor spot when operating at elevated pressures.
- The validity of the linear correlation between the measured phase angle, φ, and the calculated dissolved oxygen concentration, c_{O_2}, as previously demonstrated in Section 2.3.1, in pressurized environments.

5.1.1 Stability under High Pressure Conditions

The assessment of pressure stability was conducted as described in Chapter 4.1.1. Figure 5.1 below displays the evolution of the phase angle throughout the cyclic testing. This figure highlights the response of two sensors, each subjected to distinct regular pressure change rates of 0.5 and 2.0 MPa min^{-1}, respectively. The representation includes the progression of the first cycle, overlaid with the 8^{th}, 16^{th}, and the final 24^{th} cycles. The dashed line marks the commencement of the pressure reduction from 5.0 to 0.5 MPa. The graph demonstrates that the course of the phase angles φ remains nearly identical, regardless of whether the pressure change rate is 0.5 or 2.0 MPa min^{-1}.

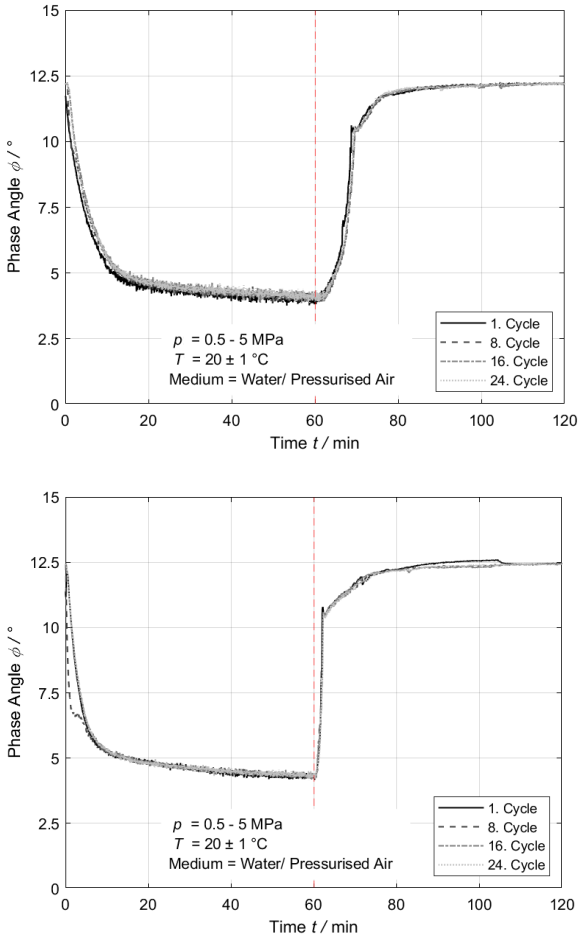

Fig. 5.1 Comparative representation of the results from alternating pressure loading tests with a pressure gradient of (top) 0.5 MPa min^{-1} and (bottom) 2.0 MPa min^{-1}.

Throughout the cycles, no notable variations of the sensor behaviour are observed, either in the dynamic shifts or in the steady states.

Additionally, the graph highlights that pressure alterations, visible starting at $t = 0$ and $t = 60$ min (marked with a red dashed line), promptly influence the measured values. A quasi-steady state, characterized by only minimal changes in the phase angle, is typically reached at $t = 20$ min and $t = 80$ min. This observation is supported by an analysis of the average phase angle across all sensors and cycles, as illustrated in Figure 5.2.

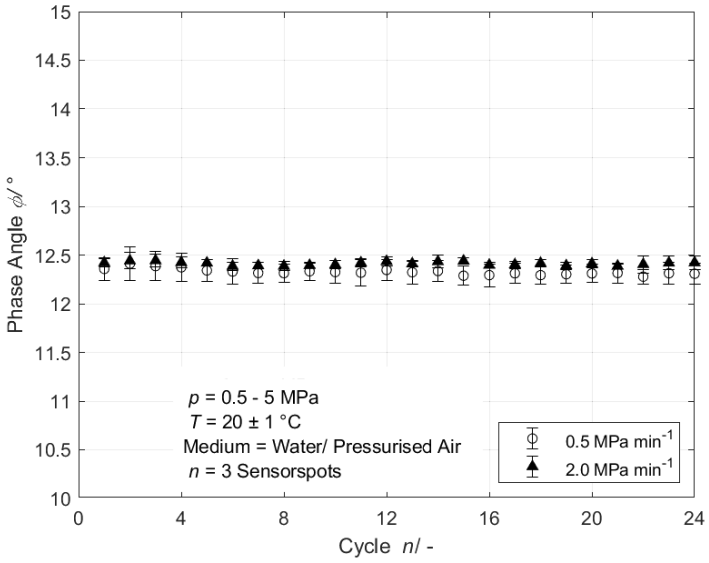

Fig. 5.2 Evolution of the quasi-stationary phase angle φ during cyclic alternating pressure load testing at rates of 0.5 MPa min^{-1} and 2.0 MPa min^{-1}.

The phase angle φ is an intrinsic parameter, predominantly influenced by the diffusion of oxygen into the polymer. Thus, relying solely on this parameter makes it difficult to derive detailed insights into the sensor spot's condition. However, fluorescence intensity I can also be leveraged in this context. Similarly, according to Equation 2.39, it can be used to determine the oxygen concentration. Nonetheless, fluorescence intensity is influenced by several factors, such as the LED's excitation intensity, temperature, and the even distribution of the fluorescent dye within the polymer structure.

The fluorescence intensity's dynamic behaviour generally aligns with that of the phase angle, as depicted in Figure 5.1, and is therefore not presented separately in this context. While the overall behaviour is similar, notable deviations become apparent, particularly in the quasi-steady states. This observation is supported by an analysis of the mean fluorescence intensity across all sensors and cycles as shown in Figure 5.3.

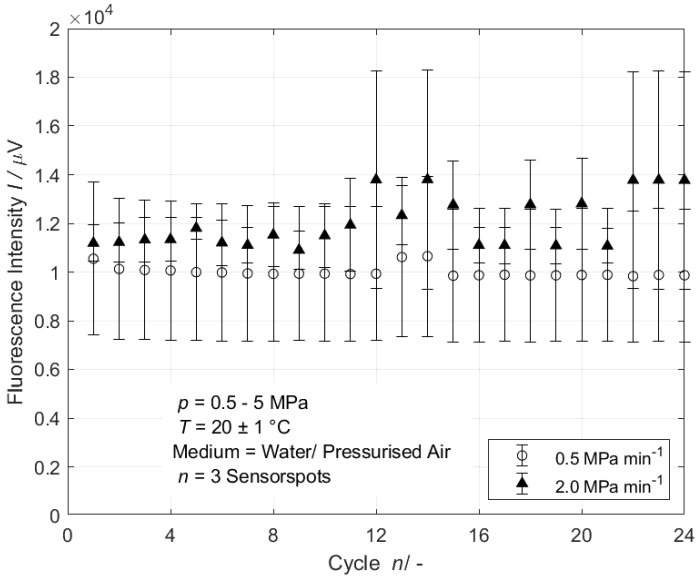

Fig. 5.3 Evolution of the quasi-stationary fluorescence intensity I during cyclic alternating pressure load testing at rates of 0.5 MPa min^{-1} and 2.0 MPa min^{-1}.

Analysis of Figure 5.3 reveals variations in measurements, as indicated by larger error bars for fluorescence intensity. This variance is attributed to the diverse behaviour of individual sensor spots. A detailed analysis reveals that the measured fluorescence intensity changes with increasing pressure change rate and cycling. At a pressure change rate of 0.5 MPa min^{-1},

the average fluorescence intensity remains relatively stable. However, closer examination of the data indicates a slight, near-linear decrease in fluorescence intensity, ranging from 10,500 µV to just under 9,860 µV. In contrast, at a pressure change rate of 2.0 MPa min^{-1}, the changes in measurement behaviour become more pronounced, with significant fluctuations in fluorescence intensity observed. The laser scanning microscope images shown in Figure (5.4) captured before and after the measurement provide additional insights and offer a potential explanation for the observed changes in fluorescence intensity.

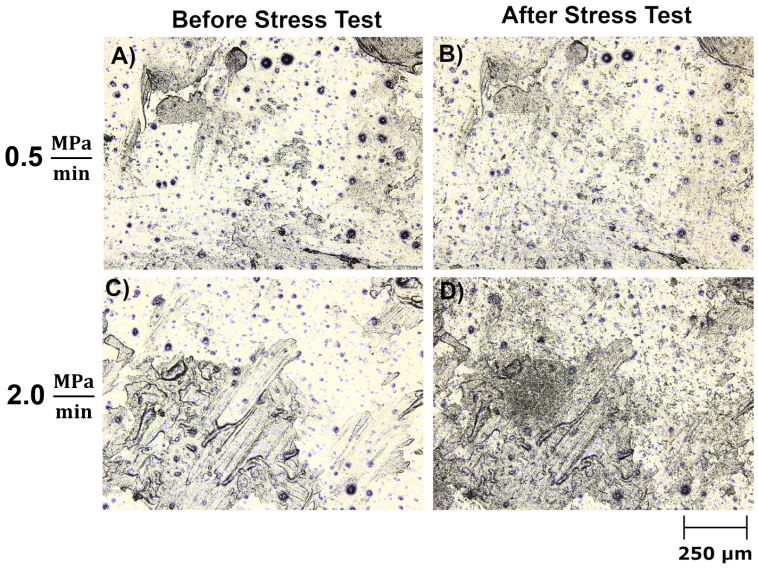

Fig. 5.4 Laser scanning microscope images of the sensor spot before and after cyclic pressure loading. Images are presented for two loading rates: A) and B) at 0.5 MPa min^{-1}; C) and D) at 2.0 MPa min^{-1}.

While the images captured at a pressure gradient of 0.5 MPa min^{-1} show only minor changes after the experiment, a significant alteration is evident at a pressure gradient of 2.0 MPa min^{-1}. Across the entire image area, a pronounced grey discolouration is visible, which, upon closer inspection, can be identified as cracks and pores in the surface. This provides a plausible explanation for the observations in Figure 5.3, where a significant change in fluorescence intensity is observed at higher pressure gradients. At 0.5 MPa min^{-1}, the polymer's surface structure remains largely intact. In contrast, at 2.0 MPa min^{-1}, the sensor surface undergoes substantial changes, potentially resulting in the direct exposure and loss of fluorescent dye.

5.1.2 Calibration under High Pressure Conditions

In the previous section, it was determined that the sensor spots deliver stable and reproducible outcomes under the influence of repeated pressure changes. To further investigate the precision of the oxygen sensor and examine the relationship between the phase angle and oxygen concentration beyond 8 mg l^{-1}, the method described in section 4.1.2 was utilised. Figure 5.5 presents the results of this exploration across different measuring solutions and pressures ranging from 0.3 to 10.0 MPa.

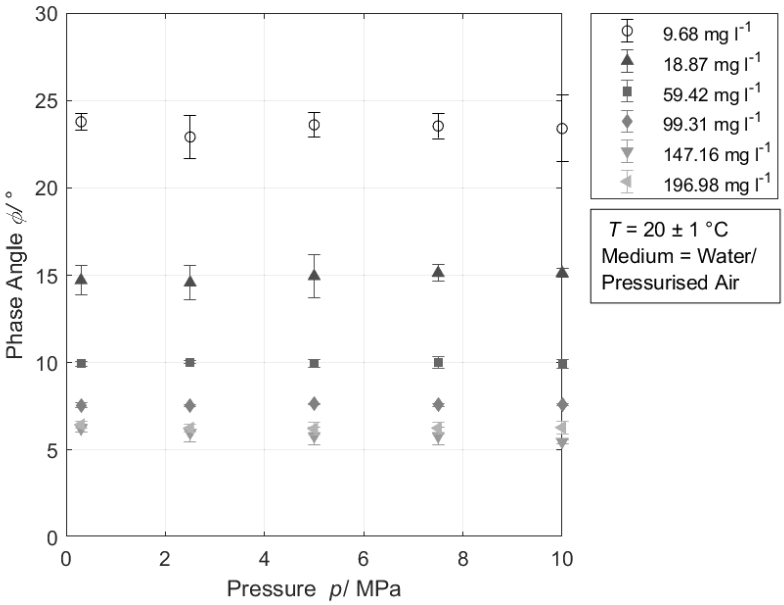

Fig. 5.5 Investigation of different measurement solutions with oxygen concentrations ρ_{O_2} ranging from 9.68 mg l^{-1} to 196.98 mg l^{-1} Using the Optical oxygen sensor at pressures between 0.3 MPa and 10 MPa.

The analysis of measurement data indicating that the phase angle φ reliably corresponds to a specific oxygen concentration c_{O_2}, regardless of pressure. This analysis confirms that higher phase angles correspond to lower oxygen concentrations. For example, at a concentration of 9.68 mg l^{-1}, the phase angle is approximately 23.4° and decreases as the oxygen concentration increases. Therefore at 196.98 mg l^{-1}, the phase angle is reduced to 6.29°. The phase angle reduction does not follow a linear trend with increasing oxygen concentration. This observation suggests that the resolution, and consequently the precision

of the sensor, diminishes with rising oxygen concentration. To refine this observation, additional measurement solutions were prepared, and their respective phase angles evaluated. In these further experiments, a total of 22 additional test solutions were examined, spanning concentrations from 9.68 mg l^{-1} to 3332.81 mg l^{-1}. Figure 5.6 displays the relationship between phase angle and oxygen concentration for a range extending up to 400 mg l^{-1}.

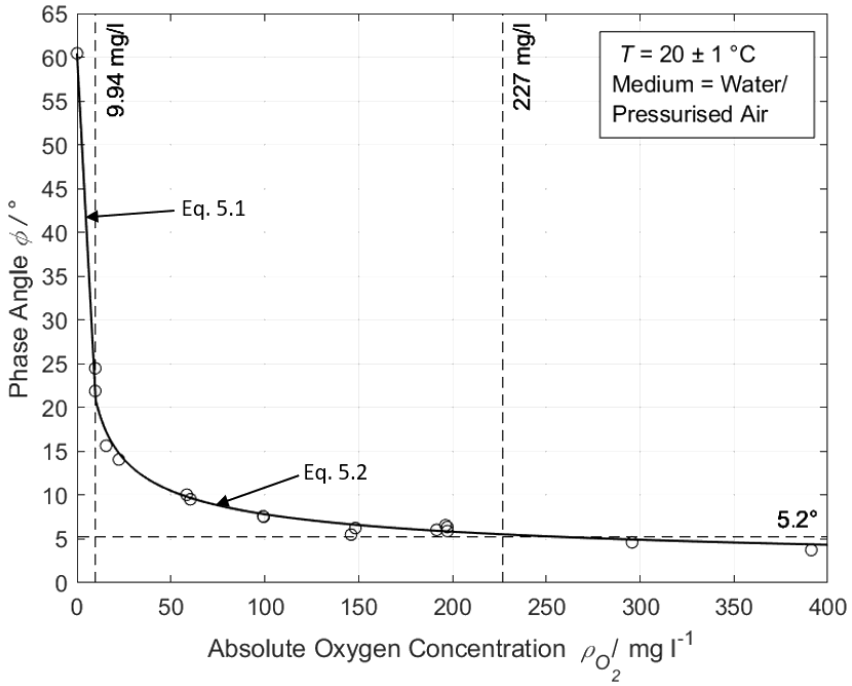

Fig. 5.6 Relationship Between Phase Angle and Absolute Oxygen Concentration ρ_{O_2} Ranging from 0 to 400 mg l^{-1}.

Analysing the relationship between the phase angle and oxygen concentration, the data can be divided into three distinct intervals. In the initial interval, ranging from 0 to 9.68 mg l^{-1}, a linear decrease is observed, consistent with the Stern-Volmer equation. This interval represents the sensor's highest resolution capability. Within this range, the relationship between the phase angle φ and the absolute oxygen concentration ρ_{O_2} can be expressed as:

$$\rho_{O_2} = \frac{\varphi - 60.43}{-3.819}. \tag{5.1}$$

Beyond 9.68 mg l^{-1}, the behaviour of the phase angle is characterized by an exponential decrease, resulting in a continuous decline in resolution within this exponential range. Experiments have demonstrated that the optical oxygen sensor consistently provides reproducible and distinguishable results up to a phase angle φ of 5.3° this corresponds to an oxygen concentration of approximately 227 mg $^{-1}$. This concentration is reached at an oxygen partial pressure of approximately 5.8 MPa. Within this range, the relationship between the phase angle φ and the absolute oxygen concentration ρ_{O_2} can be expressed as:

$$\rho_{O_2} = (\frac{\varphi}{55.206})^{-2.359}. \tag{5.2}$$

Beyond this value, Equation 5.2 can still be applied; however, the graph flattens and becomes nearly horizontal. Past the concentration ρ_{O_2} of approximately 227 mg $^{-1}$, the sensor's capacity to resolve the oxygen concentration diminishes significantly. Slight variations in the phase angle, attributable to the accuracy limits of the transmitter hardware, lead to substantial discrepancies in the oxygen concentration readings. Table 5.1 provides an overview of the sensor's overall measurement behaviour, outlining these intervals, their mean resolution, and the corresponding equations.

Table 5.1 Tabular overview of the measuring ranges, resolution, and approximation approach of the optical oxygen sensor.

Concentration/ mg/l	**Phase Angle/ °**	**Average Resolution mg/°**	**Approximation**
[0, 9.68]	[60.43, 27.17]	3.436	Equation 5.1
[9.68, 227.0]	[27.17, 5.3]	0.099	Equation 5.2
> 255	< 5.3	< 0.00085	-

The approximations outlined in Table 5.1 serve as a benchmark for assessing the accuracy of the firmware algorithm that converts phase angle readings into absolute oxygen concentrations. The evaluation was conducted by using demineralised water, initially purged with nitrogen, then aerated with compressed air at a pressure of 2.5 MPa and 20 °C to achieve full saturation. For the highest accuracy of the oxygen sensors, a two-point calibration (0 % a.s.; 100 % a.s.) was executed under these specific conditions. The resulting graph 5.7 displays the absolute oxygen concentration as calculated by the firmware and the data generated with the approximation curve. Moreover, the graph incorporates the maximum oxygen solubility, computed based on Equation 2.25 for the given experimental conditions.

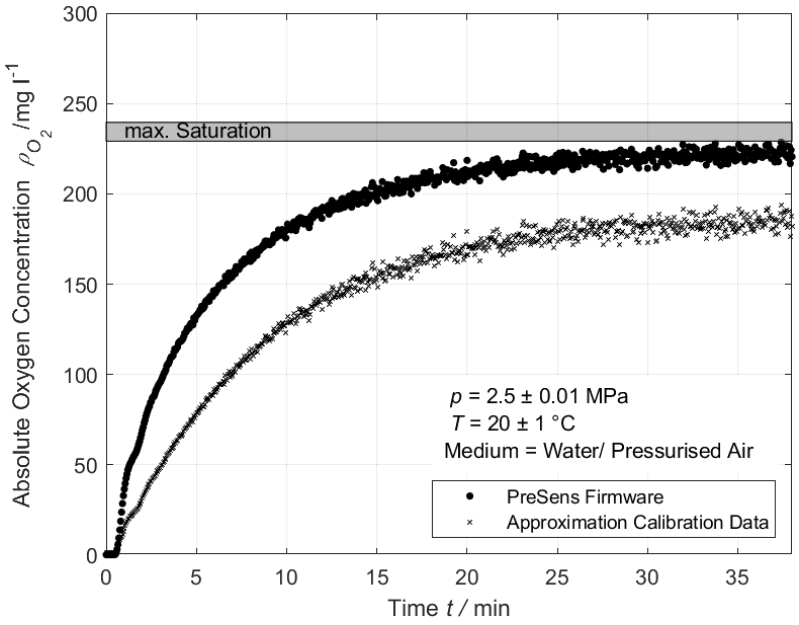

Fig. 5.7 Comparative analysis of PreSens firmware algorithm and the calibration-derived approximation for calculating absolute oxygen concentration. Reaction conditions: Saturation of distilled water with air at $T = 20$°C and $p = 2.5$ MPa.

The graph indicates that the approximation aligns well with concentrations up to 15 mg l^{-1}. Beyond this point, discrepancies between the firmware's output and the approximation become evident, with precision decreasing as oxygen concentration increases. The divergence between the curves raises questions about the measurement results' reliability. The firmware's algorithm matches the calculated maximum saturation for the set conditions quite closely, suggesting a better degree of accuracy. This observation may be attributed to the uniformity of the polymer and fluorescent dye within the sensor spots, as previously discussed. Variations in the phase angle of up to $\pm$ 0.4° within a batch can significantly affect measurements, especially at high oxygen concentrations where the exponential approximation leads to substantial deviations in the reported absolute oxygen concentration. Therefore, despite calibration efforts shedding light on sensor behaviour, a sensor-specific calibration at elevated pressures becomes essential for achieving the highest accuracy in oxygen concentration measurements.

5.1.3 Applicability of Optical Oxygen Sensors under Pressure

Based upon the knowledge gained within the preceding sections, it can be demonstrated that the sensor can be utilised with certain limitations under conditions exceeding atmospheric pressures and saturation concentrations. Consequently, it is suitable for measurements in the reactor setup. The stability study affirms that the repetitive cycles of compression and decompression do not permanently alter the phase angle φ (Figure 5.2, the primary measurement variable. Notably, despite structural changes in the polymer due to rapid decompression and oxygen release (Figures 5.3 and 5.4), no significant impact on the phase angle is observed.

Calibration under pressure conditions demonstrates that the phase angle accurately reflects an absolute oxygen concentration, irrespective of pressure (Figure 5.5). Nonetheless, the sensor's resolution declines with increasing oxygen concentration (Figure 5.6). Beyond a phase angle of 5.3°, corresponding to approximately 227 mg l^{-1}, distinguishing between absolute oxygen concentrations ρ_{O_2} accurately becomes difficult. Past this point, the mix of diminished resolution and measurement variance makes clear differentiation unfeasible.

The implemented PreSens firmware effectively replicates the absolute oxygen concentration up to a oxygen concentration of 227 mg l^{-1}. Yet, for high-precision oxygen measurements, calibration tailored to specific measuring conditions is essential (Figure 5.7). Minor shifts in the phase angle at elevated oxygen concentrations lead to notable discrepancies in the measured values, underscoring the need for precise calibration.

5.2 Characterisation of the Mass Transfer under Pressure

To understand the behaviour of glucose oxidase and further improve the process, oxygen availability and its mass transfer within the reactor setup are critically important. Analysing the bubble regime is essential for spotting potential constraints and establishing an optimal range of operation for the aeration unit. The mass transfer process is characterized through the optical measurement of bubble diameters, which allows for the determination of gas hold-up ε_G and the area available for mass transfer a. Subsequently, the mass transfer coefficient for the aeration unit is measured, employing previously characterized optical oxygen sensors.

5.2.1 Characterisation of the Bubble Regime

Figure 5.8 below presents the bubble regimes observed within a column of 15.8 mm in diameter, under varying superficial gas velocities. This visualization captures the dynamic behaviour of bubbles across different flow rates and pressures, providing insights into the operational characteristics of the aeration unit.

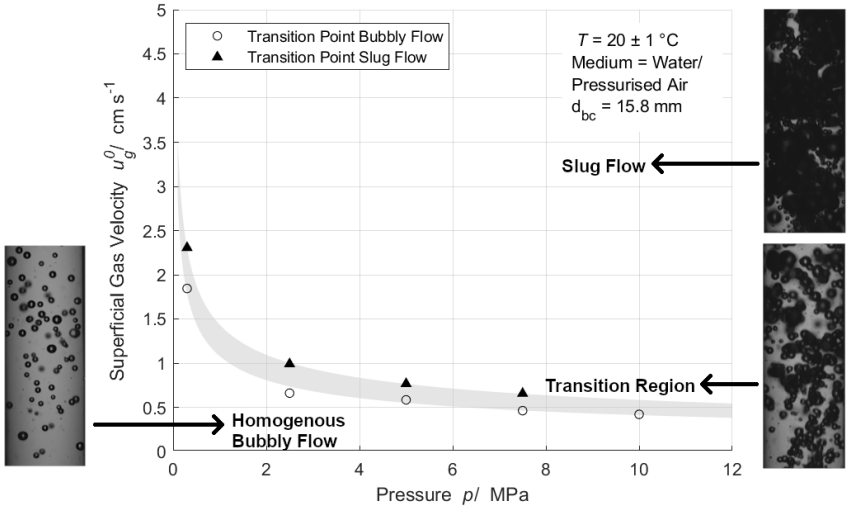

Fig. 5.8 Analysis of the bubble regime across the operational range of the bubble column ($d_c = 15.8$ mm) used in the reactor setup.

As outlined in Section 2.1.1 and depicted in 5.8, the bubble regime in small-scale laboratory bubble columns can be divided into two distinct phases: a homogeneous bubble regime and slug flow. The homogeneous bubble regime is identified by a uniform bubble pattern with a nearly monodisperse bubble size distribution. Conversely, slug flow is defined by bubbles that span the full cross-section of the bubble column. The shift between these regimes is smooth and continuous, marked by a broadening in bubble size distribution due to coalescence.

The observed range of superficial gas velocities u_g^0 between 1.8 and 2.3 cm s^{-1} at 0.3 MPa for the transition between homogeneous bubbly and slug flow is slightly lower than the 3.0 to 4.0 cm s^{-1} observed under atmospheric pressure. Additionally, it's noted that the transition

from homogeneous to heterogeneous bubble regimes occurs at lower superficial gas velocities with increasing pressure, stabilizing at a nearly constant transition range between 0.4 and 0.65 cm s^{-1} around 5.0 MPa.

It is important to note that the determination of the superficial gas velocity u_g^0 accounts for the compressibility of the gas. For this purpose, the standard volumetric flow rate was first converted into a molar flow rate using the ideal gas law (Equation 4.1). Subsequently, the molar flow rate was reconverted into the actual volumetric flow rate under process conditions, again applying the ideal gas law. Finally, the superficial gas velocity was calculated considering the reactor cross-sectional area A_{bc} using Equation 2.9. Without accounting for gas compressibility, it might falsely appear that the transition occurs at higher superficial gas velocities.

In terms of process technology, operating close to the transition boundary would be optimal to achieve a high specific exchange area, along with maximum turbulence and mixing. However, for a stable long-term operation of the aeration unit, the homogeneous regime has proven to be the optimal operating range. Prolonged operation in the transition regime leads to liquid accumulation inside the pressure control valve and resulting in significant fluctuations in pressure regulation. In the slug flow regime, increased gas velocities directly expel liquid through the pressure control valve, destabilizing the reactor setup.

5.2.2 Measurement of the Bubble Size Distribution

A key factor in characterising mass transfer is determining the available surface area for mass transfer. This is achieved by optically determining the bubble size distribution, following the methodology described in Section 4.2.1. To analyse the impact of pressure, an operating point with a constant mass flow rate ($\dot{m}_{air}$) of 12.92 mg s^{-1} at operating pressures of 0.3, 7.5, and 15.0 MPa was selected. This specific operating point effectively illustrates how the bubble size distribution changes with increasing pressure.

The normalized volumetric flow rate of air supplied to the system during the investigation of the bubble size distribution is controlled and regulated using flow controller FC 1 (Figure 3.1). This normalized volumetric flow rate is first converted into a molar flow rate using the ideal gas law (Equation 4.1), which relates the gas volume at standard conditions (273.15 K and 101.3 kPa) to the number of moles. Subsequently, the molar flow rate is converted into a mass flow rate by applying the molar mass of dry air (A_{air}) of 28.96 g/mol. The superficial gas velocity u_g^0 used was determined analogously to the procedure described in

the previous chapter. The starting point of the analysis is Figure 5.9, which shows the bubble size distribution at 0.3 MPa.

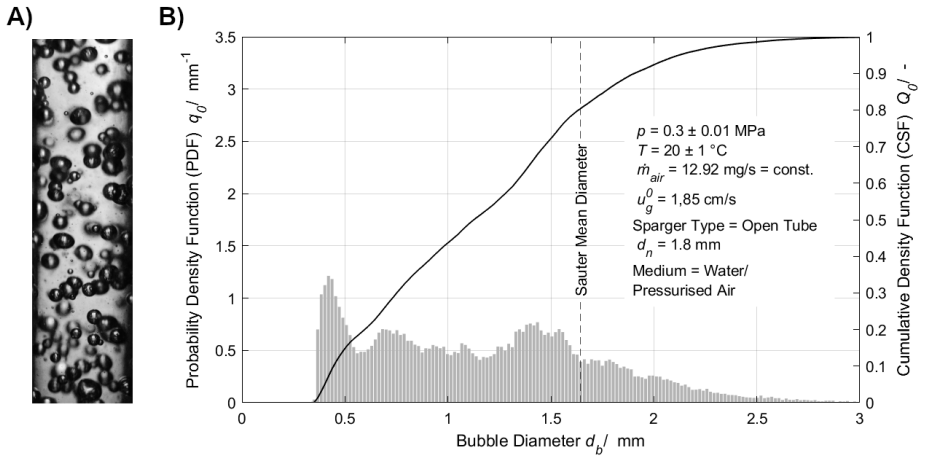

Fig. 5.9 **A)** Image of the aeration unit, and **B)** the corresponding Probability Density Function (q_0) and Cumulative Size Function (Q_0) of the measured bubbles at an operating pressure of 0.3 MPa.

The Probability Density Function (PDF) and the Cumulative Size Function (CSF) of the bubble size distribution show a wide span from 0.3 to approximately 2.5 mm, leading to a Sauter mean diameter d_{32} of 1.64 mm. A significant peak distinguishing the segment between 0.3 and 0.5 mm from the rest of the distribution is observed. At a superficial gas velocity u_g^0 of 1.85 cm s^{-1}, the system operates within the transition region of the flow regime, as indicated in Figure 5.8. This velocity places the system in a range where the flow regime transitions towards slug flow. The prevalent bubble regime promotes extensive coalescence, broadening the size range of the bubbles size distribution. At 7.5 MPa, depicted in Figure 5.10, the bubble size distribution markedly shifts.

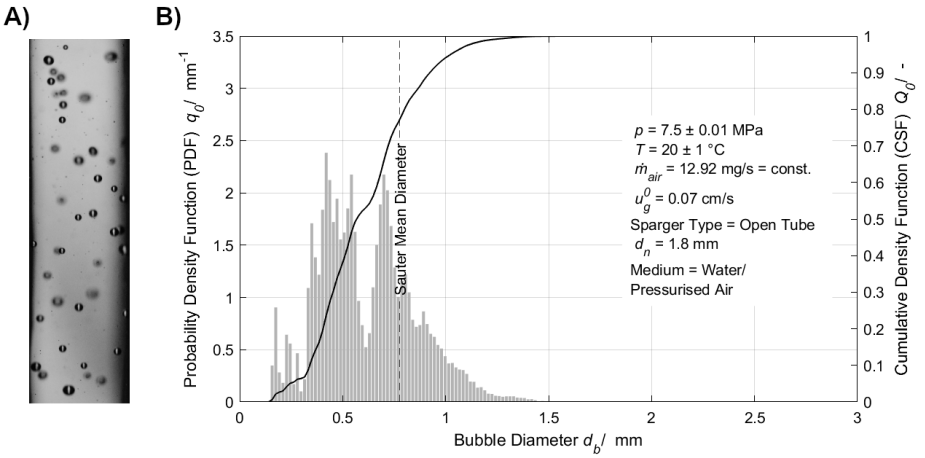

Fig. 5.10 **A)** Image of the aeration unit, and **B)** the corresponding Probability Density Function (q_0) and Cumulative Size Function (Q_0) of the measured bubbles at an operating pressure of 7.5 MPa.

This shift reveals a bimodal distribution between 0.25 and 1.5 mm, demonstrating a decrease in bubble diameters compared to an operating pressure of 0.3 MPa. Consequently, the Sauter diameter d_{32} also decreases to 0.77 mm. When considering the superficial gas velocity u_g^0, it is at 0.07 cm s^{-1}, clearly within the homogeneous bubble regime. This regime is less influenced by bubble coalescence and breakage but rather by the bubble generation at the sparger. Visual observations and the bubble size distribution indicate that bubbles are generated through jet gassing, forming both primary and secondary bubbles shortly above the aerator. The following figure shows the bubble size distribution at 15.0 MPa in Figure 5.11.

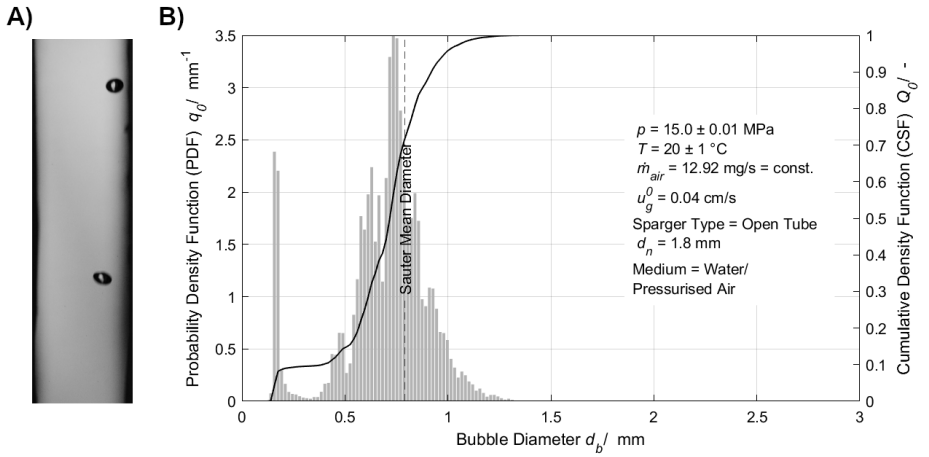

Fig. 5.11 **A)** Image of the aeration unit, and **B)** the corresponding Probability Density Function (q_0) and Cumulative Size Function (Q_0) of the measured bubbles at an operating pressure of 15.0 MPa.

At 15 MPa, the bubble size distribution closely resembles that observed at 7.5 MPa, with sizes ranging from 0.2 to 1.25 mm and a Sauter mean diameter d_{32} of 0.81 mm. The distribution shows a smaller peak around 0.2 mm and a Gaussian distribution peak at 0.79 mm. At this pressure level, with a superficial gas velocity u_g^0 of 0.04 cm s^{-1}, the system remains in the homogeneous bubble regime, signifying that bubble dynamics are mainly influenced by the sparger. Despite a consistent mass flow rate, the increased pressure compresses the gas, enhancing its density, reducing its volume, and decreasing the exit velocity from the capillary. This alteration shifts the aeration mechanism from jet gassing to bubble gassing, leading to a predominantly mono-modal bubble size distribution. The additional peak at 0.25 mm could be attributed to another phenomenon that becomes pronounced at higher pressures. An analysis of force equilibrium outlined in Section 2.1.2 indicates the role of the density difference between the gas and liquid phases in the rising behaviour of gas bubbles. As the pressure increases, the density difference decreases, leading to a reduction in the rising velocity of the gas bubbles. Coupled with vortex formation at the capillary, this dynamic encourages the accumulation of smaller bubbles within the bubble column. The following Figure 5.12 gives an overview of the complete analysis of the bubble size analysis, mapping the relationship between Sauter mean diameter d_{32}, operating pressure p, and the air mass flow $\dot{m}_{air}$ supplied to bubble column.

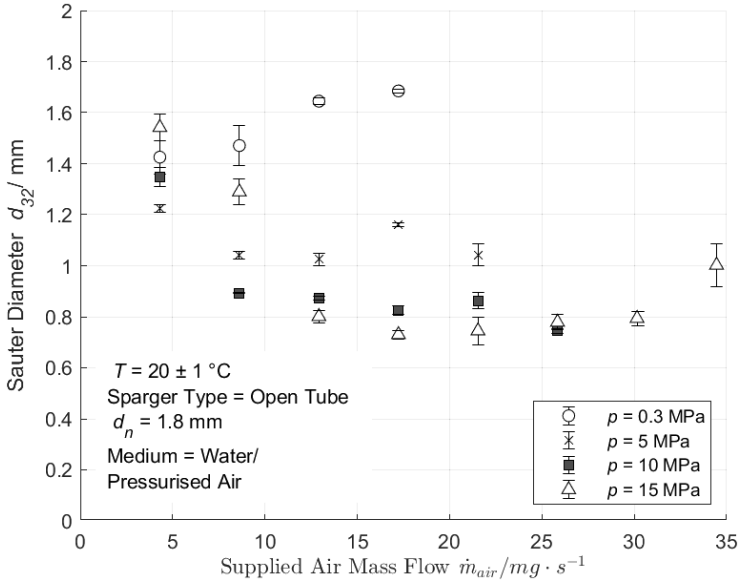

Fig. 5.12 Sauter mean diameter d_{32} as a function of the supplied air mass flow $\dot{m}_{air}$ and the operating pressure p.

From the analysis, several insights emerge regarding the bubble size distribution. Notably, at a constant mass flow rate of 5 mg s^{-1} across all examined pressure levels, the Sauter diameter remains within a confined range of 1.2 to 1.58 mm, due to a homogeneous bubble regime across these conditions. As the mass flow rate increases, this range quickly widens. At 0.3 MPa, a homogeneous bubble regime with jet gassing is observed, an increase in mass flow rate leads to increased coalescence, enlarging the bubble diameter up to 1.7 mm and transitioning towards slug flow. Conversely, at higher pressure levels, the same mass flow rate initially fosters the formation and detachment of individual bubbles. With increasing mass flow rates, both the detachment frequency and bubble diameter reduce, until a further increase in mass flow prompts a shift from bubble gassing to jet gassing.

The analysis indicates that the variation in the Sauter diameter is significantly affected by the prevailing bubble regime and the compressibility of the gas. In the mass flow range of 12 to 22 mg s^{-1} where a similar bubble regime is observed between pressures of 5 and 15.0 MPa the Sauter diameter demonstrates relative stability without significant fluctuations. Importantly, there is a notable trend for the Sauter diameter to diminish with increasing pressure. For example, at 5 MPa, the average Sauter diameter is 1.07 mm, decreases to 0.86

mm, and reaches a minimum of 0.76 mm at 15.0 MPa. The reduction in Sauter diameter is more pronounced up to 5.0 MPa than at higher pressures. This relationship becomes more evident taking gas compression into account, as shown in Figure 5.13, where the ideal gas law (Equation 4.1) is applied to calculate the superficial gas velocity,

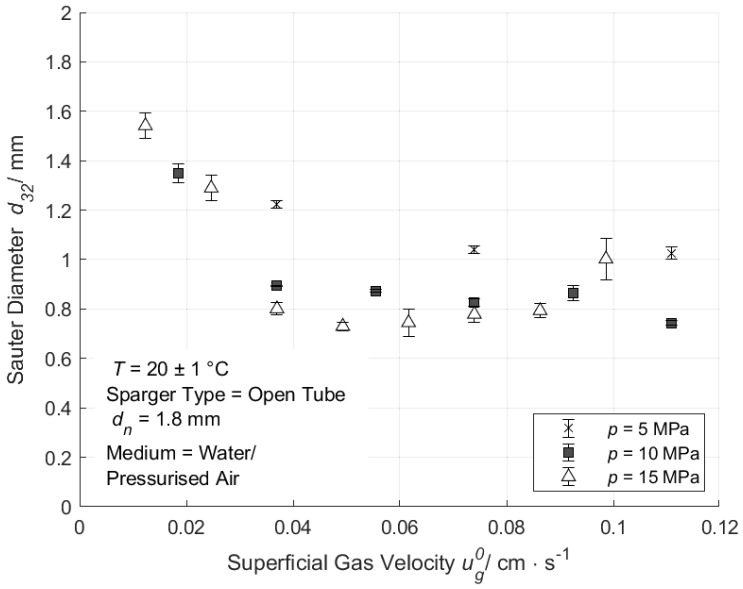

Fig. 5.13 Sauter mean diameter d_{32} as a function of the superficial gas velocity u_g^0 and the operating pressure p.

The Clift diagram serves as a valuable tool for analysing the rise behaviour and shape of bubbles through the use of the dimensionless Morton and Eötvös numbers. This analysis requires the use of pressure-dependent densities and surface tensions for both the gas and liquid phases. While the densities were primarily obtained from reference tables [UDoC23, Gre97], the surface tension values were calculated based on the methodology described by Massoudi [Mas74]. Additionally, the Sauter diameter, determined earlier, is taken into account for computing these key figures. Figure 5.14 displays a portion of the Clift diagram, featuring the specific measurement points included.

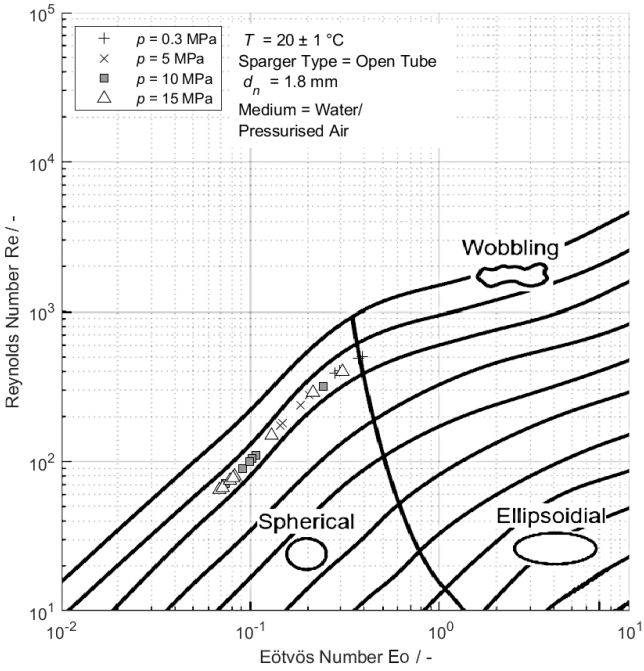

Fig. 5.14 Classification of the measurement points within the Clift diagram.

The data points in the diagram suggest that the bubbles primarily reside within the spherical category. Notably, while the Eötvös number—which factors in the bubble diameter—experiences considerable variations across all pressures, the Morton number remains almost unchanged within the investigated range. Further investigation reveals that the reduction in the Eötvös number with an increase in pressure can be attributed to two main factors: the diminishment of bubble diameter and the decrease in the driving density difference due to gas compression. Examining the data at varying pressures indicates that at 0.3 MPa, bubbles begin tending towards the wobbling regime as the mass flow increases. On the other hand, at higher pressures, there is a clear trend towards spherical bubbles. The identification of bubble regimes based on the Clift diagram is supported by visual evidence from optical images.

Using the Clift diagram, the associated Reynolds number (Re) can be determined alongside bubble morphology, enabling the calculation of the terminal rising velocity (u_b) of bubbles. To achieve this, the Eötvös number (Eo) is first calculated based on the bubble's

size and fluid properties. This value is then used to extract the corresponding Reynolds number (Re) from the Clift diagram. Finally, by applying the Sauter mean diameter (d_{32}) and the kinematic viscosity (ν) of the liquid, the terminal rising velocity (u_b) is determined using the Reynolds Equation 2.16. For a mass flow rate $\dot{m}_{air}$ of 12.92 mg s^{-1} at a pressure of 0.3 MPa, the terminal rising velocity is calculated to 29.9 cm s^{-1}. This velocity decreases progressively with increasing pressure: it drops to 17.0 cm s^{-1} at 5.0 MPa, further declines to 11.9 cm s^{-1} at 10.0 MPa, and ultimately reaches 9.9 cm s^{-1} at 15.0 MPa. Such a reduction in velocity should lead to a longer residence time of the bubbles within the column, increasing the gas hold-up. The extent and confirmation of this effect will be further analysed in the subsequent section.

5.2.3 Determination of the Gas Hold-Up and Mass Transfer Area

Based on the determined bubble size distribution and the methodology presented in Section 4.2.2, the gas hold-up can be effectively approximated. This approximation is performed using Equation 4.2. Figure 5.15 illustrates the relationship between the gas hold-up ε_g, the supplied gas mass flow $\dot{m}_{air}$ and operating pressure p:

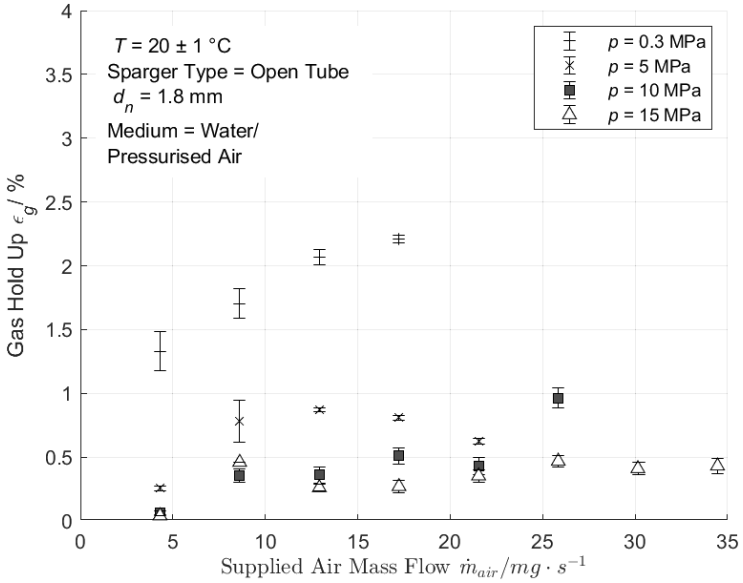

Fig. 5.15 Gas hold-up ε_g as a function of the supplied air mass flow $\dot{m}_{air}$ and the operating pressure p.

The graph shows that the gas hold-up reaches a maximum value of 2.2 %, which is relatively low considering bubble columns than can achieve gas hold-ups of up to 30 % and more. The trend in data generally aligns with the theoretical expectations depicted in Figure 2.4. Specifically, in a homogeneous bubble regime, a nearly linear increase in gas hold-up is observed. However, as it approaches the transition zone, there is a noticeable stagnation or decrease in gas hold-up, especially evident at $p = 5.0$ MPa. Regarding the influence of pressure, it's observed that the gas hold-up decreases, which can be directly linked to the bubble diameter. The reduction in gas hold-up up to $p = 5.0$ MPa is more pronounced than at higher pressures. This effect is primarily due to the reduction in volume caused by gas compression. Consequently, the next Figure, 5.16, illustrates the gas hold-up ε_g as a function of pressure p and superficial gas velocity u_g^0, take compressibility into account.

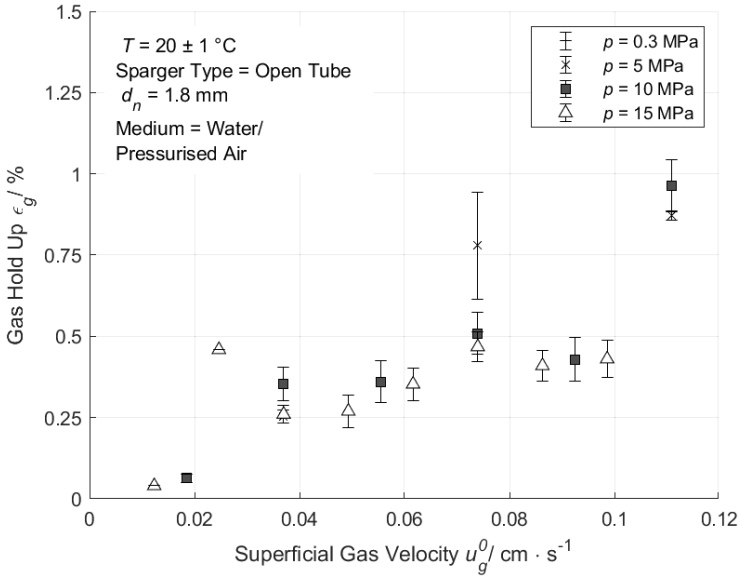

Fig. 5.16 Gas hold-up ε_g as a function of the superficial gas velocity u_g^0 and the operating pressure p.

Direct examination of the graph reinforces the observation of a linear increase in gas hold-up within the homogeneous bubble regime. Additionally, it is noticeable that pressure does not significantly alter the trend of the curves, aligning with the results from literature [Lin98]. Despite the reduction in rising velocities with increasing pressure, the limited height of the bubble column, which is only $h_{bc} = 19.4$ cm, may not contribute to an increase in gas hold-up either. This restricted height results in only a brief contact time from bubble

formation to their emergence at the liquid surface, insufficient to achieve a notable difference in gas hold-up.

As demonstrated by Equation 2.8, the gas hold-up ε and the Sauter diameter d_{32} is not directly considered in the calculation of the mass flow rate between the liquid and gaseous phases. Rather, these parameters influence the specific mass transfer area a. For spherical bubbles, this area can be calculated using Equation 2.7. The following figure displays how the specific mass transfer area a varies with the supplied air mass flow $\dot{m}_{air}$ and operating pressure p.

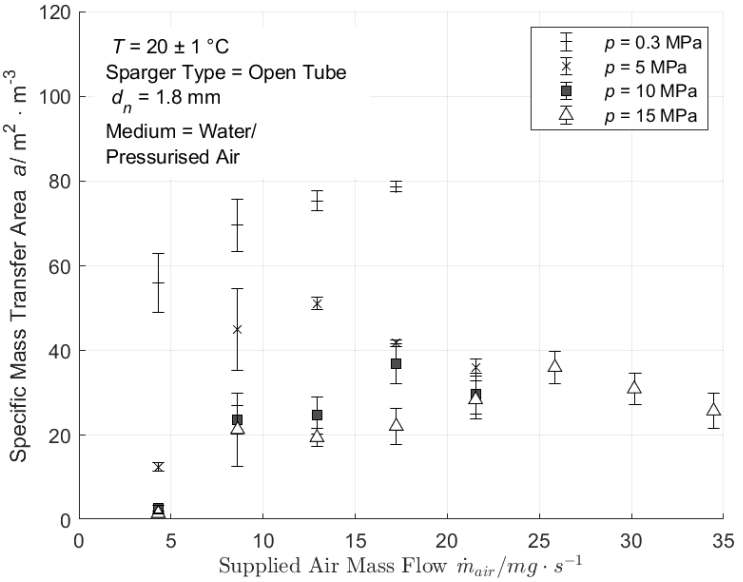

Fig. 5.17 Specific mass transfer area a as a function of the supplied air mass flow $\dot{m}_{air}$ and the operating pressure p.

The graph shows that the highest specific mass transfer area a achieved ranges from 55 to 80 $m^2\ m^{-3}$ at a pressure level of 0.3 MPa. As pressure increases, the specific transfer area gradually diminishes. The gas hold-up ε_g is a critical factor for the mass transfer area. Despite achieving a smaller bubble diameter at higher pressures, this does not fully compensate for the volume reduction and the consequent decrease in gas hold-up. Therefore, Figure 5.18 provides an alternative view of the specific mass transfer area by accounting for the actual volume supplied, represented through the superficial gas velocity.

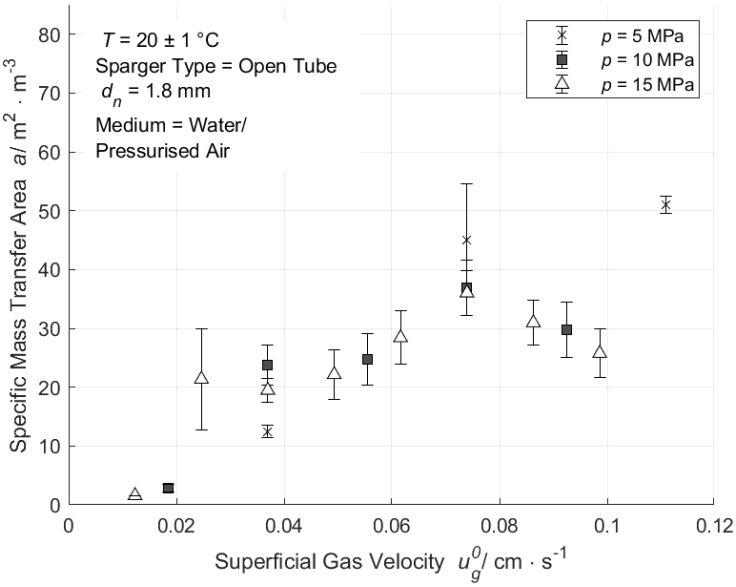

Fig. 5.18 Specific mass transfer area a s a function of superficial gas velocity u_g^0 and the Operating Pressure p.

The figure distinctly illustrates that the specific exchange area follows an almost linear correlation up to a superficial gas velocity of 0.075 cm^{-1}, unaffected by the operating pressure. Yet, past this velocity, a divergence from the trend observed at 5.0 MPa becomes apparent. While the interfacial area decreases at 10.0 and 15.0 MPa, it experiences a notable increase at 5.0 MPa. This phenomenon may be attributed to the dynamics of bubble formation. As delineated in Chapter 2.1.2, the formation of bubbles is influenced by not just the volume flow supplied but also by various material properties that are dependent on pressure, such as surface tension σ and viscosity η. According to Schmelzer [Sch05], viscosity exhibits only a minimal change from 1 to 0.99 mPa s across the pressure range considered. Conversely, surface tension demonstrates a significant reduction, from 71.7 to 63.5 mN m^{-1}, following an exponential trend within the same pressure range, as reported by Massoudi [Mas74].

5.2.4 Measurement of the Volumetric Mass Transfer Coefficient

In addition to the optical examination of the bubble regime and bubble size distribution, the optical oxygen sensors discussed in Section 5.1 were utilised for characterising the aeration unit. The mass transfer coefficient $k_l a$ was determined using the dynamic method detailed in Section 4.2.3. This method involves plotting the logarithm of the concentration difference over time, where the slope of the resulting line, representing $k_l a$, is calculated through linear regression. The evaluation of $k_l a$ posed several challenges, notably the oxygen solubility limits. Oxygen solubility, calculated according to Formula 2.25, reaches 234.23 mg l^{-1} at 2.5 MPa and 20°C, surpassing the sensor's maximum resolution limit of 227 mg l^{-1}. Thus, attempts to analyse solubility levels beyond this threshold do not provide further insights. When plotting the logarithmic concentration difference up to 227 mg l^{-1} at 2.5 MPa, as depicted in Figure 5.19, additional complications emerge.

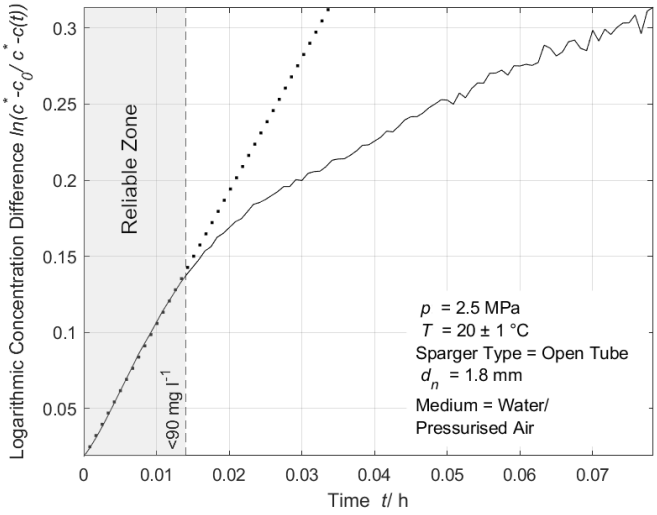

Fig. 5.19 Plot of logarithmic concentration difference over aeration duration for determining the volume-specific mass transfer coefficient $k_l a$ at 2.5 MPa.

Although a linear trend is anticipated, only a portion of the data displays a linear increase yet this range narrows as pressure p rises. Upon detailed analysis, the transition from a linear to a limited growth curve, commonly associated with saturation effects, is observed within an absolute dissolved oxygen concentration range of 90 to 100 mg l^{-1}. This change in curve behaviour may be linked to the performance characteristics of the optical oxygen sensor,

as suggested by Figure 5.6. For the analysis, only the linear section (Reliable Zone) of the trend is considered for evaluation. Additionally, the evaluation is limited to pressures up to 7.5 MPa. Beyond this pressure, the number of measurement points that fall within the range up to 90 mg l^{-1} diminishes, rendering a precise assessment of the mass transfer coefficient, $k_l a$, challenging. Figure 5.20 below illustrates the volume specific transfer coefficients $k_l a$ as a function of the supplied air mass flow $\dot{m}_{air}$ and operating pressure p.

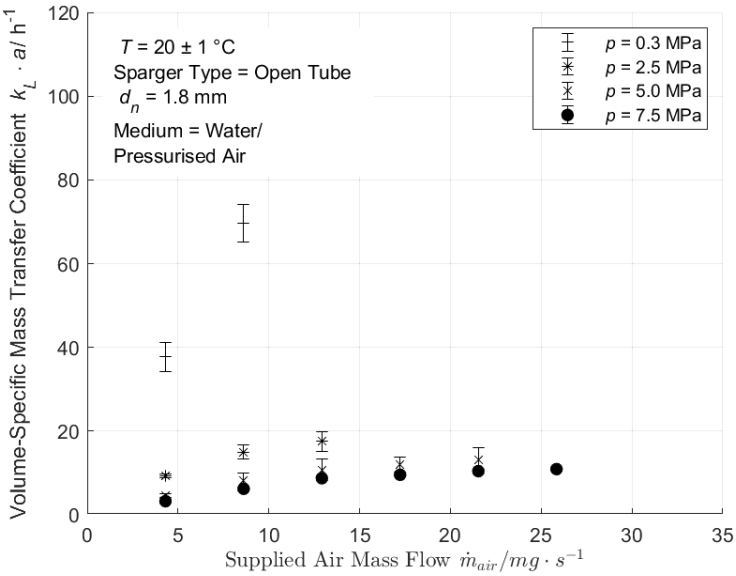

Fig. 5.20 volume-specific mass transfer coefficient $k_l a$ as a function of the supplied air mass flow $\dot{m}_{air}$ and the operating pressure p.

The graph clearly demonstrates a plausible behaviour of the mass transfer coefficient within the aeration unit, aligning with observations from the study of the volume specific surface area. The data consistently shows that the volumetric mass transfer coefficient $k_l a$ tends to increase alongside the mass flow. Notably, the maximum $k_l a$ value of 69 h^{-1} occurs at a pressure of 0.3 MPa diminishes as pressure elevates. This trend has been previously linked to the compressibility of the gas phase. Therefore, examining $k_l a$ against the superficial gas velocity u_g^0 is of special interest. This relationship is depicted in Figure 5.21.

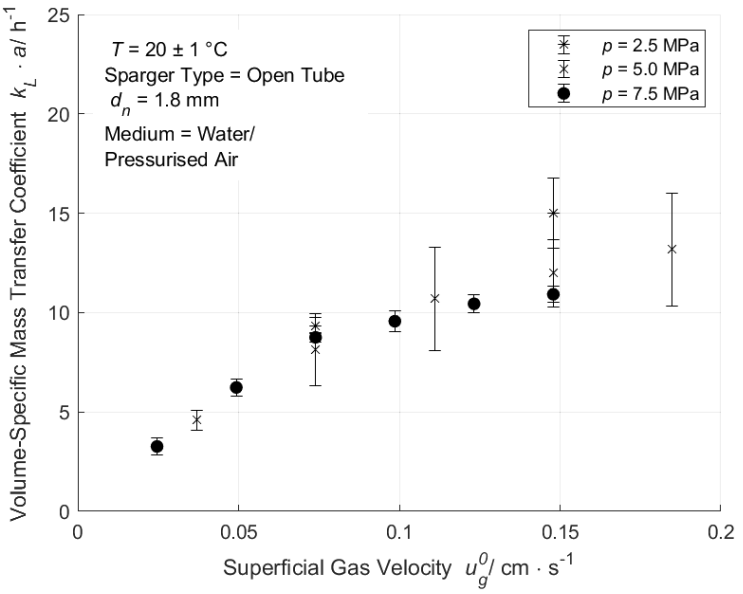

Fig. 5.21 Volume-specific mass transfer coefficient $k_l a$ as a function of the compression-corrected superficial gas velocity u_g^0 and the operating pressure p.

The graph shows that, when accounting for the compressibility of the gas, the volumetric mass transfer coefficient $k_l a$ follows a consistent trend relative to the superficial gas velocity across the examined range of the homogeneous bubble regime. This trend remains valid across all pressure levels. At lower pressures, the correlation with the available volume specific surface area a, as depicted in Figure 5.18, is distinctly observable. However, one area of interest that remains unexplored due to the limitations of optical measurement techniques is the behaviour of $k_l a$ at pressures beyond 7.5 MPa. Particularly, beyond a superficial gas velocity of 0.08 cm s^{-1}, a noticeable decrease in the volume specific surface area a has been observed.

5.2.5 Assessment of the High-Pressure Aeration Unit

After investigating various facets of mass transport, the final step involves an overall assessment of the mass transfer performance in the aeration unit and identifying core parameters. A significant consideration in this context is the compressibility of the gases under pressure. Although the liquid phase is largely incompressible, the gas phase undergoes considerable compression. Introducing a constant mass flow at the gas inlet precipitates a volume reduction, which consequently leads to a diminished volume specific surface area (Figure 5.17) and, by extension, a reduced mass transfer rate (Figure 5.18). This finding underscores the necessity of maintaining a constant volumetric flow to ensure a comparable bubble regime, thereby spotlighting a constraint within the existing aeration setup. Specifically, the research reveals that an optimal operation point, marked by an adequate volumetric mass transfer coefficient $k_l a$, is achieved at $p = 0.3$ MPa with a mass flow of $m_{air} = 13$ mg s^{-1}. To replicate a comparable volumetric flow at $p = 15.0$ MPa, about $m_{air} = 646$ mg s^{-1} would be required.

During characterisation, it was also demonstrated that increasing pressure leads to a reduction in bubble diameter, extending beyond the influence of compressibility alone. This finding aligns with observations reported in similar studies in the literature [Kri91, Rei94]. Moreover, consistent with the literature is the observation that the influence on gas hold-up is minimal within the homogeneous bubble regime [Leo19]. While a decrease in rising velocity with increasing pressure is expected, potentially leading to an increase in gas hold-up, this effect could not be observed significantly. This may be due to the limited height of the employed bubble column. Although some effects were quantified that could potentially enhance mass transport, it appears that these do not significantly improve the overall volume-specific mass transfer coefficient in a laboratory-scale aeration unit.

5.3 Validation of the Reactor Concept with Glucose Oxidase

In the validation phase, the task is to integrate the findings from previous sections and assess their interplay within the reactor system. For this purpose, glucose oxidase in its immobilized form as discussed in section 4.3, is introduced into the high-pressure reactor. Given its rapid reaction rate and the limited oxygen saturation concentration in the substrate at atmospheric pressure, glucose oxidase is prone to mass transfer limitations. Thus, the batch experiments aim to elevate oxygen concentration in the aqueous substrate solution,

surpassing these limitations. The following key points will be addressed in the context of the batch experiments:

- Investigation into how pressure conditions affect the fundamental reactivity of glucose oxidase.
- Employing optical oxygen sensors for real-time monitoring of the reaction's progression under varying pressure conditions.
- Balancing the oxygen mass flows using the data from the optical oxygen sensors.
- Examination of the relationship between increased dissolved oxygen concentration and glucose oxidase activity.
- Assessing the performance and efficiency of the aeration unit.

5.3.1 Evaluation of the Oxygen Measurement Data

In this section, we analyze and present data gathered from oxygen sensors during experiments involving glucose. Figure 5.22 showcases the time-dependent variation of oxygen concentration at both the inlet and outlet of the reactor, operating at a pressure of $p = 0.3$ MPa.

At the onset of aeration ($t = 0$), a noticeable rise in the oxygen concentration is observed at the reactor's inlet. Under conditions without oxygen consumption, it would be expected, that the oxygen concentration at the outlet would follow a similar pattern as the inlet, with a slight delay due to the reactor's hydrodynamic residence time. Ideally, after several passes through the reactor system, the liquid phase would reach oxygen saturation concentration around 22.2 mg l^{-1}. However, the observed behaviour at the bioreactor outlet deviates from this expectation. Following a start period, oxygen concentrations at both the inlet $\rho_{O2,in,stat}$ and the outlet stabilize, maintaining consistent levels from minute 10 to approximately minute 200. The inlet concentration stabilizes at 12.7 mg l^{-1}, while the outlet concentration drops to 0 mg l^{-1}, indicating complete oxygen depletion within the bioreactor. This indicates a complete depletion of oxygen within the bioreactor. From time t_d onwards, a significant increase in oxygen concentration can be observed. Starting from time t_d, there is a marked rise in oxygen concentration, with both inlet and outlet concentrations increasing and slowly aligning. This pattern suggests a reduction of the oxygen consumption within the bioreactor. Figure 5.23 further illustrates the behaviour of inlet and outlet oxygen concentrations at an operating pressure of 10.0 MPa.

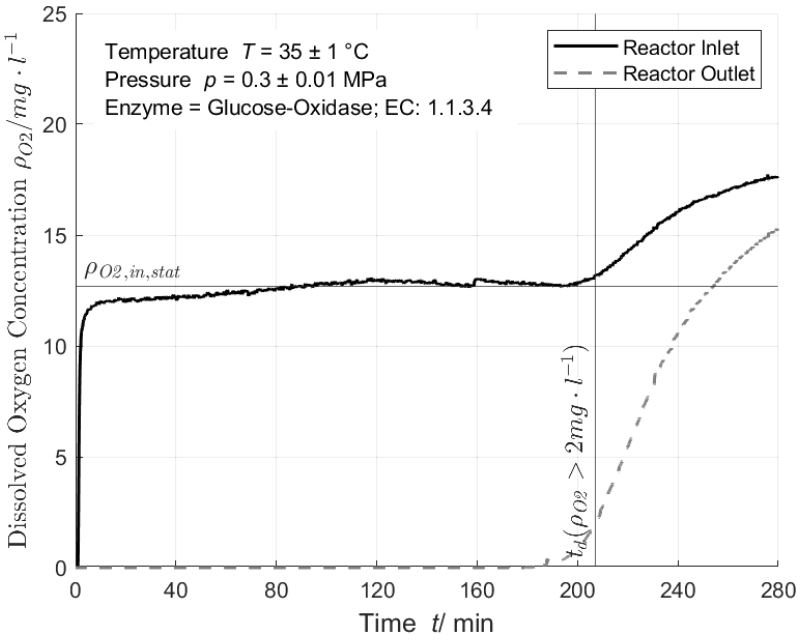

Fig. 5.22 Time course of oxygen concentration c_{O_2} at the Inlet and Outlet of the Bioreactor at $p = 0.3$ MPa. Reaction conditions: T = 35 °C, filling volume: 170 ml, 100 mM D-glucose substrate in sodium acetate buffer (100 mM, pH 5.4), enzyme loading of glucose oxidase: 2.9 $m_{gE}/g_{carrier}$, $\dot{V}_l = 80$ ml min^{-1}, $\dot{m}_{air} = 6.46$ mg s^{-1}.

A comparison of the experiments conducted at pressures of 0.3 MPa and 10.0 MPa reveals similar patterns. In both cases, there is an initial adjustment period of 10 to 15 minutes, after which a steady state is achieved. As observed at 0.3 MPa, the outlet oxygen concentration at 10.0 MPa also approaches nearly 0 mg l^{-1}, indicating complete oxygen consumption within the bioreactor. The steady-state inlet oxygen concentration $\rho_{O2,in,stat}$ at 10.0 MPa is approximately 30.75 mg l^{-1}, reflecting a tendency for this value to increase with pressure. This does not fully exploit the potential for higher saturation concentrations. For example, at 0.3 MPa, the concentration of 12.7 mg l^{-1} achieves 57.2 % of relative saturation. In contrast, at 10.0 MPa, the system has the potential to achieve saturation levels up to 740.2 mg l^{-1}. However, with an inlet concentration of 30.8 mg l^{-1} at this higher pressure, the relative saturation is only about 4.15 %, which is significantly below the maximum saturation potential. This discrepancy arises from the mass transfer performance of the aeration unit in steady-state operation (Section 5.2.5).

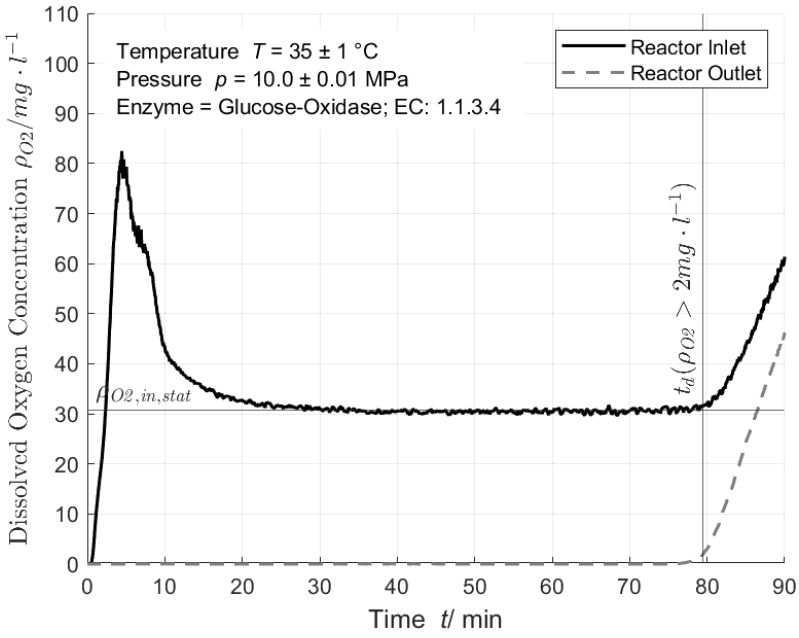

Fig. 5.23 Time course of oxygen concentration at the inlet and outlet of the bioreactor at 10.0 MPa. Reaction conditions: T = 35 °C, filling volume: 170 ml, 100 mM D-glucose substrate in sodium acetate buffer (100 mM, pH 5.4), enzyme loading of glucose oxidase: 2.9 mg g^{-1}, $\dot{V}_l = 80$ ml min^{-1}, $\dot{m}_{air} = 6.46$ mg s^{-1}.

Additionally, the time point t_d at which the outlet concentration begins to rise sharply is noteworthy. At 0.3 MPa, this point is set at around 207 minutes, but at 10.0 MPa, it's significantly reduced to about 79.5 minutes. This quicker shift and the increase in steady-state oxygen concentration both show a clear correlation with rising operating pressures. The upcoming Figure 5.24 visually illustrates the relationship between the steady-state oxygen concentration $\rho_{O2,in,stat}$, supplied to the bioreactor and averaged over the reaction time, and the time point t_d under varying pressure conditions.

The graph distinctly illustrates that the moment t_d —when a notable increase in oxygen concentration is observed— is linearly associated with the average oxygen concentration supplied at the bioreactor inlet. This relationship indicates that as oxygen concentration at the inlet rises, the time until t_d shortens. Such a trend implies that enhancing oxygen concentration could lead to process intensification within the bioreactor, a hypothesis that will be further explored and confirmed in the subsequent chapter through analysis of collected

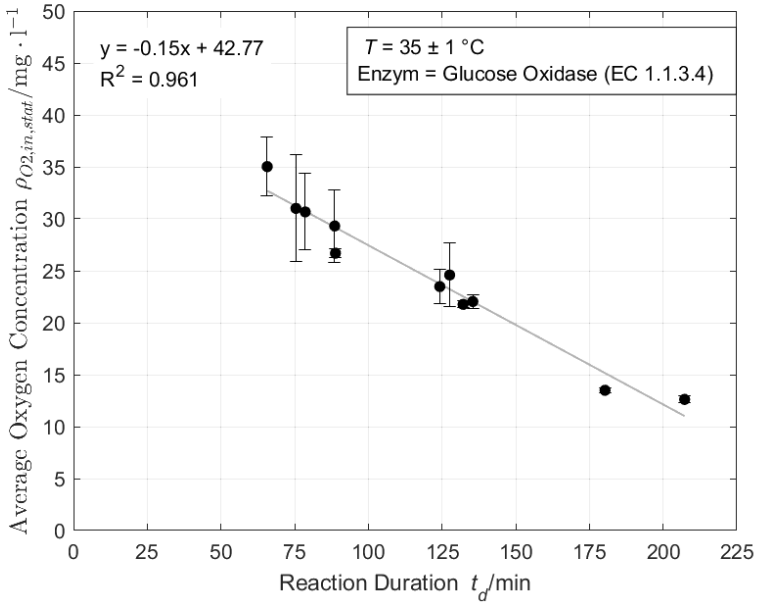

Fig. 5.24 Dependence of duration of the reaction t_d on the average oxygen concentration supplied $\rho_{O2,in,stat}$ to the bioreactor. Reaction conditions: T = 35 °C, filling volume: 170 ml, 100 mM D-glucose substrate in sodium acetate buffer (100 mM, pH 5.4), enzyme loading of glucose oxidase: 2.9 mg g^{-1}, $\dot{V}_l = 80$ ml min^{-1}, $\dot{m}_{air} = 6.46$ mg s^{-1}.

samples and glucose conversion.

Based on Section 4.3.2, the recorded oxygen concentrations were used in conjunction with Equations 4.3 to 4.9 to calculate the individual mass flows: the oxygen mass flow entering the setup ($\dot{m}_{g,bc,in}$), transferred into the liquid phase ($\dot{m}_{bc,trans}$), and consumed by the enzyme ($\dot{m}_{br,trans}$). Additionally, the total oxygen mass supplied (m_{supp}) and converted (m_{conv}) during the experiment were determined. Table 5.2 summarizes these mass flows as well as the resulting oxygen efficiency for experiments conducted at 0.3 MPa and 10.0 MPa.

Table 5.2 Tabular listing of determined mass flows in steady state, total supplied and consumed oxygen masses, and oxygen utilization efficiency during experimentation.

Operating Pressure p/ MPa	**0.3**	**10**	**Unit**
supplied oxygen mass flow $\dot{m}_{g,bc,in}$	1.357	1.357	$mg \cdot s^{-1}$
transferred oxygen mass flow $\dot{m}_{bc,trans}$	16.8	40.9	$\mu g \cdot s^{-1}$
converted oxygen mass flow $\dot{m}_{br,trans}$	18.8	43.6	$\mu g \cdot s^{-1}$
total oxygen mass supplied m_{supp}	22.77	7.65	g
total oxygen mass converted m_{conv}	0.240	0.235	g
Degree of oxygen utilisation η_{O_2}	1.05	3.07	%

A comparison of these data points includes some interesting aspects. The oxygen fully utilised in the bioreactor ($\dot{m}_{br,trans}$) corresponds to all the oxygen dissolved in the liquid phase ($\dot{m}_{bc,trans}$), with instances where the amount of oxygen converted within the bioreactor slightly exceeds the mass of oxygen transferred within the bubble column. This anomaly could result from two factors: potential measurement signal fluctuations due to the sensor spot variability or the decomposition of hydrogen peroxide (Figure 3.6). Contrary to initial mass balance assumptions, the presence of catalase in the aqueous phase allows for hydrogen peroxide decomposition en route from the gas supply unit to the bioreactor, potentially increasing the oxygen concentration.

At the conclusion of the experiment, the enzyme in bioreactor utilised an oxygen mass (m_{conv}) of approximately 0.240 g, a figure closely aligned with the 0.235 g used at $p =$ 10.0 MPa. Remarkably, the mass flow transferred (m_{supp}) between the gaseous and liquid phases within the aeration unit at 10.0 MPa is 2.4 times higher than at 0.3 MPa, measuring 40.9 µg s^{-1}. This results in a reduced time to dissolve 0.235 g of oxygen, and with a total oxygen supply of 7.65 g, the utilization efficiency η_{O_2} of the introduced oxygen improves from 1 % to 3 % significantly.

A far more interesting aspect is the exploration of the extent to which these numbers can be optimized. A key consideration in optimizing process parameters is the impact of insights gained from the characterisation of mass transfer on overall performance. A pivotal factor is the maximum oxygen solubility observed. At 0.3 MPa, the system reaches a relative saturation of 57.2 % a.s, indicating a high degree of dissolved oxygen. As the mass transfer is driven by the concentration gradient between the liquid bulk phase and the saturation

concentration, achieving full saturation of the aqueous phase may not be the most effective approach. Moreover, operating near the liquid phase's saturation limit poses a risk of oxygen outgassing due to pressure drops, such as those that might occur in the pump or in the packed bed of the bioreactor. One aspect that can be considered for optimization in relation to maximum saturation is increasing the partial pressure of oxygen in the supplied air or using pure oxygen. This approach can reduce the overall pressure in the system while still achieving high saturation levels. However, this consideration must include the increased effort related to safety measures.

Another aspect to consider is the specific surface area for mass transfer. Figure 5.17 shows that, at a constant mass flow, the surface area for mass transfer decreases with increasing pressure. For the case examined, with an total air flow of $\dot{m}_{air} = 6.461$ mg s^{-1}, a mass transfer area of around $a = 60$ m^2 m^{-3} is achieved at 0.3 MPa. This figure drops to approximately $a = 12$ m^2 m^{-3} at 10.0 MPa. Although the mass transfer area is significantly reduced at higher pressures, the aeration unit can still achieve a better mass transfer performance due to the enhanced concentration gradient driving the process. Therefore, future work should focus on identifying an optimal operation point based on operating pressure—which influences maximum saturation—and the volumetric inlet flow of the bubble column, which correlates with the volume-specific mass transfer coefficient. This balance is crucial to avoid limited glucose conversion in the bioreactor due to insufficient dissolved oxygen and to ensure an efficient mass transfer in the bubble column.

5.3.2 Assessment of the Samples taken from the Reactor

After in-depth examination of the oxygen data and the demonstrated oxygen consumption within the bioreactor, attention now turns to validating how these findings correlate with data acquired from offline HPLC analytics. The subsequent Figure 5.25 shows the glucose conversion X_{GL} over time at various pressure levels under study.

The figure indicates that the conversion rate increases with reaction duration across all pressures, thus confirming the hypothesis that the enzyme is active. Initially, the reaction shows a linear segment where the reaction rate remains constant. This is followed by a phase where the reaction rate diminishes until it finally halts. The data distinctly show that supplementary oxygen supply accelerate the reaction across pressure levels. For instance, while a linear progression of the conversion up to approximately 70 % is observed after 270 minutes at 0.3 MPa, this level is reached after just about 120 minutes at 10.0 MPa, and after only 30 minutes at 15.0 MPa. For all pressures, the identified time point t_d precisely indicates

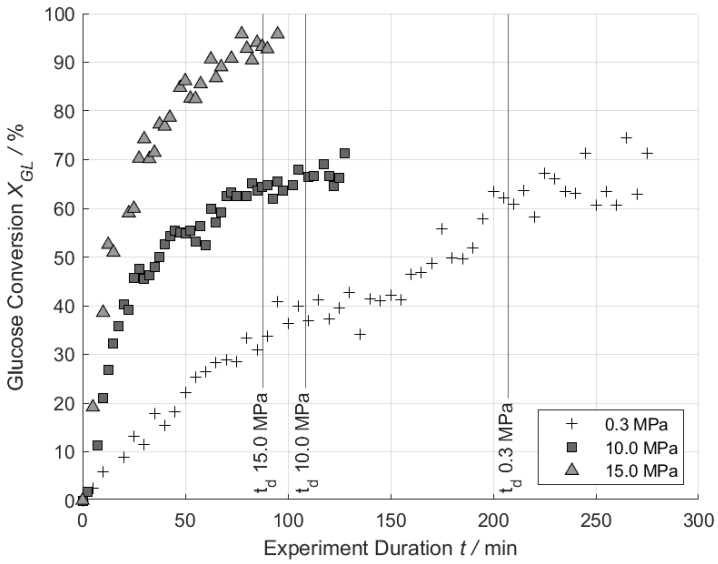

Fig. 5.25 Conversion of glucose X_{GL} over time at 0.3 MPa, 10.0 MPa and 15.0 MPa. Reaction conditions: T = 35 °C, filling volume: 170 ml, 100 mM D-glucose substrate in sodium acetate buffer (100 mM, pH 5.4), enzyme loading of glucose oxidase: 2.9 mg g^{-1}, $\dot{V}_l$ = 80 ml min^{-1}, $\dot{m}_{air} = 6.46$ mg s^{-1}.

when the conversion significantly slows down and nearly reaches a standstill. Further conclusions can be drawn from the conversion data. By considering the stoichiometry, the oxygen demand for the conversion can be determined and compared with the measurement data from the oxygen sensors. For both 0.3 MPa and 10.0 MPa, a conversion rate of 70 % was achieved by the end of the experiment. Since one mole of oxygen is required for the conversion of one mole of D-glucose, the required mass of oxygen can be calculated using the following equation, based on the initial concentration of glucose $c_{GL,0}$, the reactor's fill volume V_R, and the total glucose conversion X_{GL}, as follows:

$$m_{O_2} = c_{Gl,0} \cdot X_{Gl} \cdot M_{O_2} \cdot V_{bc} \tag{5.3}$$

This results in a maximum theoretical oxygen demand of $m_{O_2} = 0.38$ g. By accounting for the oxygen released from hydrogen peroxide decomposition, the theoretical oxygen demand per mole of glucose reduces to 0.5 mole of oxygen, thus lowering the minimal oxygen requirement to $m_{O_2} = 0.19$ g. Comparing this with the data from the oxygen sensors, the observed oxygen conversion at the bioreactor at $m_{conv} = 0.24$ g is within an acceptable range,

trending towards the minimal demand. Pinpointing the exact reason for the discrepancy between the measured oxygen consumption and the minimal theoretical demand is complex. Catalase is added in excess to the substrate solution of each experiment. Determining its degree of deactivation due to circulation and aeration from the existing data proves challenging. Beyond oxygen demand, the data also permits preliminary insights into reaction kinetics. Analysing the conversion data from 0 to 40 % or 40 mM of gluconic acid, as illustrated in Figure 5.26, enables the estimation of the reaction rate.

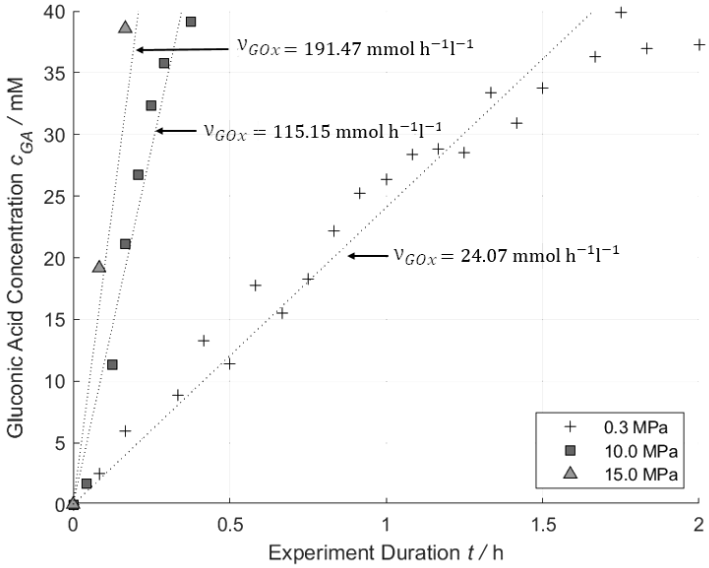

Fig. 5.26 Determination of the reaction rate V_{GOX} in dependence of pressure based on the experimental data. Reaction conditions: T = 35 °C, filling volume: 170 ml, 100 mM D-glucose substrate in sodium acetate buffer (100 mM, pH 5.4), enzyme loading of glucose oxidase: 2.9 mg g^{-1}, $\dot{V}_l = 80$ mL min^{-1}, $\dot{m}_g = 6.46$ mg s^{-1}.

Regression analysis enables the calculation of the initial reaction rate. At $p = 0.3$ MPa, a rate of $\nu_{GOx} = 24.07$ mmol h^{-1} l^{-1} is observed, increasing significantly to 115.15 mmol h^{-1} l^{-1} at 10.0 MPa, and further to 191.47 mmol h^{-1} l^{-1} at 15.0 MPa. This upward trend in the reaction rate of glucose oxidase, prompted by increased oxygen availability, correlates with findings documented by Lindeque [Lin20].

5.3.3 Modeling of the Enzymatic Reaction

After analyzing the oxygen concentration and reaction conversions, kinetic models from the literature can be utilised to contextualize the results and verify the previous findings. These models also help assess the extent to which the potential of increased oxygen availability has been exploited.

The reaction kinetics of the described reaction adheres to the ping-pong bi-bi mechanism as detailed in Section 2.2.1. Initially, the free enzyme binds with glucose and subsequently releases it as oxidized glucono-δ-lactone into the solution. In the following step, the enzyme in its reduced state facilitates a reaction between water and oxygen, producing hydrogen peroxide. This sequence regenerates the enzyme for the following reaction cycle. The Cleland diagram that illustrates this mechanism is shown in Figure 5.27.

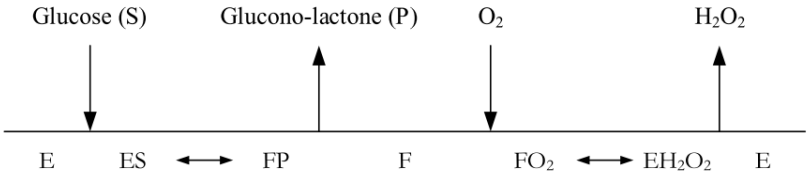

Fig. 5.27 Representation of the Ping-Pong Bi-Bi reaction mechanism of glucose oxidase illustrated in a Cleland diagram.

Based on the reaction mechanism, the reaction rate v_{Gox} can be calculated using the enzyme concentration c_{GOx}, the substrate concentration c_{GL}, and the oxygen concentration c_{O_2}, as described in following equation

$$v_{GOx} = \frac{k_{cat,GOx} \cdot c_{GOx} \cdot c_{GL} \cdot c_{O_2}}{c_{GL} \cdot c_{O_2} + K_{M,O_2} \cdot c_{GL} + K_{M,GL} \cdot c_{O_2}}. \tag{5.4}$$

The affinity constants of glucose oxidase for glucose and oxygen, crucial for Equation 5.4, were identified by Ringborg using a specified pressurised tube-in-tube flow reactor with a reactor volume of $V_R = 155$ µl [Rin17]. These obtain kinetic values are listed in Table 5.3.

Table 5.3 Kinetic parameters for glucose oxidase [Rin17].

Kinetic Parameter	**Value**	**Unit**
Turnover Number GOx/ $k_{cat,GOx}$	17.8 ± 1.39	$\mu mol \cdot min^{-1} \cdot mg^{-1}_{GOx}$
Affinity Coefficient Glucose/ $k_{M,GL}$	75.2 ± 9.38	mM
Affinity Coefficient Oxygen/ k_{M,O_2}	0.51 ± 0.09	mM

Using Equation 5.3 and the parameters provided by Ringborg (Table 5.3), the reaction dynamics are evaluated by taking into account the concentrations of glucose oxidase, glucose, and oxygen. The following graph depicts the calculated reaction rates v_{GO_x} as a function of the glucose oxidase concentration ρ_{GO_x} and oxygen concentration ρ_{O_2}.

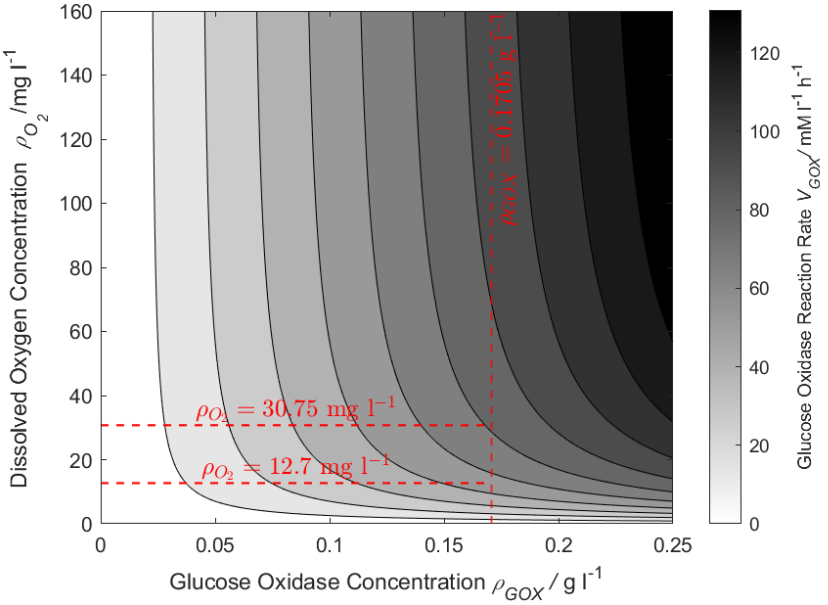

Fig. 5.28 Reaction rate of glucose oxidase (v_{GO_x}) determined through Ping-Pong Bi-Bi multi-Substrate Kinetics at a glucose concentration (c_{GL}) of 100 mM.

In the context of oxygen supply, the generated contour plot offers key insights: Horizontal lines indicate a reaction rate limited by available oxygen, while vertical lines suggest that glucose oxidase activity is the limiting factor.

The results from the previous experiments can also be contextualized using the contour plot. Based on the total weight of the carrier material (10 g), its enzyme loading (2.9 mg enzyme/g carrier), and the total reactor volume (170 ml), the resulting glucose oxidase concentration ρ_{GOx} is 0.1705 g l^{-1}. For oxygen concentrations in the range of atmospheric saturation ($\rho_{O_2,atm} = 8.8$ mg l^{-1}), a horizontal progression of the contour lines can be observed. Consequently, by increasing the oxygen concentration to $\rho_{O_2} = 12.7$ mg l^{-1}, achieved under the experimental conditions at 0.3 MPa, an increase in the reaction rate from $\nu_{GOx} = 50.52$ mmol h^{-1} l^{-1} to $\nu_{GOx} = 59.99$ mmol h^{-1} l^{-1} can be predicted. However, the experimentally determined reaction rate is only $\nu_{GOx} = 24.07$ mmol h^{-1} l^{-1}. This discrepancy can be explained by further examining the work of Lindeque and Ringborg [Lin20, Rin17]. In their studies, reactor types such as the Continuous Stirred Tank Reactor (CSTR) were employed, where glucose is homogeneously distributed within the substrate. This configuration allows for higher enzymatic activity compared to the Packed Bed Reactor (PBR) used in this study.

An interesting aspect arises when considering a further increase in oxygen concentration. At 10 MPa, a steady-state oxygen saturation of $\rho_{O_2} = 30.75$ mg l^{-1} was achieved. According to the model, this results in a reaction rate of $\nu_{GOx} = 79{,}82$ mmol h^{-1} l^{-1} , approaching a range where the contour lines begin to align vertically. This showing an independence of the oxygen concentration to further increase the reaction rate beyond approximately $\nu_{GOx} =$ 100 mmol h^{-1} l^{-1}. In contrast, the experimentally determined reaction rate at this condition was significantly higher, reaching $\nu_{GOx} = 115.15$ mmol h^{-1} l^{-1} at 10 MPa and reaching $\nu_{GOx} = 191.47$ mmol h^{-1} l^{-1} at 15 MPa.

Generally, the experimental results align with the model predictions, indicating that an increase in oxygen concentration indeed enhances the reaction rate. However, the measured values at higher pressures significantly exceed the calculated values. A possible explanation for this discrepancy might be that Ringborg determined the kinetic data only up to $p =$ 0.6 MPa. Consequently, the model may not fully account for pressure effects occurring at pressures up to 15 MPa. This highlights the necessity of re-evaluating the kinetic data for pressures beyond this range, emphasizing the importance of extending kinetic studies to higher pressure conditions for a more comprehensive understanding.

5.4 Assessment of the Reactor Setup

In this concluding section, the aim is to compile and evaluate the results of the studies along with the experiences gained in handling the setup. This encompasses a comprehensive consideration of biotechnological, measurement, and mass transport aspects. Beyond the experiments involving glucose oxidase, the reactor's applicability as a versatile platform for exploring various enzymatic systems is also discussed.

In terms of biotechnological assessment, the investigated setup provided a fundamental proof of principle. The batch experiments conducted in the bioreactor with immobilized glucose oxidase demonstrated enzyme reactivity up to the maximum pressure of 15.0 MPa. Moreover, it was established that mass transfer limitations observed under atmospheric conditions could be mitigated by enhancing dissolved oxygen concentration, leading to process intensification. However, several critical factors for the economical scaling of bioreactor operations remain unexplored. This limitation is partly due to the primary focus on the properties of the bioreactor's inflow and outflow streams, leaving the reactor's internal dynamics a black box when operated under pressure. The activity, stability, and specificity of glucose oxidase have been examined only superficially, despite the possibility that these could be influenced by applying high pressure. Similarly, the potential negative influence of substantially higher oxygen concentrations on the enzyme's activity has not been investigated.

Regarding the aim to establish the reactor as an effective biotechnological testing platform, there's a distinct need for developing a quick and easily adaptable immobilization method for various enzymes, as well as choosing suitable carrier materials and structures. The processes of enzyme immobilization and bioreactor loading were not only time-intensive but also subject to variability and inaccuracies, complicating the conduct of systematic screening experiments.

Within the realm of measurement technology, optical oxygen measurement techniques have been established as reliable online monitoring tools. The investigation demonstrated that the sensors could provide accurate measurements under pressure and resolve oxygen concentrations up to approximately 227 mg l^{-1}. It was also shown that the results from the optical sensors align with those obtained from offline analytics. In addition to optical oxygen sensors, optical pH sensors were successfully integrated into the setup to monitor the pH level of the aqueous phase. Through an integrated control loop, acidification of the medium by the produced gluconic acid could be prevented, maintaining maximum enzyme activity. Regulating the pH value posed a challenge due to the reactor's small volume,

necessitating the use of a relatively high concentration of sodium hydroxide. Alongside the online measurement of oxygen concentration, a controllable HPLC valve with a sampling loop was also incorporated via a bypass. By connecting to the process control system and utilizing a sample carousel, the sampling process could be automated. The arrangement enabled the consistent and frequent collection of high-quality samples from the pressurized environment, demonstrating the system's effectiveness in gathering precise data for analysis.

In the examination of mass transport and hydrodynamics within the setup, the compressibility of the supplied gas emerged as one of the significant challenges. As a result, the supplied volume, the mass transfer area, and consequently, the specific mass transfer coefficient were reduced. In the range where a volume-dependent perspective was possible, it was demonstrated that a reduction in bubble diameter and a decrease in rise velocity with increasing pressure could be achieved. However, due to the low height of the bubble column used, these effects could not be fully exploited. Despite the significantly reduced mass transfer area, an increase in the oxygen concentration in the liquid phase could be achieved due to the driving concentration difference between the bulk and saturation concentrations. Nonetheless, the achieved dissolved oxygen concentration remains significantly below the saturation concentrations. This discrepancy can be attributed to the mass transfer performance of the aeration unit, is not optimized for achieving maximum saturation levels under the pressures investigated. Therefore, a primary focus in the scale-up process is accordingly on optimizing the aeration unit of the reactor concept.

Chapter 6

Conclusion and Concept for a Reactor Scale-Up

In this study, a reactor was successfully designed, manufactured, and erected for aerated high-pressure applications in biotechnology. During the operation of this facility, aspects such as online oxygen measurement technology, mass transfer in the aeration unit under increasing operating pressures, and a reduction of mass transport limitations through enhanced oxygen solubility were examined.

The investigation of the optical measurement technique revealed that oxygen probes based on fluorescence quenching can withstand varying pressure loads and that, even under pressure, the measurements can be clearly attributed to specific oxygen concentrations. It was also shown that with increasing oxygen concentration, the relationship between the measured variable and oxygen concentration is no longer linear, and the resolution decreases. As a result, this method is only applicable up to an absolute oxygen concentration of approximately $\rho_{O_2} = 227\ \mathrm{mg\ l^{-1}}$.

The hydrodynamic characterization covered the distribution of bubble sizes, gas hold-up, volume specific surface area, and the volumetric mass transfer coefficient. This study confirmed literature claims about the reduction in bubble diameter under pressure. An increase in gas hold-up due to reduced ascent velocity could not be confirmed. Possibly due to the given height of the bubble column. It was also demonstrated that the primary improvement in mass transfer within the bubble column used is not due to an increase in exchange area but to a significant increase in the driving concentration gradient due to higher saturation concentrations.

Validation experiments with glucose oxidase demonstrated that the core idea of the reactor concept works. Firstly, the progress of the reaction could be monitored through the integrated oxygen sensors. Secondly a higher oxygen input achieved a significant intensification of the reaction process. However, it was also shown that the full potential of increased maximum oxygen solubility was not fully utilised due to the limited performance of the employed aeration unit.

This study highlights the potential benefits of utilising pressure as a key process parameter and provides the necessary tools with the reactor concept and the investigation of oxygen sensors to easily study the activity, selectivity, and stability of enzymes in the future. This allows the feasibility in an industrial environment to be assessed.

Based on these findings, a scale-up concept utilizing a Jet Loop Reactor was developed and will be implemented and tested in future studies. A key identification point that is also preserved in the scale-up process is the spatial separation of the enzyme from the aeration. The bubble column previously employed should be replaced with a more effective aeration unit that offers a better surface area and a higher residence time for mass transfer in a compact design. An initially considered approach was the Airlift Reactor depicted in Figure 2.1 D. This reactor is characterized by an external loop. The circulation through the external loop is created without mechanical components, due to the density difference with the aerated medium. Another consideration in utilizing this reactor concept was to directly integrate the Packed Bed Reactor into the downcomer. However, design analyses based on insights from Chisti [Chi87] and Guieysse [Gui11] indicated that the essential density difference for effective circulation might be inadequate, primarily due to pressure drops across the packed bed reactor. Consequently, a jet loop reactor was chosen as the central aeration unit. The flow diagram of a reactor concept based on a jet loop reactor is presented in the Figure 6.1.

The concept is distinguished by two circulating liquid loops. The bioreactors are integrated within the inner circulation loop. The inner circulation loop consists of four bioreactors arranged in a star shape around the jet loop reactor. The circulation can be adjusted or completely halted via control and shut-off valves. This allows for a greater operational flexibility, enabling the removal or exchange of bioreactors during operation under pressure. Likewise, different types of enzymes can be introduced to carry out sequential reactions. The bioreactors are dimensioned similarly to the bioreactor used at the laboratory scale. Compared to the laboratory scale, the reactors have, in addition to oxygen measurement at the inlet and outlet, three additional ports to insert optical sensors, thus enabling the resolution of the axial

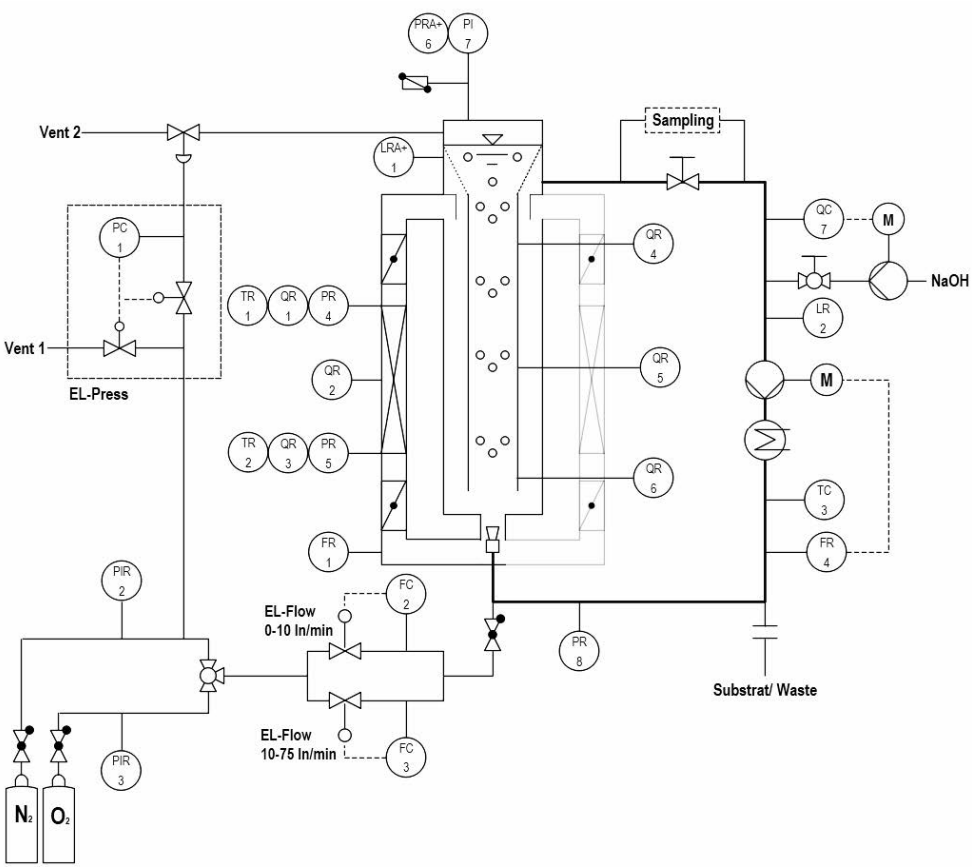

Fig. 6.1 Piping and instrumentation diagram of the scaling concept based on a jet loop reactor

concentration gradient across the reactor.

The outer circulation loop consists of the jet loop reactor, the integrated two-phase nozzle, and a pulse-free gear pump. The scale-up uses a loop reactor designed according to Maly [Mal22], based on Blenke's [Ble71] design rules. In the concept, the liquid flow is drawn from the top of the jet loop reactor, conveyed through an external loop with the pump, and reintroduced at the bottom through a two-phase nozzle. In the outer loop, established peripheral elements such as sampling, pH control, and the main heat exchanger are integrated. In accordance with the design specifications, the reactor accommodates a liquid flow rate ranging from $\dot{V}_l$ 1 to 1.7 l min^{-1} and a specific energy dissipation rate from $\dot{E}/P = 1$ to 4 kW m^{-3}. The gas volume flow is set within $\dot{V}_g$ 0 to 0.3 l min^{-1}. To

counteract the effects of gas compressibility under elevated pressures and to maintain a consistent flow rate across all pressure levels, two mass flow controllers are employed. Based on the P&ID flow diagram and the calculated sizing of the jet loop reactor, a mobile reaction system was designed. A rendered representation of the design is shown in Figure 6.2.

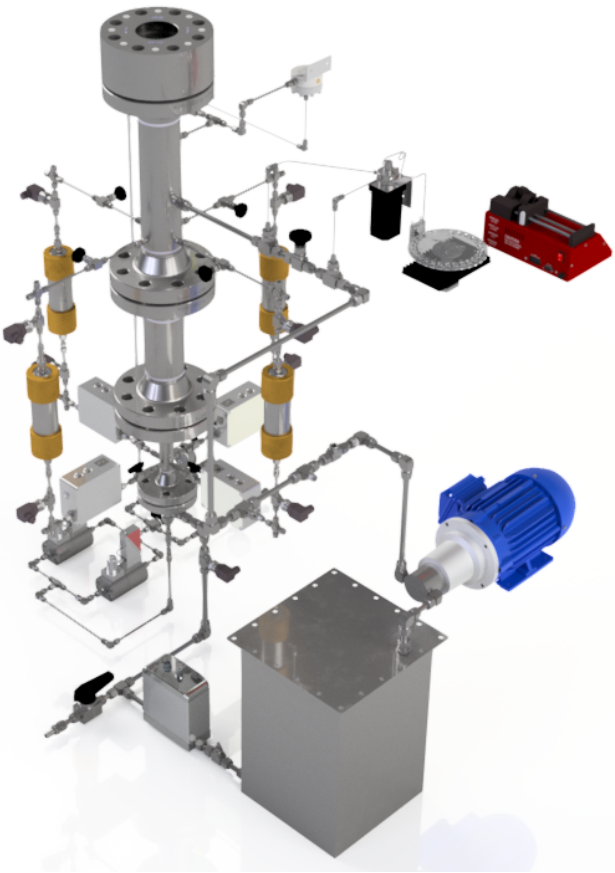

Fig. 6.2 Rendered Representation of the Construction Model of the Upscaled Aerated High-Pressure Reactor.

A key identification point of the reactor concept and in its design is the interconnection of two separate circulation loops without the need for additional pumps. For this purpose, the free jet of the two-phase nozzle is utilized. As depicted in Figure 6.3, the effect is exploited

whereby the jet velocity decreases with increasing distance, and the widening of the jet.

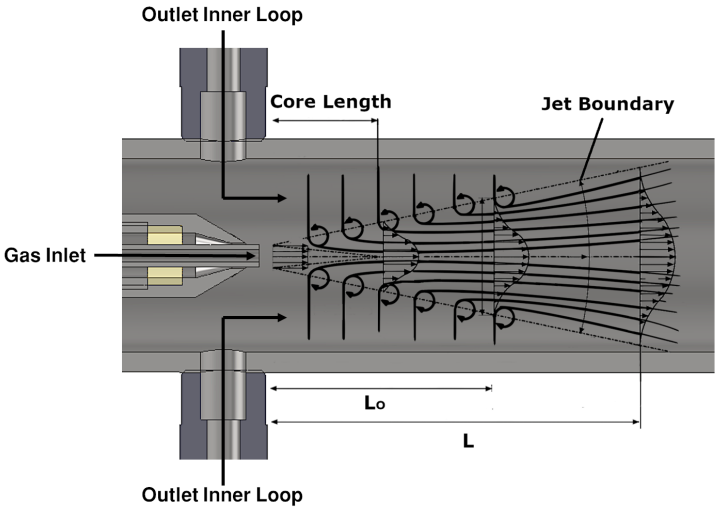

Fig. 6.3 Schematic drawing of the two-phase nozzle of the jet loop reactor including suction from the internal circulation loop via the generated jet.

This expansion is due to the frictional effect at the edge of the jet, which draws in stationary fluid from the surrounding area and moves it within the jet. The overall volume flow rate can thus be proportionally described by the ratio of the core jet length L_0 to the jet length L as follows [Sur17]:

$$\dot{V} = 2 \cdot \dot{V}_0 \cdot \frac{L}{L_0} \tag{6.1}$$

The suction volume flow rate from the inner circulation loop can thus be influenced by two parameters. Firstly, the volume flow rate carried by the external circulation loop can be increased to enhance the exit velocity of the nozzle. Secondly, the positioning of the nozzle in relation to the inlet of the internal circulation can potentially be used to control the suction volume flow rate. During the design phase, the feasibility of axial positioning during operation was assessed. However, due to cost considerations, the nozzle was designed modularly, allowing at least for adjustments to its position outside of active operation.

References

[Alb07] Albani, J.R. *Principles and applications of fluorescence spectroscopy*. Wiley, London, 2007. ISBN 978-1-4051-3891-8.

[Ama03] Amao, Y. *Probes and Polymers for Optical Sensing of Oxygen*. *Microchimica Acta*, 143(1):1–12, 2003. ISSN 0026-3672. doi:10.1007/s00604-003-0037-x.

[Arn18] Arnold, F.H. *Directed Evolution: Bringing New Chemistry to Life*. *Angewandte Chemie (International ed. in English)*, 57(16):4143–4148, 2018. doi:10.1002/anie.201708408.

[Bam94] Bambot, S.B., Holavanahali, R., Lakowicz, J.R., Carter, G.M. and Rao, G. *Phase fluorometric sterilizable optical oxygen sensor*. *Biotechnology and bioengineering*, 43(11):1139–1145, 1994. doi:10.1002/bit.260431119.

[Bat82] Battino, R. *Nitrogen and air*, vol. 10 of *Solubility data series*. Pergamon Press, Oxford, 1982. ISBN 0-08-023922-6.

[Ber10] Berheide, M., Peper, S., Kara, S., Long, W.S., Schenkel, S., Pohl, M., Niemeyer, B. and Liese, A. *Influence of the hydrostatic pressure and pH on the asymmetric 2-hydroxyketone formation catalyzed by Pseudomonas putida benzoylformate decarboxylase and variants thereof*. *Biotechnology and Bioengineering*, 106(1):18–26, 2010. doi:https://doi.org/10.1002/bit.22650.

[Bes18] Besagni, G., Inzoli, F. and Ziegenhein, T. *Two-Phase Bubble Columns: A Comprehensive Review*. *ChemEngineering*, 2(2):13, 2018. ISSN 2305-7084. doi:10.3390/chemengineering2020013.

[Bis17] Bisswanger, H. *Multi–Substrate Reactions*. In H. Bisswanger, editor, *Enzyme kinetics*, pp. 121–143. Wiley-VCH, Weinheim, 2017. ISBN 9783527342518. doi:10.1002/9783527806461.ch5.

[Bit18] Bittig, H.C., Körtzinger, A., Neill, C., van Ooijen, E., Plant, J.N., Hahn, J., Johnson, K.S., Yang, B. and Emerson, S.R. *Oxygen Optode Sensors: Principle, Characterization, Calibration, and Application in the Ocean*. *Frontiers in Marine Science*, 4, 2018. doi:10.3389/fmars.2017.00429.

[Bla88] Blaß, E. *Bildung und Koaleszenz von Blasen und Tropfen*. *Chemie Ingenieur Technik - CIT*, 60(12):935–947, 1988. ISSN 0009-286X. doi:10.1002/cite.330601203.

References

[Ble71] Blenke, H., Bohner, K. and Pfeiffer, W. *Hydrodynamische Berechnung von Schlaufenreaktoren für Einphasensysteme*. *Chemie Ingenieur Technik - CIT*, 43(1-2):10–17, 1971. ISSN 0009-286X. doi:10.1002/cite.330430103.

[Bol19] Bolivar, J.M., Mannsberger, A., Thomsen, M.S., Tekautz, G. and Nidetzky, B. *Process intensification for O2 -dependent enzymatic transformations in continuous single-phase pressurized flow*. *Biotechnology and bioengineering*, 116(3):503–514, 2019. ISSN 00063592. doi:10.1002/bit.26886.

[Bol20] Bolivar, J.M. and López-Gallego, F. *Characterization and evaluation of immobilized enzymes for applications in flow reactors*. *Current Opinion in Green and Sustainable Chemistry*, 25, 2020. ISSN 24522236. doi:10.1016/j.cogsc.2020.04.010.

[Bor12] Bornscheuer, U.T., Huisman, G.W., Kazlauskas, R.J., Lutz, S., Moore, J.C. and Robins, K. *Engineering the third wave of biocatalysis*. *Nature*, 485(7397):185–194, 2012. doi:10.1038/nature11117.

[Bot16] Bothe, M. *Experimental Analysis and Modeling of Industrial Two-Phase Flows in Bubble Column Reactors*. Ph.D. thesis, Technische Universität Hamburg-Harburg, Göttingen, Germany, 2016.

[Bra71] Brauer, H. and Mewes, D. *Stoffaustausch einschliesslich chemischer Reaktionen*. Grundlagen der chemischen Technik. Sauerländer, 1971. ISBN 9783794100088.

[Bra72] Brauer, H. and Mewes, D. *Strömungswiderstand sowie stationärer und instationärer Stoff– und Wärmeübergang an Kugeln*. *Chemie Ingenieur Technik - CIT*, 44(13):865–868, 1972. ISSN 0009-286X. doi:10.1002/cite.330441314.

[Bre13] Brena, B., González-Pombo, P. and Batista-Viera, F. *Immobilization of enzymes: a literature survey*. *Methods in molecular biology (Clifton, N.J.)*, 1051:15–31, 2013. doi:10.1007/978-1-62703-550-7{\textunderscore}2.

[Bri14] Bridgman, P.W. *The Coagulation of albumen by pressure*. *Journal of Biological Chemistry*, 19:511–512, 1914.

[Bri25] Briggs, G.E. and Haldane, J.B. *A Note on the Kinetics of Enzyme Action*. *The Biochemical journal*, 19(2):338–339, 1925. ISSN 0264-6021. doi:10.1042/bj0190338.

[Buc12] Buchholz, K., Kasche, V. and Bornscheuer, U.T. *Biocatalysts and enzyme technology*. Wiley-Blackwell, Weinheim, 2nd, completely rev., and enl. ed (online-ausg.) edn., 2012. ISBN 9783527632923.

[Cen01] Centi, G. *Selective oxidation by heterogeneous catalysis*. Fundamental and Applied Catalysis. Kluwer Academic/Plenum Publishers, New York, 2001. ISBN 0306462656.

[Cha14] Chakraborty, S., Kaushik, N., Rao, P.S. and Mishra, H.N. *High-Pressure Inactivation of Enzymes: A Review on Its Recent Applications on Fruit Purees and Juices*. *Comprehensive reviews in food science and food safety*, 13(4):578–596, 2014. doi:10.1111/1541-4337.12071.

[Cha18] Chapman, M.R., Cosgrove, S.C., Turner, N.J., Kapur, N. and Blacker, A.J. *Highly Productive Oxidative Biocatalysis in Continuous Flow by Enhancing the Aqueous Equilibrium Solubility of Oxygen*. *Angewandte Chemie (International ed. in English)*, 57(33):10535–10539, 2018. doi:10.1002/anie.201803675.

[Che95] Cheftel, J.C. *Review : High-pressure, microbial inactivation and food preservation*. *Food Science and Technology International*, 1(2-3):75–90, 1995. ISSN 1082-0132. doi:10.1177/108201329500100203.

[Chi87] Chisti, M.Y. and Moo-Young, M. *Airlift Reactors: Characteristics, Applications And Design Considerations*. *Chemical Engineering Communications*, 60(1-6):195–242, 1987. ISSN 0098-6445. doi:10.1080/00986448708912017.

[Chi10] Chilekar, V.P., van der Schaaf, J., Kuster, B.F.M., Tinge, J.T. and Schouten, J.C. *Influence of elevated pressure and particle lyophobicity on hydrodynamics and gas–liquid mass transfer in slurry bubble columns*. *AIChE Journal*, 56(3):584–596, 2010. ISSN 00011541. doi:10.1002/aic.11987.

[Chm18] Chmiel, H., Takors, R. and Weuster-Botz, D. *Bioprozesstechnik*. Springer Berlin Heidelberg, Berlin, Heidelberg, 2018. ISBN 978-3-662-54041-1. doi:10.1007/978-3-662-54042-8.

[Cli92] Clift, R., Grace, J.R. and Weber, M.E. *Bubbles, drops, and particles*. Acad. Press, New York, NY, 3. print edn., 1992. ISBN 012176950X.

[Clo17] Clomburg, J.M., Crumbley, A.M. and Gonzalez, R. *Industrial biomanufacturing: The future of chemical production*. *Science (New York, N.Y.)*, 355(6320), 2017. doi:10.1126/science.aag0804.

[Cze17] Czeslik, C., Luong, T.Q. and Winter, R. *Enzymatic activity under pressure*. *MRS Bulletin*, 42(10):738–742, 2017. ISSN 0883-7694. doi:10.1557/mrs.2017.211.

[Dal22] Dalfen, I., Burger, T., Slugovc, C., Borisov, S.M. and Klimant, I. *Materials for optical oxygen sensing under high hydrostatic pressure*. *Sensors and Actuators B: Chemical*, 352:131037, 2022. ISSN 09254005. doi:10.1016/j.snb.2021.131037.

[Dan51] Danckwerts, P.V. *Significance of Liquid-Film Coefficients in Gas Absorption*. *Industrial & Engineering Chemistry*, 43(6):1460–1467, 1951. ISSN 0019-7866. doi:10.1021/ie50498a055.

[Dat13] Datta, S., Christena, L.R. and Rajaram, Y.R.S. *Enzyme immobilization: an overview on techniques and support materials*. *3 Biotech*, 3(1):1–9, 2013. ISSN 2190-572X. doi:10.1007/s13205-012-0071-7.

[Dec85] Deckwer, W.D. and Schumpe, A. *Blasensälen - Erkenntnisstand und Entwicklungstendenzen*. *Chemie Ingenieur Technik*, 57(9):754–767, 1985. ISSN 0009286X. doi:10.1002/cite.330570909.

[Dem95] Demas, J.N., DeGraff, B.A. and Xu, W. *Modeling of Luminescence Quenching-Based Sensors: Comparison of Multisite and Nonlinear Gas Solubility Models*. *Analytical chemistry*, 67(8):1377–1380, 1995. ISSN 0003-2700. doi:10.1021/ac00104a012.

References

[Dem99] Demas, J.N., DeGraff, B.A. and Coleman, P.B. *Oxygen sensors based on luminescence quenching*. *Analytical chemistry*, 71(23):793A–800A, 1999. ISSN 0003-2700. doi:10.1021/ac9908546.

[Den15] Denard, C.A., Ren, H. and Zhao, H. *Improving and repurposing biocatalysts via directed evolution*. *Current opinion in chemical biology*, 25:55–64, 2015. doi:10.1016/j.cbpa.2014.12.036.

[Dew97] Dewes, I. and Schumpe, A. *Gas density effect on mass transfer in the slurry bubble column*. *Chemical Engineering Science*, 52(21-22):4105–4109, 1997. ISSN 00092509. doi:10.1016/S0009-2509(97)00252-2.

[Eis09] Eisenmenger, M.J. and Reyes-De-Corcuera, J.I. *High pressure enhancement of enzymes: A review*. *Enzyme and Microbial Technology*, 45(5):331–347, 2009. ISSN 01410229. doi:10.1016/j.enzmictec.2009.08.001.

[Fan90] Fan, L.S. and Tsuchiya, K. *Bubble wake dynamics in liquids and liquid-solid suspensions*. Butterworth-Heinemann series in chemical engineering. Butterworth-Heinemann, Boston and London, 1990. ISBN 9781483289502.

[Fic55] Fick, A. *Ueber Diffusion*. *Annalen der Physik*, 170(1):59–86, 1855. ISSN 0003-3804. doi:10.1002/andp.18551700105.

[Fra98] Fraher, P. and Clarke, D.W. *Fouling detection and compensation in Clark-type DOx sensors*. *IEEE Transactions on Instrumentation and Measurement*, 47(3):686–691, 1998. ISSN 00189456. doi:10.1109/19.744325.

[GEN10] GENG, M. and DUAN, Z. *Prediction of oxygen solubility in pure water and brines up to high temperatures and pressures*. *Geochimica et Cosmochimica Acta*, 74(19):5631–5640, 2010. ISSN 00167037. doi:10.1016/j.gca.2010.06.034.

[Gre97] Green, D.W. and Maloney, J.O., editors. *Perry's Chemical Engineers' Handbook*. McGraw-Hill Chemical Engineering Series. McGraw-Hill, New York, NY, 7. ed. edn., 1997. ISBN 0-07-049841-5.

[Gui11] Guieysse, B., Quijano, G. and Muñoz, R. *Airlift Bioreactors*. In *Comprehensive Biotechnology*, vol. 47, pp. 199–212. Elsevier, 2011. ISBN 9780080885049. doi:10.1016/B978-0-08-088504-9.00095-7.

[Han20] Hansen, R.B., Agerbaek, M.A., Nielsen, P.M., Rancke-Madsen, A. and Woodley, J.M. *Esterification using a liquid lipase to remove residual free fatty acids in biodiesel*. *Process Biochemistry*, 97:213–221, 2020. ISSN 13595113. doi:10.1016/j.procbio.2020.06.005.

[Hig35] Higbie, R. *The Rate of Absorption of a Pure Gas into a Still Liquid during Short Periods of Exposure*. *Transactions of the AIChE*, 31:365–389, 1935.

[Hik80] Hikita, H., Asai, S., Tanigawa, K., Segawa, K. and Kitao, M. *Gas hold-up in bubble columns*. *The Chemical Engineering Journal*, 20(1):59–67, 1980. ISSN 03009467. doi:10.1016/0300-9467(80)85006-4.

[Int09] International Organization for Standardization. *Water quality; Determination of dissolved oxygen; Iodometric method*, 1983-09.

[Iye08] Iyer, P.V. and Ananthanarayan, L. *Enzyme stability and stabilization—Aqueous and non-aqueous environment*. *Process Biochemistry*, 43(10):1019–1032, 2008. ISSN 13595113. doi:10.1016/j.procbio.2008.06.004.

[Jen87] Jensen, V.J. and Rugh, S. *[33] Industrial-scale production and application of immobilized glucose isomerase*. In *Immobilized Enzymes and Cells, Part C*, vol. 136 of *Methods in Enzymology*, pp. 356–370. Elsevier, 1987. ISBN 9780121820367. doi:10.1016/S0076-6879(87)36035-5.

[Jor02] Jordan, U., Terasaka, K., Kundu, G. and Schumpe, A. *Mass Transfer in High-Pressure Bubble Columns with Organic Liquids*. *Chemical Engineering & Technology*, 25(3):262–265, 2002. ISSN 09307516. doi:10.1002/1521-4125(200203)25:3{\textless}262::AID-CEAT262{\textgreater}3.0.CO;2-C.

[Kan05] Kantarci, N., Borak, F. and Ulgen, K.O. *Bubble column reactors*. *Process Biochemistry*, 40(7):2263–2283, 2005. ISSN 13595113. doi:10.1016/j.procbio.2004.10.004.

[Klu83] Klug, P. *Der Blasenbildungsvorgang bei der Gasverteilung an Lochplatten*. Phd thesis, Technische Universität Clausthal, 1983.

[Kra12] Kraume, M. *Transportvorgänge in der Verfahrenstechnik*. Springer Berlin Heidelberg, Berlin, Heidelberg, 2012. ISBN 978-3-642-25148-1. doi:10.1007/978-3-642-25149-8.

[Kri91] Krishna, R., Wilkinson, P.M. and van Dierendonck, L.L. *A model for gas holdup in bubble columns incorporating the influence of gas density on flow regime transitions*. *Chemical Engineering Science*, 46(10):2491–2496, 1991. ISSN 00092509. doi:10.1016/0009-2509(91)80042-W.

[Kul05] Kulkarni, A.A. and Joshi, J.B. *Bubble Formation and Bubble Rise Velocity in Gas−Liquid Systems: A Review*. *Industrial & Engineering Chemistry Research*, 44(16):5873–5931, 2005. ISSN 0888-5885. doi:10.1021/ie049131p.

[Lak06] Lakowicz, J.R. *Principles of fluorescence spectroscopy*. Springer, New York, NY, 3. ed. edn., 2006. ISBN 0-387-31278-1.

[Lei17] Leite Júnior, B.R.d.C., Tribst, A.A.L., Grant, N.J., Yada, R.Y. and Cristianini, M. *Biophysical evaluation of milk-clotting enzymes processed by high pressure*. *Food research international (Ottawa, Ont.)*, 97:116–122, 2017. doi:10.1016/j.foodres.2017.03.042.

[Lei23] Leite Júnior, B.R.d.C. and Tribst, A.A.L. *Effect Of High-Pressure Technologies on enzyme*. ELSEVIER ACADEMIC PRESS, S.l., 2023. ISBN 978-0-323-98386-0.

References

[Leo15] Leonard, C., Ferrasse, J.H., Boutin, O., Lefevre, S. and Viand, A. *Bubble column reactors for high pressures and high temperatures operation*. *Chemical Engineering Research and Design*, 100:391–421, 2015. ISSN 02638762. doi: 10.1016/j.cherd.2015.05.013.

[Leo19] Leonard, C., Ferrasse, J.H., Lefevre, S., Viand, A. and Boutin, O. *Gas hold up in bubble column at high pressure and high temperature*. *Chemical Engineering Science*, 200(11):186–202, 2019. ISSN 00092509. doi:10.1016/j.ces.2019.01.055.

[Let97] Letzel, H.M., Schouten, J.C., van den Bleek, C.M. and Krishna, R. *Influence of elevated pressure on the stability of bubbly flows*. *Chemical Engineering Science*, 52(21-22):3733–3739, 1997. ISSN 00092509. doi:10.1016/S0009-2509(97)00219-4.

[Let99] Letzel, H.M., Schouten, J.C., Krishna, R. and van den Bleek, C.M. *Gas holdup and mass transfer in bubble column reactors operated at elevated pressure*. *Chemical Engineering Science*, 54(13-14):2237–2246, 1999. ISSN 00092509. doi:10.1016/S0009-2509(98)00418-7.

[Lew24] Lewis, W.K. and Whitman, W.G. *Principles of Gas Absorption*. *Industrial & Engineering Chemistry*, 16(12):1215–1220, 1924. ISSN 0019-7866. doi: 10.1021/ie50180a002.

[Lew44] Lewis, G.N. and Kasha, M. *Phosphorescence and the Triplet State*. *Journal of the American Chemical Society*, 66(12):2100–2116, 1944. ISSN 0002-7863. doi:10.1021/ja01240a030.

[Lie13] Liese, A. and Hilterhaus, L. *Evaluation of immobilized enzymes for industrial applications*. *Chemical Society reviews*, 42(15):6236–6249, 2013. doi:10.1039/c3cs35511j.

[Lin98] Lin, T.J., Tsuchiya, K. and Fan, L.S. *Bubble flow characteristics in bubble columns at elevated pressure and temperature*. *AIChE Journal*, 44(3):545–560, 1998. ISSN 00011541. doi:10.1002/aic.690440306.

[Lin20] Lindeque, R.M. and Woodley, J.M. *The Effect of Dissolved Oxygen on Kinetics during Continuous Biocatalytic Oxidations*. *Organic Process Research & Development*, 24(10):2055–2063, 2020. ISSN 1083-6160. doi: 10.1021/acs.oprd.0c00140.

[Lot74] Lott, P.F. and Hurtubise, R.J. *Instrumentation for fluorescence and phosphorescence*. *Journal of Chemical Education*, 51(6):A315, 1974. ISSN 0021-9584. doi:10.1021/ed051pA315.

[Lud03] Ludikhuyze, L., van Loey, A., Indrawati, Smout, C. and Hendrickx, M. *Effects of combined pressure and temperature on enzymes related to quality of fruits and vegetables: from kinetic information to process engineering aspects*. *Critical reviews in food science and nutrition*, 43(5):527–586, 2003. ISSN 1040-8398. doi:10.1080/10408690390246350.

[Mal22] Maly, M., Schaper, S., Kuwertz, R., Hoffmann, M., Heck, J. and Schlüter, M. *Scale-Up Strategies of Jet Loop Reactors for the Intensification of Mass Transfer Limited Reactions*. *Processes*, 10(8):1531, 2022. doi:10.3390/pr10081531.

[Man19] Manjrekar, O.N. and Dudukovic, M.P. *Identification of flow regime in a bubble column reactor with a combination of optical probe data and machine learning technique*. *Chemical Engineering Science: X*, 2:100023, 2019. ISSN 2590-1400. doi:https://doi.org/10.1016/j.cesx.2019.100023.

[Mar21] Martin, D.K., Vicente, O., Beccari, T., Kellermayer, M., Koller, M., Lal, R., Marks, R.S., Marova, I., Mechler, A., Tapaloaga, D., Žnidaršič-Plazl, P. and Dundar, M. *A brief overview of global biotechnology*. *Biotechnology & Biotechnological Equipment*, 35(sup1):S5–S14, 2021. ISSN 1310-2818. doi:10.1080/13102818.2021.1878933.

[Mas74] Massoudi, R. and King, A.D. *Effect of pressure on the surface tension of water. Adsorption of low molecular weight gases on water at 25.deg*. *The Journal of Physical Chemistry*, 78(22):2262–2266, 1974. ISSN 0022-3654. doi:10.1021/j100615a017.

[Mee06] Meersman, F., Smeller, L. and Heremans, K. *Protein stability and dynamics in the pressure-temperature plane*. *Biochimica et biophysica acta*, 1764(3):346–354, 2006. ISSN 0006-3002. doi:10.1016/j.bbapap.2005.11.019.

[O'C17] O'Connell, L. *Clark Oxygen Electrode*. https://commons.wikimedia.org/wiki/File:Clark_Oxygen_Electrode.png, 2017. Licensed under CC BY-SA 4.0: https://creativecommons.org/licenses/by-sa/4.0/.

[Pat18] Patel, R.N. *Biocatalysis for synthesis of pharmaceuticals*. *Bioorganic & medicinal chemistry*, 26(7):1252–1274, 2018. doi:10.1016/j.bmc.2017.05.023.

[Pee53] Peebles, F.N. *Studies on the motion of gas bubbles in liquid*. *Chem. Eng. Prog.*, 49(2):88–97, 1953.

[Qua12] Quaranta, M., Borisov, S.M. and Klimant, I. *Indicators for optical oxygen sensors*. *Bioanalytical reviews*, 4(2-4):115–157, 2012. ISSN 1867-2086. doi:10.1007/s12566-012-0032-y.

[Rei94] Reilly, I.G., Scott, D.S., Debruijn, T.J. and Macintyre, D. *The role of gas phase momentum in determining gas holdup and hydrodynamic flow regimes in bubble column operations*. *The Canadian Journal of Chemical Engineering*, 72(1):3–12, 1994. ISSN 00084034. doi:10.1002/cjce.5450720102.

[Rei22] Reich, J.A., Aßmann, M., Hölting, K., Bubenheim, P., Kuballa, J. and Liese, A. *Shift of the reaction equilibrium at high pressure in the continuous synthesis of neuraminic acid*. *Beilstein Journal of Organic Chemistry*, 18:567–579, 2022. ISSN 1860-5397. doi:10.3762/bjoc.18.59.

[Rin17] Ringborg, R.H., Toftgaard Pedersen, A. and Woodley, J.M. *Automated Determination of Oxygen-Dependent Enzyme Kinetics in a Tube-in-Tube Flow Reactor*. *ChemCatChem*, 9(17):3285–3288, 2017. ISSN 18673880. doi:10.1002/cctc.201700811.

[Riq89] Riquarts, H. *Strömungsmechanik disperser Zweiphasenströmungen. Reaktionstechnik und Stoffaustauschtechnik in dispersen Zweiphasensystemen, DECHEMA Monografien, Bd*, 114, 1989.

[Rol15] Rollbusch, P., Bothe, M., Becker, M., Ludwig, M., Grünewald, M., Schlüter, M. and Franke, R. *Bubble columns operated under industrially relevant conditions – Current understanding of design parameters. Chemical Engineering Science*, 126(1):660–678, 2015. ISSN 00092509. doi:10.1016/j.ces.2014.11.061.

[Rol16] Rollbusch, P. *Gas holdup in two phase bubble columns at industrial processing conditions - effect of operating parameters, liquid properties and column scale*. Dissertation, Ruhr Universität Bochum, Bochum, 2016.

[San15] Sander, R. *Compilation of Henry's law constants (version 4.0) for water as solvent. Atmospheric Chemistry and Physics*, 15(8):4399–4981, 2015. doi:10.5194/acp-15-4399-2015.

[Sau26] Sauter, J. *Die Größenbestimmung der im Gemischnebel von Verbrennungskraftmaschinen vorhandenen Brennstoffteilchen*. VDI-Verl Berlin, Berlin, 1926.

[Sch05] Schmelzer, J.W.P., Zanotto, E.D. and Fokin, V.M. *Pressure dependence of viscosity. The Journal of chemical physics*, 122(7):074511, 2005. doi:10.1063/1.1851510.

[Sch18a] Schlüter, M. *Bildung und Bewegung von Tropfen und Blasen in technischen Apparaten*. In K. Jousten, editor, *Handbuch Vakuumtechnik*, Living reference work, pp. 1–19. Springer, Wiesbaden, 2018. ISBN 978-3-658-13403-7. doi:10.1007/978-3-662-52991-1{\textunderscore}92-2.

[Sch18b] Schrittwieser, J.H., Velikogne, S., Hall, M. and Kroutil, W. *Artificial Biocatalytic Linear Cascades for Preparation of Organic Molecules. Chemical reviews*, 118(1):270–348, 2018. doi:10.1021/acs.chemrev.7b00033.

[She18] Sheldon, R.A. and Woodley, J.M. *Role of Biocatalysis in Sustainable Chemistry. Chemical Reviews*, 118(2):801–838, 2018. doi:10.1021/acs.chemrev.7b00203. PMID: 28876904.

[Ste19] Stern, O. and Volmer, M. *Über die Abklingungszeit der Fluoreszenz. Physikalische Zeitschrift*, 20, 1919.

[Sto20] Stoll, I.K., Boukis, N. and Sauer, J. *Syngas Fermentation to Alcohols: Reactor Technology and Application Perspective. Chemie Ingenieur Technik*, 92(1-2):125–136, 2020. doi:https://doi.org/10.1002/cite.201900118.

[Sur17] Surek, D. and Stempin, S. *Technische Strömungsmechanik*. Springer Fachmedien Wiesbaden, Wiesbaden, 2017. ISBN 978-3-658-18756-9. doi:10.1007/978-3-658-18757-6.

[Ten06] Tengberg, A., Hovdenes, J., Andersson, H.J., Brocandel, O., Diaz, R., Hebert, D., Arnerich, T., Huber, C., Körtzinger, A., Khripounoff, A., Rey, F., Rönning, C., Schimanski, J., Sommer, S. and Stangelmayer, A. *Evaluation of a lifetime–based*

optode to measure oxygen in aquatic systems. *Limnology and Oceanography: Methods*, 4(2):7–17, 2006. ISSN 1541-5856. doi:10.4319/lom.2006.4.7.

[Tho11] Thomas, C.R. and Geer, D. *Effects of shear on proteins in solution*. *Biotechnology letters*, 33(3):443–456, 2011. doi:10.1007/s10529-010-0469-4.

[Tho21] Thomas, B. *Anwendung von Feinblasentechnologie in der Biokatalyse*. Dissertation, Technische Universität Hamburg, Hamburg, 2021. doi:10.15480/882.3438.

[Tro00] Tromans, D. *Modeling Oxygen Solubility in Water and Electrolyte Solutions*. *Industrial & Engineering Chemistry Research*, 39(3):805–812, 2000. ISSN 0888-5885. doi:10.1021/ie990577t.

[UDoC23] U.S. Department of Commerce, N.I.o.S. and Technology. *NIST Chemistry WebBook*. https://webbook.nist.gov/, 2023. Accessed: 2025-01-03.

[Wei19] Wei, Y., Jiao, Y., An, D., Li, D., Li, W. and Wei, Q. *Review of Dissolved Oxygen Detection Technology: From Laboratory Analysis to Online Intelligent Detection*. *Sensors (Basel, Switzerland)*, 19(18), 2019. doi:10.3390/s19183995.

[Wil92] Wilkinson, P.M., Spek, A.P. and van Dierendonck, L.L. *Design parameters estimation for scale-up of high-pressure bubble columns*. *AIChE Journal*, 38(4):544–554, 1992. ISSN 00011541. doi:10.1002/aic.690380408.

[Wil94] Wilkinson, P.M., Haringa, H. and van Dierendonck, L.L. *Mass transfer and bubble size in a bubble column under pressure*. *Chemical Engineering Science*, 49(9):1417–1427, 1994. ISSN 00092509. doi:10.1016/0009-2509(93)E0022-5.

[Win88] Winkler, L.W. *Die Bestimmung des im Wasser gelösten Sauerstoffes*. *Berichte der deutschen chemischen Gesellschaft*, 21(2):2843–2854, 1888. ISSN 0365-9496. doi:10.1002/cber.188802102122.

[Wol15] Wolfbeis, O.S. *Luminescent sensing and imaging of oxygen: fierce competition to the Clark electrode*. *BioEssays : news and reviews in molecular, cellular and developmental biology*, 37(8):921–928, 2015. doi:10.1002/bies.201500002.

[Zhe19] Zheng, J. and Mao, S. *A thermodynamic model for the solubility of N2, O2 and Ar in pure water and aqueous electrolyte solutions and its applications*. *Applied Geochemistry*, 107(SA4):58–79, 2019. ISSN 08832927. doi:10.1016/j.apgeochem.2019.05.012.

Appendix

Note on Linguistic Assistance

In the preparation of this dissertation, AI-powered language processing tools were used to assist with translations and to enhance linguistic quality. Specifically, the services ChatGPT 4o and 3o (a Large Language Model) and DeepL (a neural machine translation network) were employed.

All substantive, scientific, and argumentative statements in this dissertation were independently authored, reviewed, and verified by the author. The aforementioned tools were used solely for linguistic support and did not influence the content or scientific substance of this work.

Data Availability Statement

All data, scripts, and figures used in this dissertation are stored in a repository of TUHH Open Research (TORE) and are publicly accessible.

Access to the data is provided via the following DOI:https://doi.org/10.15480/882.14608